

Lawrence Berkeley National Laboratory

Recent Work

Title

DEVELOPMENT OF FERRITIC WELDMENTS FOR GRAIN-REFINED FERRITIC STEELS FOR 4.2K SERVICE

Permalink

<https://escholarship.org/uc/item/40f9m96b>

Author

Kim, H.J.

Publication Date

1982-11-01

c.2



Lawrence Berkeley Laboratory

UNIVERSITY OF CALIFORNIA

Materials & Molecular Research Division

RECEIVED
LAWRENCE
BERKELEY LABORATORY

MAR 21 1983

LIBRARY AND
DOCUMENTS SECTION

DEVELOPMENT OF FERRITIC WELDMENTS FOR
GRAIN-REFINED FERRITIC STEELS FOR 4.2K SERVICE

Hee Jin Kim
(Ph.D. Thesis)

November 1982

TWO-WEEK LOAN COPY

*This is a Library Circulating Copy
which may be borrowed for two weeks.
For a personal retention copy, call
Tech. Info. Division, Ext. 6782.*



LBL-14748
c.2

DISCLAIMER

This document was prepared as an account of work sponsored by the United States Government. While this document is believed to contain correct information, neither the United States Government nor any agency thereof, nor the Regents of the University of California, nor any of their employees, makes any warranty, express or implied, or assumes any legal responsibility for the accuracy, completeness, or usefulness of any information, apparatus, product, or process disclosed, or represents that its use would not infringe privately owned rights. Reference herein to any specific commercial product, process, or service by its trade name, trademark, manufacturer, or otherwise, does not necessarily constitute or imply its endorsement, recommendation, or favoring by the United States Government or any agency thereof, or the Regents of the University of California. The views and opinions of authors expressed herein do not necessarily state or reflect those of the United States Government or any agency thereof or the Regents of the University of California.

LBL-14748

DEVELOPMENT OF FERRITIC WELDMENTS FOR
GRAIN-REFINED FERRITIC STEELS FOR 4.2K SERVICE

by

Hee Jin Kim
(Ph.D. Thesis)

Lawrence Berkeley Laboratory
University of California
Berkeley, California 94720

November 1982

This work was supported by the Director, Office of Energy Research, Office of Development and Technology, Magnetic Systems Division of the U.S. Department of Energy under Contract Number DE-AC03-76SF00098.

DEVELOPMENT OF FERRITIC WELDMENTS FOR GRAIN-REFINED FERRITIC STEELS FOR 4.2K SERVICE

Hee Jin Kim

Department of Materials Science and Mineral Engineering

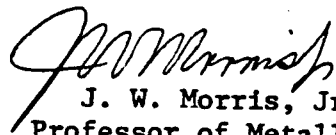
UNIVERSITY OF CALIFORNIA, BERKELEY

ABSTRACT

The weldability of grain-refined ferritic nickel steels designed for structural use in liquid helium was investigated. Plates of interstitial-free Fe-12Ni-0.25Ti alloy and carbon-containing 9Ni steel were welded with 14Ni ferritic fillers using a gas tungsten arc welding (GTAW) process with pure argon gas shielding.

The ferritic weldments made have a strength closely matching those of the base plates without a significant loss in base metal toughness at temperatures as low as 4.2 K. The comparable toughness obtained in the welded region is attributed to three factors; the defect-free weldment, the chemical cleanliness of the GTAW weld deposit, and the in-process formation of an appropriate microstructure in the welded region. Special emphasis in this study was placed on changes in microstructures with respect to the characteristic of the weld thermal cycles and the effect of the resultant microstructures on low temperature toughness. In the heat-affected zone (HAZ) of multi-pass welded 9Ni steel, the retained (or precipitated) austenite is removed by the weld heat cycles but the sequential rapid heat cycles to successively lower peak tempera-

tures associated with succeeding weld passes re-establish high toughness by sequentially refining the grain size and getting carbon in the form of cementite precipitates. On the other hand, the high toughness in the HAZ of the 12Ni alloy and in the weld deposit is a direct consequence of repeated grain refinement through the overlapped austenitizing cycles and is not affected by the tempering cycles because of the carbon-free nature of these materials.



J. W. Morris, Jr.
Professor of Metallurgy
Chairman of Committee

Table of Contents

Chapter I: Introduction	1
Chapter II: Experimental Procedures	7
Chapter III: Experimental Results	19
A. Weld Solidification	19
B. Weld Cycle Simulation	23
C. Microstructure of Full Thickness Weldments	29
D. Mechanical Properties of Ferritic Weldment	31
Chapter IV: Discussion	40
A. Effect of Composition	40
B. Effect of Weld Thermal Cycle	43
C. Ferritic Weldment for 4.2K Service	53
D. Alternative Welding Procedures	59
Chapter V: Summary and Conclusions	61
References	65
Tables	72
Figure Captions	78
Figures	82

ACKNOWLEDGMENTS

The author wishes to express his deepest gratitude to Professor J. W. Morris, Jr. for his guidance, support, and encouragement throughout the course of this research. He is also grateful to Professors R. Ritchie and D. Donfeld for their reviews of this manuscript. Thanks are also due Drs. C. K. Syn and Jungihl Kim for their advice and encouragement.

The author must acknowledge the assistance provided by the support staff of the Materials and Molecular Research Division, Lawrence Berkeley Laboratory, especially Ken Gaugler (SEM and x-ray), Brian Pope (alloy making and metallography), Don Krieger (mechanical testing), Herb Liebe and Weyland Wong (machining), Sandy Stewart (purchasing), and Gloria Pelatowski (line drawings).

The author wishes to thank Mr. Fred Lockwood and his students at Contra Costa Community College, who performed the non-destructive testing on all of the welds in this study. Special thanks are extended to Nippon Kokan K.K., Japan, for donating 9% Ni plates for part of this research.

Very special thanks are owed Mrs. Jeanne Shull for the careful preparation and typing of this manuscript. Thanks are also extended to the author's colleagues, especially to Mr. M.J.Strum and Mr. Karou Sakai for their help in reviewing this manuscript.

The author is greatly indebted to his family, especially to his wife, Soon, and his son, Andrew, for their patience and love.

This work was supported by the Director, Office of Energy Research, Office of Development and Technology, Magnetic Systems Division of the U.S. Department of Energy under Contract Number DE-AC03-76SF00098.

**DEVELOPMENT OF FERRITIC WELDMENTS FOR GRAIN-REFINED
FERRITIC STEELS FOR 4.2K**

HEE JIN KIM

**CHAPTER I
INTRODUCTION**

A. Background.

Production of electricity from nuclear fusion may rank as one of man's major technological achievements. One of the most promising approaches to achieve this goal uses magnetic confinement of the reacting plasma. Economic considerations lead to the conclusion that the magnetic fields required for confinement must be produced by large superconducting magnets. The production of these large magnets has required a significant extension of existing cryogenic materials since most structural components of the superconducting machinery are cooled by liquid helium to 4.2K (-269°C). Moreover, for fusion magnetic systems, the principal features governing alloy selections for structural applications are the enormous size, the extremely high forces exerted by the magnetics, the massive structural elements needed to restrain these forces, the limited space available for the structure, etc. [1] These features result in the need for alloys with sufficient strength and stiffness to perform the required struc-

tural functions within the space available, sufficient fatigue and fracture resistance to operate safely at 4.2K, and sufficient fabricability to permit manufacture and assembly of the components.

Currently, the austenitic stainless steels, particularly the nitrogen-strengthened grades such as 304LN and 316LN, are the most widely used alloys for structural application in superconducting magnet systems. But these stainless steel grades are not necessarily the most suitable because of high cost, low strength, microstructural instability during cold deformation and temperature drops, and the scarcity of Ni resources. Moreover, requirements for structural materials in the expanding cryogenic technology demand a combination of high strength coupled with high toughness. For example, one set of criteria documented [2] by Japan Atomic Energy Research Institute (JAERI) for the future Fusion Engineering Reactor (FER) suggests a yield strength in excess of 1200 MPa (174 ksi) with fracture toughness above $200 \text{ MPa} \sqrt{m}$ ($182 \text{ ksi} \sqrt{\text{in}}$) at 4.2K. This high combination of strength and toughness can hardly meet with varying composition of stainless steels due to the well-known inverse relationship [3] between yield strength (σ_y) and fracture toughness (K_{IC}) at 4.2K, that is, $K_{IC} (\text{MPa} \sqrt{m}) = 500 - 0.3\sigma_y (\text{MPa})$.

So, several alloys including high manganese austenitic steels [4-6] and ferritic steels [7-10] have been and/or are being developed to get a higher combination of strength and toughness than that of the 300 grade stainless steels.

Historically, the ferritic grades have been eliminated from consideration for 4.2K use on the grounds that BCC alloys tend to undergo a ductile-to-brittle transition as the temperature decreases. However, recent research [7-9] has demonstrated that the ductile-to-brittle transition temperature of Fe-(9-12)Ni ferritic cryogenic steels can be suppressed to below 4.2K by applying heat treatments which establish an ultra-fine grain size. In particular, a laboratory Fe-12Ni-0.25Ti alloy has been grain-refined by a four-step (so-called "2B") thermal cycling treatment and a commercial Fe-9Ni alloy has

been reprocessed through a five-step (so-called "2BT") treatment to achieve an excellent combination of strength and toughness at 4.2K, and recently these alloys have potential applications in the structures of high field superconducting magnets despite being ferromagnetic. Since the structures of such magnets are almost invariably welded, needless to say, their application is mostly dependent on their weldabilities. The research project described herein attempts to evaluate their weldabilities while developing filler wire chemistry and optimizing welding procedures.

B. Toughening Mechanism of Ferritic Nickel Steels.

Several factors have been known to control the low temperature toughness of ferritic steels such as grain size, interstitial content, presence of retained austenite and its distribution. The superior toughness of Fe-12Ni-0.25Ti alloy at 4.2K, for instance, is derived mainly from extremely low interstitial content and its ultra-fine grain size imparted by 2B heat treatment. The detailed discussion of this grain refinement procedure is given elsewhere [7]. Its essential features are, however, evident in Fig. 1-a. In this treatment, thermal cycles into the austenite field ("A" treatment) are alternated with intercritical annealing ("B" treatment) at a relatively high temperature in the two phase $\alpha+\gamma$ region. The initial structure (AN) annealed for two hours at 900°C has a grain size of 60 μm . This is reduced to about 15 μm by an 1A treatment of $\alpha\rightarrow\gamma\rightarrow\alpha$ thermal cycle. The 1A structure is decomposed by a nucleation and growth process during 1B treatment at 650°C in which austenite grains form in the prior austenite grain boundaries and along the martensite lath boundaries. The preferential alignment of these grains is largely broken up by a second reversion cycle of the 2A treatment. The grain refinement is completed through a final two-phase decomposition at 650°C. After cooling to room temperature the alloy consists of fine grains of tempered martensite. No residual or precipitated austenite exists in the final structure. Although the details of the grain-refining mechanism during the 2B treatment needs further study, this treatment has been applied successfully in 9Ni [9] and 5Mn steels

[11] with the addition of a final intercritical tempering treatment as shown in Fig. 1-b. Since the 9Ni steel, which is commercially available in the quench-and-tempered (QT) condition for 77K use, contains approximately 0.06 percent of carbon, the reprocessing of this steel by a 2B treatment was not successful in toughening this steel at 4.2K because of the presence of carbon in the refined matrix. To overcome this problem, the final tempering ("T" treatment) in the low portion of the $\alpha+\gamma$ field has to follow the 2B treatment in order to introduce a distribution of austenite phase into the structure. This austenite stable even at low temperature serves two functions: it refines the effective grain size of the steel by disrupting the crystallographic alignment of martensite packets, hence lowering the ductile-to-brittle transition temperature (DBTT) [12], and it getters carbon from the lattice, hence raising the upper-shelf toughness [13,14]. Therefore, the good toughness of the 2BT-treated 9Ni steel at 4.2K is derived not only from the fine grain size but also from the finely distributed austenite phase.

Table I summarizes the 4.2K properties of these ferritic steels along with those of the stainless steel grades for comparison. It clearly shows a more desirable combination of strength and toughness can be obtained with ferritic steels. However, the 'equivalent energy method' used for measuring fracture toughness of ferritic steels in references [8] and [9] was purely empirical and has no basis of crack initiation. More precise evaluation of these materials with reliable methods such as 'crack-initiation J_{IC} test' is needed, as well as the weldability study.

C. Objectives and Approach.

The objective of this investigation is to develop the filler metal chemistry and suitable welding process and conditions for the intended use of grain-refined ferritic 9 and 12Ni steels. As mentioned previously, since the structure of superconducting magnets must be welded, the valuation and improvement of their weldability are the most important factors for the practical use of these steels.

The welding problem is, at least superficially, a formidable one. The good cryogenic properties of the base alloys are achieved through the use of heat treatments which establish a rather precise control over the alloy microstructure. Subsequent welding introduces the simultaneous problems of establishing a suitable microstructure in the weld deposit and retaining an appropriate microstructure in the heat-affected zone.

Initial research on the welding of this [17] and similar alloys [18] for 4K service employed high-nickel Inconel filler metals to avoid the problem of brittleness in the weld deposit. However, the gas metal arc (GMA) welding of Fe-12Ni-0.25Ti with Inconel 92 filler [19] was partly successful. The Inconel 92 filler was inferior to the ferritic base metal over the whole temperature range, not only in its yield strength but also in its notch toughness. In addition, the Inconel 92 weldment exhibited a fusion zone brittleness which was also reported by others [19] on the welding of Fe-9Ni steel with non-matching austenitic fillers; cracks starting in the heat-affected zone tend to propagate along the fusion line. Furthermore, because of the high alloying content of such filler materials, they tend to be expensive.

A more suitable approach from both a metallurgical and economical standpoint would be to develop a low nickel matching ferritic filler, whose strength and physical properties would be more compatible with the base metals. Unfortunately, early attempts [20] to weld quench-and-tempered (QT) 9Ni steel with matching ferritic consumables combined with gas-metal arc welding (GMAW) process resulted in cracked welds with very poor toughness at low temperatures.

A more promising approach was developed in joint research between the Japanese steel companies, Nippon Kokan K.K. and Kobe steel [21], who showed that QT 9Ni steel may be welded for 77K service with a matching ferritic filler if a multi-pass gas-tungsten arc welding (GTAW) process is employed. The GTAW process provides a relatively clean weld deposit and permits a largely independent control of the heat input

and deposition rate. In the controlled GTAW process, subsequent weld passes may be made to impose thermal cycles on the solidified material, hence refining the structures of the weld deposit and preserving a refined microstructure in the heat-affected zone (HAZ). This process is now used commercially in Japan in the manufacture of liquid natural gas (LNG) tanks [22]. Exploratory work at the NASA Lewis Research Center [23] showed that the GTAW process could also be used for autogenous welding of Fe-12Ni-0.25Ti and two other similar alloys, and reported that it produces a sound weldment with good toughness at 77K.

The microstructural constraints which must be satisfied to achieve good toughness at 4K are much more stringent than those required for toughness at 77K. Nonetheless, the metallurgical approach of the multi-pass GTAW process as a means of controlling the microstructure of the weldment together with the success which has already been achieved at 77K suggest that this process may be successful for joining ferritic cryogenic steels for 4K service.

The microstructural problem in welded 9Ni steel is superficially more difficult than in the 12Ni alloy since the 9Ni steel base plate has good 4K properties only when it is given a final intercritical tempering to introduce a distribution of stable austenite phase into the grain-refined structure. Therefore, the retention of retained austenite phase near the fusion line and in the heat-affected zone may be important to 4K toughness of the 9Ni welded joint. However, there have been conflicting results reported in the literature [24,25] as to the effect of thermal cycling on the presence of retained austenite. Hence, the present work has paid particular attention to the influence of weld thermal cycles on the microstructural changes and to identify the microstructural features controlling low temperature toughness. To isolate the fusion zone effects from HAZ properties, specimens were heat treated to simulate HAZ conditions. Based on the simulated results, it was also attempted to establish the optimum welding conditions for a better microstructure and properties.

CHAPTER II

EXPERIMENTAL PROCEDURES

A. Material Preparation and Welding Procedures.

1. Base Plates.

The compositions of 9 and 12Ni alloy used in this research are given in Table I. The 9Ni steel was a commercial grade provided by Nippon Kokan, K.K. containing about 0.06% carbon. The material was received in the form of 24.5mm (1.0 inch) thick plates in the quench-and-temper (QT) condition. The 12Ni alloy of nominal composition Fe-12Ni-0.25Ti was cast in the laboratory after vacuum induction melting from pure starting materials. It was cast as a 25 lb (9.425 Kg) ingot, homogenized at 1200°C for 24 hours under inert atmosphere, and then upset cross-forged at 1100°C into plates of 7-inch width and 0.6-inch thickness (175x15mm).

Both the 9Ni and 12Ni base plates were annealed at 900°C for 2 hours to remove the effects of prior deformation and thermal treatment, and then given the 2BT and 2B heat treatments (diagrammed in Fig. 1) respectively. After full heat treatment, these plates were machined into the weld joint configurations described in section A-3.

2. Filler Metals and Wire Fabrication.

The compositions of two filler metals (designated Filler A and B) used in this research are given in Table I. They have a slightly higher nickel content (14%) than the base plates plus intentional additions of other alloying elements such as silicon and manganese in filler A and boron in filler B. Both filler metals were cast into 5 lb (9.25 Kg) 1 in (25 mm) diameter ingots. After homogenization at 1200°C for 24 hours the ingots were hot rolled into 5/16 in (7.9 mm) square bars at a starting temperature of 1100°C, then hot-swaged to 1/2 in (6.4 mm)

diameter round bars and surface ground to remove any oxides. The ground bars were cold-swaged to 1/16 or 3/32 in (1.59 or 2.38 mm) diameter bars, which were used as the filler rod for the manual GTA welding process. During the cold swaging process, the wire surface was cleaned repeatedly by hand grinding with 320 and 180 grit emery paper followed by degreasing with acetone and ethyl alcohol.

3. Welding Procedures.

The plates to be welded were machined into one of the two joint configurations diagrammed in Fig. 2; a 45° single bevel or a 60° single V or a 60° double-V groove. The plates were welded with a manual multi-pass GTAW procedure using one of the two sets of welding conditions tabulated in Table II. In order to prevent excessive oxidation of the root pass, a copper back-up plate with a machined V-groove was clamped under the plates to be welded allowing the joint to be continually purged with a 100% argon gas backup during the root pass. After the root pass, the back-up plate was removed and the plates were fully-restrained using C-clamps to prevent distortion during welding. The maximum interpass temperature was maintained below 100°C and no preheat was employed. Cleaning between passes was restricted to wire brushing followed by ethyl alcohol and acetone rinse unless visible defects, which required grinding, were evident. No post-weld heat treatments were performed on the weldments. Completing the single V-joint in an 0.6 in (15 mm) plate require ≈35 passes at a heat input of 0.7 kJ/mm versus 12 passes at a heat input of 1.7 kJ/mm. The completed welded joint was examined non-destructively by x-ray radiography using a voltage of 250 kV and a 10 mA current. No significant defects were found in any of the weld joints made in this study. Bead-on-plate welds were also made under a variety of conditions to study weld solidification characteristics and ferritic weld structures. For the same purpose, a single-pass Electron Beam (EB)

welded 12Ni specimen with weld conditions of 80 kV and 50 mA was analyzed in this study.

B. Weld Thermal Cycle Simulation.

Single and multiple thermal cycling studies were conducted to gain insight into the response of the base metals to the rapid heating and cooling cycles encountered during welding. The thermal cycles were imposed on slightly oversized Charpy impact specimens in an induction furnace. The sample was suspended in the center of a 38 mm diameter quartz tube surrounded by the induction coil. This coil was connected to a 30 kW RF (radio frequency) generator. The samples were heated at 20 kW by setting the power level if the peak temperatures were over 1200°C or by changing the power level to keep a constant heating rate for the lower peak temperature cycles. With a current level setting of 120 mA, sample heating rates of 120°C/sec from room temperature to \approx 700°C and 30°C/sec in the higher temperature ranges were obtained. The typical temperature profile up to 1300°C is shown in Fig. 3. The dramatic decrease in heating rate that occurred at the transformation temperature range (A_5) seems to be due to the sudden change in phase from bcc to fcc through the reverse martensitic transformation. Since it was not possible to keep the constant heating rate beyond the transformation temperature by electronic control, it was performed manually by changing the power level. To be able to read the exact peak temperature, lower heating rates of 27°C/sec were employed for all the cycles except 1200°C and higher temperature cycles. For cycles having a peak temperature lower than 1200°C, the temperature was monitored by a chromel-alumel thermocouple spot-welded on the specimen surface and then connected both to a chart recorder and to a digital indicator. For cycles having peak temperature higher than 1200°C, an optical pyrometer was used. Once the selected peak temperature had been reached the sample was dropped into a

quenching bath of either water or oil. The cycled specimens were machined into standard-sized Charpy V-notch specimens and tested at 77K in accordance with ASTM 23-72 [26].

C. X-ray Diffraction Analysis.

X-ray diffraction analysis was performed to identify the austenite phase and to determine the volume fraction of retained austenite in specimens quenched in liquid nitrogen bath (77K) for 30 minutes. In order to measure the variation of austenite content across the HAZ, the welded specimens were sliced parallel to the fusion boundary (as shown in the insert to Fig. 32) and mounted in Koldmount. These specimens were ground on successive emery papers up to 600 grade and then chemically polished in a solution containing 3 ml HF + 100 ml H_2O_2 for about 10 minutes in order to remove any deformed surface where mechanically-induced transformation of the austenite phase may have occurred. After these treatments, the specimens were scanned with a Picker x-ray diffractometer using $CuK\alpha$ radiation. The distribution of austenite across the HAZ was found by sequential grinding and chemical polishing.

X-ray analysis was also done on the heat-cycled specimens which have also been used for optical examination. These specimens were cut from broken Charpy specimens along a transverse direction and then mounted in Koldmount. After optical examination, these specimens were chemically repolished and scanned as described above.

The calculation of the volume fraction of precipitated austenite was based on Miller's method [27], comparing average integrated intensities of the (220) and the (311) austenite peaks to that of the (211) martensite peak. No correction was made to take into account the preferred grain orientation which might develop during rolling. Therefore, there would be an error, about ± 1 pct., in absolute value of the retained austenite phase investigated in this research.

D. Mechanical Tests.

The mechanical tests conducted included hardness, uniaxial tensile, Charpy impact and fracture toughness tests. To prepare test specimens, the welded plates were sliced perpendicular to the joint and etched with 10% nital or 3 ml HF + 100 ml H_2O_2 solutions which was useful to reveal the weld location on the sliced surface. The specimens were then machined and a notch made at a specified location and orientation with respect to the welded joint.

1. Hardness Test.

A Leitz Miniload Hardness Tester with a 200 gm. load and a diamond pyramid indenter to register Vickers hardness was used to continuously scan across the various weldments at a level of $1/2 t$ (t =joint thickness). The Rockwell hardness was also measured using a Wilson Rockwell hardness tester. The Rockwell B or C scale was used with an escape time of 15 seconds taken as standard.

2. Tensile Test.

The uniaxial tensile tests employed subsized specimens of 0.5 in (1.27 cm) gage length and 0.125 in (0.3 cm) gage diameters (Fig. 4), which were machined so that the gage length included base metal, HAZ material, and weld metal. Testing at 77K was done in an Instron machine equipped with a liquid nitrogen Dewar at a crosshead speed of 0.05 cm/min. The yield strength was calculated by the 0.2% offset method and the total elongation was determined by measuring the difference in distance between gage length marking before and after testing. The elongation and reduction in area were measured to within an accuracy of ± 0.01 mm with a traveling microscope.

3. Charpy Impact Test.

Standard-sized Charpy V-notch specimens were machined from the base plates and the weldments as shown in Fig. 5. The notches in the base plate and HAZ-simulated specimens were machined perpendicular to the rolling direction of the plate. Charpy impact specimens intended to test the HAZ and fusion line toughness were notched parallel to the welding direction. Weld metal specimens were prepared both with the notch parallel to the welding direction and with the notch parallel to the weld axis as shown in Fig. 31.

Charpy impact tests at 300K (room temperature), 77K (liquid nitrogen temperature) were performed according to ASTM specifications [27]. The impact tests at 4-5K (liquid helium temperature) used slightly short Charpy impact specimens, 51 mm in length, which were enclosed in insulation styrofoam boxes and bathed in liquid helium until struck by the impact hammer.

The styrofoam box configuration is a slight modification of the 'lucite box' previously used by Jin et al. [28]. A rectangular styrofoam block of dimensions 12 x 24 x 51 mm was cut and hollowed out to house the Charpy specimens as shown in Fig. 6. Two holes were made on the top surface for liquid helium flow. After inserting the specimen a styrofoam cover was glued onto the open face. The whole assembly was then wrapped with scotch tape for easy handling. The testing procedure was identical to that reported in reference [28]. Typical temperature-time curves obtained on transferring liquid nitrogen and liquid helium as shown in Fig. 7. The cooling rates down to 4.2K are almost the same as reported previously [28] even with the simple geometry.

4. Fracture Toughness Test.

Fracture toughness measurements were made on three types of specimens: pre-cracked Charpy specimens tested in three-point bending, compact tension

specimens according to ASTM specification [30], and modified compact tension specimens for J_{IC} test. All the dimensions of these specimens are shown in Fig. 8. For the three-point bend tests, as shown in Fig. 8a, the Charpy specimens were given a 0.008 inch (0.2 mm) wide saw cut of about 1 mm depth at the root of the Charpy V-notch in order to minimize the deviation of the fatigue pre-crack from the desired location. After fatigue pre-cracking to initial crack length to specimen width (a/w) of ≈ 0.5 , these specimens were tested in a three-point bending fixture immersed in a liquid nitrogen bath at a cross-head speed of 0.06 mm/min in a 300K-lb (1.6×10^5 kG) capacity MTS Universal Testing machine equipped with a cryostat. The "compact tension" fracture toughness specimens were 13 mm (0.51 in) in thickness and were fatigue pre-cracked to a crack length ratio (a/w) of ≈ 0.5 in accordance with ASTM E-399 [29]. These specimens were broken at 77K under immersion in liquid nitrogen at a cross-head speed of 0.06 mm/min. The compact tension specimens were also tested at liquid helium temperature (4.2K) again using a styrofoam box modification of the lucite box technique reported previously [8]. Space for the compact tension specimen was hollowed out of a 25 mm thick styrofoam block and grooves were made on the inside surfaces to facilitate helium flow. The specimen assembly was wrapped and inlet holes were provided for liquid helium as described in ref [8]. The temperature during the sample cooling and testing was monitored by a Au + 0.07Fe-Chromel thermocouple embedded in the sample near the crack tip. The fracture toughness test was conducted after the sample temperature had stabilized near 4K.

None of the specimens tested with the above two types of geometry met ASTM requirements for small scale yielding (the plastic zone size is merely a small perturbation in the linear plastic field). However, the recent development in elastic-plastic fracture theories, i.e., the J-integral concept [30,31], crack tip

opening displacement (CTOD) approach [32], and equivalent energy approach [33,34] allow the evaluation of fracture toughness from non-linear load-displacement curves. The plain strain toughness values, denoted $K_{IC}(E)$, of the three-point bend and compact tension specimens were estimated from the "equivalent energy" criterion. The relevant equations are

$$K_{IC}(E) = \frac{P_q S}{B W^2} f\left(\frac{a}{w}\right) \sqrt{\frac{A_1}{A_2}} \quad (1)$$

for three-point bend specimens and

$$K_{IC}(E) = \frac{P_q}{B} W^{\frac{1}{2}} f\left(\frac{a}{w}\right) \sqrt{\frac{A_1}{A_2}} \quad (2)$$

for compact tension specimens, where a , W , B and S are respectively the crack length, specimen width, thickness and span length, P_q is the maximum load on the linear portion of the load-displacement curve, $f(a/w)$ is the geometric shape factor [29] and A_1 and A_2 are the areas under the load-displacement curve up to the maximum load and the load P_q . The fracture toughness values, $K_{IC}(E)$, given in the following are the averages of two or more test results. The equivalent energy concept, however, is quite empirical in nature because it lacks information about crack initiation.

The equivalent energy results, $K_{IC}(E)$, obtained by the above equations only serve as a useful guide to expected toughness so that the J-integral test, which was developed on the sound basis of elastic-plastic fracture mechanics, is to be preferred for the precise evaluation of the materials. The J-integral test has the advantage of being applicable to smaller specimens (up to 100 times smaller) and tougher materials than the plane strain fracture test (K_{IC} test). A disadvantage of J-integral technique has been its experimental difficulties and its high cost for the large number of specimens. Recently developed single specimen J-integral tests eliminated the multiple-specimen requirement through a compliance measurement technique useful even at low temperature.

In this research, the modified compact tension specimens (Fig. 8c) were tested in accordance with the J-integral procedures described elsewhere [3]. Each specimen is loaded to a certain amount of displacement and then partly unloaded, about 10 percent, with the unloading slope giving an instantaneous measurement of crack length, Δa , through the compliance calculation [35]. A series of unloadings at various load levels recorded in amplified scale on the other recorder will reflect the beginning of crack advance and also the amount of crack extension (Δa). The J-integral value at the certain amount of crack extension is calculated using the following equation:

$$J = \frac{A}{B b} f(a/W) \quad (3)$$

where A equals the area under load, load-point displacement curve up to the unloading point.

B and W are the same as in equations 1 and 2.

b equals initial uncracked ligament, $W - a_0$.

a_0 equals original crack size, including fatigue precrack.

$f\left(\frac{a_0}{W}\right)$ equals a dimensionless coefficient value that corrects for the tensile component of loading. Values are given in ref. [37]. For a given test, a curve of J vs. Δa is constructed, which is called a R-curve. On the same graph, the blunting line defined by equation (4) is drawn:

$$J = 2\sigma_f \Delta a \quad (4)$$

where $\sigma_f = (\sigma_{ys} + \sigma_{UTS})/2$, $\sigma_{ys} = 0.2\%$ offset yield strength, and $\sigma_{UTS} =$ ultimate tensile strength. The intersection of the J- Δa plot (R-curve) and blunting line is defined as J_{IC} , the value of J at the onset of crack extension in plane strain. Apparent crack extension at Δa values less than $J/2\sigma_f$ is attributed to deformation at the crack tip instead of material separation. Begley and Landes [31] have proposed that the plane strain fracture toughness, K_{IC} , is related to J_{IC} as

follows:

$$K_{Ic} (J) = \left(\frac{J_{Ic} E}{1 - \nu^2} \right)^{\frac{1}{2}} \quad (5)$$

where E is Young's modulus and ν is Poisson's ratio. The values of E and ν at 77 and 4.2K were estimated as 29×10^9 psi (200 GPa) and 0.3 respectively based on the reference [37].

The 77K tests were conducted in the MTS machine and 4.2K tests in a 50K-lb capacity Instron machine (Model No. 1332) equipped with liquid helium cryostat.

E. Microscopy.

1. Optical Microscopy.

Specimens for optical microscopy were cut from the weldment or from broken Charpy bars to reveal the microstructure below the fracture surface. The samples were mounted in Koldmount and ground on successive emery papers up to 600 grade under water-flood cooling. Polishing was done on $6\mu m$ and $1\mu m$ diamond paste wheels.

Polished sections were examined after etching with one of two reagents: a 5% nital solution, which reveals the solidification structure, and an acidified $FeCl_3$ solution, 200 ml HCl + 200 ml H_2O + 20 gr $FeCl_3$, which brings out the columnar grain structure and details of the transformation structure. The microstructures were examined with a Carl Zeiss metallograph.

2. Scanning Electron Microscopy (SEM) and Energy Dispersive Analysis of X-rays (EDAX).

Fracture surfaces of tested specimens were examined with an AMR 1000 scanning electron microscope operated at 20 kV. An energy dispersive analysis of x-rays (EDAX) spectrometer unit attached to the microscope permitted semi-quantitative chemical analysis of precipitates within dimples on the fracture

surfaces.

Brittle fracture surfaces, i.e., either intergranular or transgranular cleavage, which were induced by impact loading the single bead weldment at 77K, were examined before and after etching in such a manner to obtain the analytical features of weld solidification structure on the fracture surfaces. The etching with 5% Nital solution for 5 minutes was able to reveal the cellular substructure on either cleavage facets or intergranular surfaces of columnar grains. In addition, etch pits were developed on the brittle cleavage plane by dipping the fracture surface in the several solutions successively as reported in ref. [38]. Through the examination of these etch pits under SEM, it was possible to determine the orientation of the cellular structure.

3. Transmission Electron Microscopy (TEM).

Most of the TEM studies were done on weld-simulated 9Ni steel. Thin slices of about 0.25 mm thick were cut from broken Charpy specimens tested at 77K. The sliced specimens were mechanically and then chemically thinned to about 0.1 mm in a solution of 3 ml HF + 100 ml H_2O_2 . Three mm discs were spark cut at the mid-section of these slices and sanded down to 0.002 in (0.05mm) in thickness. These thin foils were finally electropolished in a twin jet electropolishing apparatus using a solution of 400 ml CH_3COOH , 75 g CrO_3 , and 2l ml H_2O . The polishing voltage varied from 20 to 25 volts. Specimens so obtained were examined in a Phillips EM 301 electron microscopy at an operating voltage of 100 kV.

4. Auger Electron Spectroscopy (AES).

A PHI 590A scanning Auger microprobe with a minimum spot size of $0.3\mu m$ was used to analyze the low atomic number elements contained in weld metal inclusions. The specimens were broken at near 77K in a vacuum chamber main-

tained in the 10^{-10} torr range. Then the particles inside the dimple were analyzed at the operating voltage of 8kV. Chemical information was plotted in the form of the first derivative of the number of counts, N , per electron energy, E , (dN/dE) versus electron binding energy (eV). Peaks were correlated with their corresponding chemical elements using the ref [39].

CHAPTER III

EXPERIMENTAL RESULTS

A Weld Solidification.

1. Bead-on Plate Weldments.

A variety of test weldments were made on the 12Ni plates at heat inputs ranging from 0.7 kJ/mm to 7 kJ/mm. These had essentially similar microstructures, which consisted of columnar grains made up of bundles of solidification cells apparently growing in the same direction (later it will be proven to be the $\langle 100 \rangle$ direction in austenite.) The cellular solidification substructure is revealed by a nital etch as shown in Fig. 9-a. No dendritic structures were observed in the heat input range studied in this research. The columnar grains revealed by chloride etching solution are shown in Fig. 9-b. As observed by other investigators [40-42], they appear to grow epitaxially (From the Greek "taxi" - to arrange and "epi" - upon.) from half-melted coarsened grains along the fusion line. It is noted that the grain boundaries are continuous across the fusion line and that no boundary is created across the grains at the fusion line. This metallographic evidence of epitaxial growth has been supported conclusively by micro-beam x-ray diffraction studies [42] which showed the crystallographic orientation of each grain to be continuous across weld fusion boundary. The average lateral dimension of columnar grains tends to increase with increasing heat input (Fig. 10) as reported by Matsuda et al. [42].

An examination of partially overlapped bead-on-plate weld passes (Fig. 10) shows that the solidification structure is hardly affected by the subsequent passes but the columnar grains are destroyed. The result is a fine equiaxed grain structure even at the fusion boundaries. It represents the columnar grains or coarsened HAZ grains formed during the earlier pass did not coarsen further at the fusion boundaries of a

later pass.

High melting point inclusions, such as oxides, were not found in the optical examinations. However, small spherical inclusions, possibly titanium oxide particles were often found in the TEM studies of full-thickness welds. These oxide inclusions will be proved to be the dominant void nucleation sites in a later section.

2. Solidification Structures on Fracture Surfaces.

As described in optical examinations, the solidification microstructure of 12Ni alloy has two features, i.e., columnar grain structure and cellular solidification substructure. In this study, it was possible to reveal those two features on the brittle fracture surfaces. Figure 11-a is the SEM fractograph which shows the individual columnar grains on the fracture surface. This specimen was prepared from the 'bead-on-plate' weld with heat input of 7 kJ/mm with a saw-cut made towards the weld bead up to the grain-coarsened HAZ as shown in Fig. 11-b. By impact loading at 77K, the fracture mode changed from transgranular cleavage in the HAZ to intergranular in the weld metal. The metallurgical sources of intergranular brittleness in weld metal have not been studied but it makes possible the assessment of the growth mechanism of columnar grains during weld solidification. As shown in Fig. 11-a, the columnar grain grown from HAZ grains continue to grow toward the center of the weld metal until their growth was restricted by other elongated grains grown horizontally along the the welding direction. This kind of growth pattern has been reported [43,44] to be developed when the weld pool has an elliptical shape which tends to minimize alloy segregation at the weld centerline. The dissipation of the latent heat of fusion liberated at the moving solid-liquid interface exerts a major influence on the shape of weld pool. Since the instantaneous rate of liberation of latent heat is directly proportional to the rate of growth of the solid, the maximum rate occurs at the centerline of the weld pool. Therefore, above some critical welding velocity, the shape of weld pool changes from elliptical to tear drop. In the case of the tear drop shape, since all the columnar grains

terminate their growth at the centerline of the weld pool, the central region has the highest alloying content (with positive segregation) and becomes the weakest point in the weldment. In the present study, no tear drop shaped weld pools were observed in the 'bead-on-plate' welds with welding speeds ranging from 3 to 15 mm/sec and with various heat input levels up to 7 kJ/mm.

Etching the fracture surface with 5% Nital solution reveals the cellular patterns on the surface of each columnar grain as shown in Figs. 11-d and 12. All the cell boundaries are exclusively straight regardless of the curvature of the columnar grains which have grown following the direction of maximum thermal gradient at the liquid-solid interface. A typical example of the straight growth of cells is shown in grain 'a' in Fig. 12-a. The grain consists of a bundle of cells which have nucleated on the one side of the grain, grown straight across the grain and terminated on the other side. Another growth pattern is shown in grains 'b' and 'c' in Fig. 12. These grains consist of a couple of bundles and each of them are growing in different directions. This kind of pattern has not been reported previously in the literature.

On the other hand, the cellular pattern revealed on the cleavage facets are either the long axis of cells or roughly hexagonal cross sections as shown in Fig. 13. This specimen was taken from the fully penetrated electron beam (EB) welded 12Ni plate fractured at 77K. As shown in Fig. 13, the long axis of the cells are always perpendicular to a set of cleavage planes and parallel to the other set of planes. Considering that the {100} plane is the dominant cleavage plane of body-centered cubic (bcc) crystals [45-47], particularly at low temperature [48], the long axis of the cells seem to be parallel to $\langle 100 \rangle$ direction of the bcc martensite phase.

In order to obtain a direct observation of cell orientation, etch pits were developed on the {100} cleavage facets. During the SEM observations of etch pits, it was confirmed that the cell axis is parallel to not only $\langle 100 \rangle$ but also the $\langle 110 \rangle$ direction of martensite. For example, the SEM picture in Fig. 14 shows that cell axis is almost

parallel to the diagonal direction of square-shaped etch pits, which have been reported to be developed on the $\{100\}$ plane of martensite [38]. The diagonal direction was analyzed to be the $\langle 110 \rangle$ direction of martensite as shown in Fig. 14. Consequently it is demonstrated that the cell direction is parallel to the $\langle 110 \rangle$ direction of martensite as well as $\langle 100 \rangle$ direction.

3. Preferred Growth Orientation of Cell Structure.

The occurrence of a preferred orientation in the columnar zone of castings is well known after the extensive research done by Walton et al. [49]. They reported that it has been attributed to the preferred growth direction of dendritic structures in the cast. And they summarized all the published data and demonstrated that the $\langle 100 \rangle$ crystallographic orientation is the preferred growth direction of dendritic structures in bcc or fcc alloys. The $\langle 100 \rangle$ preferred orientation was also derived in the cellular structure of Pb-Ag alloy by Rosenberg et al. [50]. Later, the $\langle 100 \rangle$ orientation has generally adopted [40], as the preferred growth direction of cell structures even in the weld solidification considering the same solidification principles in the weld deposit as in castings.

The result in the previous section showed that the cell boundaries are parallel to either $\langle 100 \rangle$ or $\langle 110 \rangle$ direction of bcc martensite. These two orientations can be traced back to their original orientation in the austenite phase through the orientation relationship between austenite and martensite. According to well known orientation relationships [51], viz Bain, Kurdjumov-Sachs (K-S), and Nishiyama-Wasserman (N-W) relations, the nearest common index directions of austenite from $\langle 100 \rangle$ and $\langle 110 \rangle$ of martensite is $\langle 100 \rangle$ direction. Consequently, it can be concluded that the cell axis (cell growth direction) is parallel to $\langle 100 \rangle$ orientation of austenite. The present result on preferred orientation of cellular structure in weld metal is in good agreement with Rosenberg's work in Ag-Pb cast structure [50]. However, the technique used in this study is very simple, i.e., etching the brittle fracture surfaces and/or analyzing the cell

direction by the etch-pit technique. Therefore this method seems to be useful for analyzing the brittle fracture surface with respect to solidification aspects. It should be noted here that the cell growth direction is determined by the crystallographic orientation of columnar grains but the growth of columnar grains are affected by the temperature gradient at the solid-liquid interface, i.e., by weld pool shape.

B. Weld Cycle Simulation.

As a result of overlapped 'bead-on-plate' welds, the subsequent passes were found to be very effective in destroying the large columnar grains and also the coarsened HAZ grains. However, it was not possible to evaluate the toughness improvement only with the microstructural examination. In order to obtain a better understanding of the various structural changes in HAZ as a result of multipass thermal cycling and their effect on the mechanical properties, particularly on cryogenic toughness, various simulation studies on 12Ni and 9Ni steels were conducted as described in Section II-B.

1. Fe-12Ni-0.25Ti Alloy.

Thermal cycling studies conducted on 12Ni alloy were performed with mainly single cycle thermal treatment on one of two starting conditions. The two starting conditions are the as-annealed condition, which was used as a crude representation of the initial condition of the weld deposit and the "2B" condition, which represented the initial state of the heat-affected zone.

Regardless of the peak temperature, number of cycles, and starting conditions, none of the specimens tested contained the retained austenite phase, even at room temperature. Moreover, their hardness values kept constant at around 98 on the R_B scale.

As-annealed Condition. Figure 15 shows the microstructure changes and Fig. 16 the change in impact energy when as-annealed 12Ni specimens are given rapid thermal cycles. The original as-annealed structure, Fig. 15-a, has about a $60\mu m$ grain size and

fractures in a cleavage mode with an impact energy of *wig* 10 ft-lb (14 Joule) at 77K. The specimens reheated below the A_c temperature (678°C) retained the original grain size, low toughness and brittle fracture mode. Cycling to near 800°C peak temperature destroys the original structure and creates non-uniform irregular grains (Fig. 15-c). The grain size here varies from 10 to 50 μ m. The impact toughness is dramatically improved, to *wig* 150 ft-lb (210 Joule) as shown in Fig. 16, and a dimple-rupture type fracture mode is established. When the cycle reaches a peak temperature >1200°C, however, grain growth takes place (Fig. 15-d) and leads to low toughness in a brittle mode. It is interesting to note the wide range of peak temperatures over which the toughness is improved, in contrast to the narrow range for conventional heat treatment, as found by Yokota, et al. [52] for the Fe-12Ni-0.5Ti alloy.

"2B" Condition. The results of the single cycle HAZ simulation done on the 2B heat-treated specimens are shown in Figs. 17 and 18. The microstructures presented in Fig. 17 document that fine grain size is retained until the peak temperature reaches about 1000°C but severe grain growth takes place above 1200°C.

The Charpy impact energy is improved for peak temperature in the range 700-1100°C, as shown in Fig. 18, and is about 50 ft-lb (70 Joule) higher in the case of the 700°C cycle. The microstructural source of this improvement is not yet clear, but a similar behavior was found in the real HAZ Charpy impact test, as described in the next section. For cycle temperatures between 800°C and 1100°C, the toughness reached a plateau at a level slightly higher than that of the initial 2B condition. Cycle temperatures higher than 1100°C induced significant grain growth (Fig. 17) and resultant low toughness by an upward shift of the ductile-to-brittle transition temperature after cycle. The original high toughness, however, can be recovered with a second thermal cycle at 800°C by accompanied grain refinement. In contrast, the toughness values shown in Fig. 18 are little affected by second tempering cycles at or below 600°C. This indicates that only the austenitizing cycle ($T > A_f$ temp) is effective in improving the

toughness of grain-coarsened HAZ in 12Ni welded joints. The main source of this improvement appears to be the grain refinement through the $\alpha \rightarrow \gamma \rightarrow \alpha$ cycle resulting in a decrease of DBTT to below the testing temperature (77K).

2. 9Ni Steel.

Thermal cycling studies on 9%Ni steel were conducted by applying single or multiple thermal cycles on the 2BT-treated specimens that contained about 12-14% retained austenite in a ferrite matrix. A previous study [24] on the QT 9%Ni steel reported that significant amounts of austenite were retained after thermal cycling and that a good correlation existed between volume fraction of austenite in the simulated HAZ specimens and the 77K impact toughness levels. However, Kim et al. [25] recently reported the retained austenite phase was completely removed after rapid austenitizing cycles on the QT-treated 6 and 9% Ni steel resulting in a significant drop in upper shelf energy. Both reports are in good agreement on the beneficial effect of retained austenite on cryogenic properties but the presence of retained austenite after austenitizing cycles is in gross disagreement between these two. Therefore, the study in this section is aimed at providing direct evidence on the existence or absence of retained austenite phase in the cycled specimen and at establishing systematic microstructural changes during multicycle treatments imposed on HAZ.

Single Cycle. The retained austenite content, the 77K Charpy impact toughness, and room temperature hardness are plotted in Fig. 19 as a function of peak temperature in a single thermal cycle. Peak temperatures below the A_s temperature ($\approx 630^\circ\text{C}$) caused no apparent change in the alloy; the 77K Charpy impact energy, hardness, and the fraction of retained austenite remained unchanged. Above 630°C the retained austenite content dropped precipitously, and no retained austenite was detected for peak temperatures above the A_f temperature ($\approx 715^\circ\text{C}$). The hardness curve also shows a sharp transition between these two temperatures (A_s and A_f) from low hardness (Rc 18) to a high value (Rc 34). The transition in hardness indicates tensile

property changes in the specimen cycled to above the A_c temperature. Kim et al. [26] reported that the yield and ultimate tensile strengths of rapidly austenitized (up-quenched) Fe-6Ni steel after QLT treatment are nearly twice as high as those in the QLT treated condition. The increase in hardness and strength seems to be due to the carbon dissolving into solution in the martensite since no austenite, which is a carbon-rich phase, is present in these specimens. The absence of retained austenite was also confirmed by direct TEM observations. Figure 20 shows the transmission electron micrographs of 2BT-treated 9%Ni steel. As shown in this micrograph, the 2BT-treated base metal consists of retained austenite and well developed polygonized ferrite cell structure. X-ray diffraction of this specimen revealed that about 13 percent of retained austenite was present at 77K. The austenite islands are typically of submicron size, elongated shape, and are precipitated mostly along the cell boundaries or packet boundaries. Figure 21 shows a corresponding transmission electron micrograph of a specimen cycled to 750°C which is slightly higher than A_f temperature. This specimen has a highly dislocated lath martensite structure and very clean boundaries. As shown in its selected area diffraction pattern (Fig. 21-b) retained austenite was not detected at all in this specimen. It demonstrates the absence of retained austenite after single cycle over A_f temperature and support the indirect result of x-ray diffraction analysis.

The specimens cycled to between A_c and A_f temperatures lose part of their retained austenite accompanied by the deterioration of 77K impact toughness. Eventually, 77K impact toughness reaches ≈ 65 ft-lb (88 joules) at 730°C which was preserved until the peak temperature exceeded 1000°C. While the impact toughness was relatively low over the range 715-1000°C, the fracture mode was ductile rupture, showing that the ductile-to-brittle transition temperature remained below 77K. Above 1000°C grain growth was observed. Peak temperatures above 1200°C led to large prior austenite grain sizes (up to 400 μm Fig. 23-b) resulting in very low toughness, 17 ft-lb (23 Joule), in a brittle fracture mode (Fig. 24-a); the ductile-to-brittle transition temperature was

raised above 77K.

These results suggest that the destruction of the 2BT structure on rapid cycling occurs in two steps. For peak temperatures in the range 650-715°C the precipitated austenite disappears causing a decrease in upper shelf toughness and an increase in hardness while preserving a fine effective grain size and a low ductile-to-brittle transition temperature. The fine substructure begins to be destroyed at peak temperatures above 1000°C, causing a further loss in toughness due to an increase in the transition temperature.

Multiple Cycles. In order to simulate the microstructure in the heat-affected zone near the fusion line of a multi-pass weldment, specimens which had been rapidly cycled to 1200°C were given additional thermal cycles to lower peak temperatures. The multiple cycling treatments were selected on the basis of work done by Tamura, et al. [24] on quench-and-tempered 9Ni steel, and are shown on the x-axis of Fig. 22. The y-axis plots the 77K Charpy values, content of the retained austenite and hardness values as a function of the heat treatment. It also shows that no retained austenite was detected in any of the thermally-cycled specimens. The highest impact value was obtained in the specimens cycled to 800°C followed by a 600°C cycle. The first addition of 800°C cycle raises the impact toughness from 17 ft-lb (23 joule) to \approx 70 ft-lb (95 joule) and the subsequent 600°C cycle raises it further to 150 ft-lb (203 joules). The microstructure and SEM fractograph of each condition are shown in Figs. 23 and 24 respectively. The dominant microstructural change wrought by the 800°C cycle is a refinement of effective grain size (Fig. 23-c). This results in suppression of the DBTT to below 77K and a toughness level almost the same as that of 2BT-treated specimens cycled over the A_f temperature (Fig. 19). The dramatic improvement in toughness after the 800°C cycle contrasts with the negligible effect of a 600°C cycle imposed directly on a sample which had not experienced the intermediate 800°C treatment. Even with the significant improvement in the triple-cycled (1200 + 800 + 600(deC) specimen, the optical pic-

tures shown in Fig. 23-d give little information about the microstructural source of this improvement.

The only noticeable difference between double- and triple-cycled specimens is that the grain or packet boundaries are revealed clearly only in 600°C cycle specimens. The packet size measured in the triple cycled specimen was about 5 μm , so it is also expected to be the size of packets in double (1200°C, 800°C) cycled specimens. The fact that packet or grain boundaries are revealed in the 600°C cycled specimen but not in the 800°C cycled specimens indicates assorted microstructural change favored along the boundaries take place during the last 600°C cycle.

In order to investigate the details of microstructural change and source of toughness improvement during the 600° cycle, double and triple cycled specimens were studied with transmission electron microscope. Figure 25 shows the typical TEM micrographs of double cycled specimens. As shown in this micrograph, heavily dislocated martensite laths were grouped in parallel arrays but in two different orientations, i.e., [100] and [111]. The occurrence of two mixed orientations was reported [46] to be observed in the martensitic structure in a unit of group of laths rather than an isolated lath scale. No second phase such as austenite or cementite precipitates were observed in this specimen. This suggests that the microstructural features of the 800°C cycled specimen are quite the same as that of the as-quenched condition except for the misorientation between laths within a packet. Upon addition of a tempering cycle to 600°C, as shown in Fig. 26-a, a recovery reaction takes place to some extent and consequently the lath boundaries become unclear compared with the micrograph shown in Fig. 25. It is also noted that cementite precipitates were formed discontinuously along the lath boundaries as shown in its dark field micrograph (Fig. 26-b). The cementite precipitates were also observed along the packet and grain boundaries. Therefore, it was concluded that the development of boundaries in the etched 600°C cycled specimens can be attributed to the cementite precipitates formed along these boundaries.

Accordingly, the high level of hardness (Figs. 20 and 22) and low upper shelf toughness registered in the specimen cycled over A_1 temperature are attributable to the supersaturation of carbon in the martensite matrix, while the low hardness and high upper shelf toughness in the in the 600°C cycled specimen are due to the carbon getting by cementite formation during the short tempering process. It is also worth noting that the lowest hardness was recorded in the 2BT-treated base metal where carbon is gettered into the soft austenite phase almost completely. This indicates that carbon getting in the form of cementite precipitates during rapid tempering cycles may be less complete than in retained austenite after long time tempering treatments and/or that the cementite precipitates may act as the precipitation-hardening constituent.

C. Microstructure of Full Thickness Weldment.

1. Grain Refinement.

Figure 27 shows the macro- and microstructures of a completed 12Ni weldment with a 0.7 kJ/mm heat input. The HAZ of each bead deposited reheats, recrystallizes and breaks up the original cast columnar microstructure (Fig. 27-a). Thus, the whole weldment is repeatedly transformed, refined, and possibly tempered during fabrication. While a few isolated islands of partially refined structure remain (Fig. 27-d), throughout the greater part of the weld volume both the coarsened HAZ and the large columnar grains are broken up to produce a fine-grained structure (Figs. 27-d and -e). A similar grain refinement was attained with a 1.7 kJ/mm heat input. The grain size of the irregular grains is in the range 5-10 μm in the well-refined regions.

As in the case of grain-refined 12Ni steel, the multi-pass GTA weld of 9Ni steel was effectively grain refined in both the weld metal and heat-affected zone. While there were some islands of larger grain size at the root and final pass region which apparently represent a poor overlap of subsequent weld passes, a reasonably uniform grain size was obtained through the weld region. A full thickness view of the micros-

structure revealed in the single bevel joint of 9Ni steel is shown in Fig. 28.

2. Retained Austenite.

Applying the method described in section II.C., the volume fraction of retained austenite is plotted as a function of distance from the fusion line as shown in the insert to Fig. 32. In agreement with the result [53] obtained earlier in welding of QT-9Ni steel with ferritic filler metals, no austenite was detected within the ferritic weld deposits with either 9Ni or 12Ni base plates. However, the austenite profile through the HAZ is expected to differ depending on the base plate since the 9Ni base material contains 14% austenite while 12Ni plate has none. In the HAZ of 12Ni joint, formation of austenite at the tempered region was expected but no austenite was detected throughout the welded joint, i.e., from weld metal to base metal. This indicates that weld thermal cycles in the tempering temperature range are not sufficient to form a stable austenite, mainly due to the absence of holding time and the low diffusivity of nickel. Hwang et al. reported [54] that it took at least 30 min. of tempering at 550°C before a measurable amount of austenite (larger than one percent) was formed in 2B-treated 12Ni plate. It also supports the present result that the formation of austenite is not expected during a weld tempering cycle.

But a 9Ni joint is quite different from a 12Ni joint because a 9Ni base metal contains a substantial amount of austenite in the 2BT condition. X-ray diffraction analysis shows that the volume fraction of austenite in the 9Ni joint decreases gradually through the heat-affected zone from that of the base metal to a negligible amount at the fusion line. Its gradual change is shown in Fig. 29. The decrease in austenite content through the HAZ ought to be due to weld thermal cycles over the A_1 temperature, as expected from the result of the HAZ simulation study. The result shown in Fig. 29 is quite similar to that of Mahin et al. [53] but is in some disagreement with the earlier observations of Tamura et al. [55] on welding of quench-and-tempered 9Ni steel with ferritic filler metal. Tamura et al. reported an increase in retained austenite in the

heat-affected zone to approximately 10% from a lower value of 4% within the base metal. They also found a significant amount of austenite retention within the weld metal, and argued that the austenite fraction is well correlated to cryogenic impact toughness [24,55]. In the present work the austenite volume fraction decreases monotonically through the heat-affected zone and has no obvious correlation with the variation of impact toughness through the weld region, which will be described in the next section, D.2. The reason for this discrepancy is not clear but is presumably due to the difference in heat treatment condition of base plates, i.e., quench-and-tempered (QT) vs grain refined and tempered (2BT). and/or the difference in measuring technique, i.e. $(111)_{\gamma}/(110)_{\alpha}$ vs. $(220)_{\gamma}+(311)_{\gamma}/(211)_{\gamma}$.

D. Mechanical Properties of the Weldments.

1. Tensile Properties and Hardness.

The results of tensile tests of 12Ni joints welded with filler B are shown in Table IV along with those of the base plates [7,9]. The tensile properties in the transverse direction compared closely with those of the 12Ni base metal in the case of the 0.7 kJ/mm heat input but were slightly lower for the higher heat input of 1.7 kJ/mm. It was confirmed by etching the broken specimens at 77 and 300K that the fracture occurred outside the weld metal, perhaps near the base metal/HAZ boundary. Since the specimen was severely deformed in the fracture region, it was not possible to define an exact fracture site. The tensile data indicate that the yield strength of the weld metal is the same or higher than that of the base plate. Room temperature micro-hardness tests also give higher values in the weld metal ($H_v = 290 \text{ Kg/mm}^2$) than in the HAZ ($H_v = 280$) or base metal ($H_v = 260$). As a result, the joint efficiency of the ferritic weldments (expressed as the ratio in percent of the weld joint strength to the strength of the base metal) [56] is expected to be almost 100% at both room temperature and 77K. The increased strength of the weld deposit over the heat-treated base plate seems to be

contributable to the high density of imperfections in the as-welded structure , as well as the higher nickel content in the weld deposit.

The tensile tests were not performed on 9Ni weldments but the higher hardnesses recorded in the HAZ (Rc 26) and weld metal (Rc 24) relative to base metal (Rc 18) indicate higher strength in the welded region than in the base metal.

2. Charpy V-notch Impact Toughness.

a. 12Ni Welded Joint. Charpy impact tests were conducted at 300K, 77K, and 4.2K to give a general indication of the toughness of the welded plate. Figure 30 shows the variation of impact toughness with notch location at 77K and 4.2K in the single bevel joint welded with filler B. The HAZ has the highest impact energy values than the base plate. It fractures in a ductile mode at 77K but sustains some quasi-cleavage at 4.2K.

This slight brittleness at 4.2K in the single bevel joint groove was completely suppressed in the single V joint. As shown in Fig. 31, filler B weld metal deposited in the V-joint with either of the two levels of heat input maintained high impact values at liquid helium temperature regardless of notch orientation. SEM fractographs taken from broken specimens at 77K and 4.2K show a completely ductile mode. The impact DBTT of filler B weld metal was, hence, successfully suppressed to below liquid helium temperature.

On the other hand, the impact toughness of filler A was much lower than that of Filler B, particularly at 4.2K as shown in Table V. The lower toughness of the filler A weld metal is, apparently, a microstructural effect. Examination of low toughness filler A specimen revealed two types of inclusion particles: a small spherical type often found inside fracture dimples in the ductile region, and a large, round or irregular type which was often observed in the brittle region. These two kinds of particles are shown in Fig.

32, with the EDAX analysis of each. The spherical particles within dimples always registered Ti and S while the irregular particles in the brittle region showed Mn, Si, and Ti without any trace of S. The Auger analysis of the Ti inclusions shows that titanium can act not only as a good oxidizer but also as a scavenger of deleterious elements such as carbon and sulfur. The full Auger spectrum of Ti inclusions is presented in Fig. 33 with that of the matrix for comparison. In filler B weld metal all the particles inside the dimples are the spherical Ti inclusions since no Mn or Si were added in filler B. Therefore, the low toughness accompanied with Filler A seems to be attributed to the large oxide particles of Mn and Si.

Table V also shows an effect of weld geometry: the DBTT of filler A is lower than 77K in the single V joint but higher in the single bevel joint. This behavior apparently reflects the influence of weld geometry on grain refinement; the single bevel joint has a lower potential for grain refinement along the fusion boundary during multi-pass welding. Optical examination of the single bevel joint showed that the beads just beside the straight joint side retained the as-cast columnar structure, particularly near the root pass.

b. 9Ni welded joint. The results of Charpy impact testing at 77K and 4.2K are listed in Table VI and are compared with those obtained for 12Ni steel welded with the same filler metal, filler B, and similar procedures. The variation of impact toughness through the heat-affected zone at 4K is also plotted in Fig. 34 with that of the 12Ni joint.

The Charpy impact energy of the welded 9Ni steel is relatively flat through the heat-affected zone and reaches a maximum within the weld metal. The sharp maximum in impact toughness within the heat-affected zone which was found in 12Ni steel is not present. Combining this result with that of retained austenite shown in Fig. 29, it

demonstrates that there is no obvious correlation between the impact toughness and the retained austenite level remained in the HAZ of 9Ni steel.

.PP The relevant scanning electron fractographs of the specimens broken at 4K are presented in Fig. 35. The impact ductile-to-brittle transition temperature of the ferritic weldment in 9Ni steel is also below liquid helium temperature. There was no evidence of fusion zone brittleness. While there is a slight drop in Charpy impact energy near the fusion line, the fusion zone fracture was ductile, and cracks initiated from the heat-affected zone did not follow the fusion boundary. Based on the heat cycle results, the lower impact value near the fusion line may be attributed to the cementite precipitates which can offer additional nucleation sites for micro-voids during ductile failure process.

3. Fracture Toughness.

a. 12Ni welded joint. Since the filler A tended to become brittle at 4.2K in Charpy impact tests, further fracture toughness tests were done only on joints welded with filler B. Figure 36 shows typical load-COD curves obtained from three-point bend tests with a clip gage at 77K with three different locations of the fatigue crack. All the specimens seemed immune to catastrophic crack propagation; the specimens were fully plastic and the pre-induced cracks grew slowly in a stable manner until the test stopped. A value of $K_q \approx 75 \text{ksi}\sqrt{\text{in}} (83 \text{MPa}\sqrt{\text{m}})$ was computed from the linear portion of these curves. The fracture toughness values computed by the 'equivalent energy' method are presented in Table VII. The estimated fracture toughness, $K_{IC}(E)$, of HAZ and weld metal is either close to or even higher than that of 12Ni base metal. It is noted that the highest toughness value was obtained in the HAZ as is the case for Charpy impact values. Improvement of toughness in the HAZ of 12Ni alloy was also reported by Devletian et al. [23].

Since weld metal showed lower 77K toughness than the HAZ, further tests at 4.2K were done only on weld metal specimens. The results of the compact tension fracture toughness tests of weld metal at 77K and 4-6K are also shown in Table VI and Fig. 12. The crack in the compact tension specimen grew without any catastrophic propagation at 77K but at 4-6K gave a serrated load-deflection curve up to the maximum load, then propagated discontinuously (Fig. 37). The calculated K_q values were 138 ksi $\sqrt{\text{in}}$ (152 MPa $\sqrt{\text{m}}$) at 77K and 115 ksi $\sqrt{\text{in}}$ (127 MPa $\sqrt{\text{m}}$) at 4-6K.

Whatever the testing method at 77K, the estimated fracture toughness of the weld metal is comparable with the toughness of the base plate (338 MPa $\sqrt{\text{m}}$). A lower boundary for the fracture toughness of the 4-6K specimens was calculated using equation (2). The area under curve, A_1 , was taken to the maximum load point. The calculated K_{IC} value was 160 ksi $\sqrt{\text{in}}$ (176 MPa $\sqrt{\text{m}}$), average of two tests. Examination of the fracture surface along the fatigue crack line revealed that the fracture mode was completely ductile mode at 77K but a mixture of dimple rupture and quasi-cleavage at 4K as shown in Fig. 38.

The exact nature of the serration mode and the details of J-integral fracture toughness and fracture mode of weld metal at 4.2K will be presented in the following section.

b. *9Ni welded joint.* For 9Ni steel, the preliminary test employed deep-notched (a/w 0.6) three-point bend specimens of 10 mm thickness for the rough indication of J_{IC} values at 77K. The results of three-point bend tests (stroke control) at 77K showed that the specimens from the base plate and weldment showed no evidence of fast crack propagation at 77K. The HAZ specimen showed only a slight indication after the peak load had been passed. The typical load vs. load-point displacement curves are shown in Fig. 39. Assuming that the crack started to grow at the maximum load point, the frac-

ture toughness was estimated using equation (3) , and converted to plane strain fracture toughness using equation (5). The estimated values are tabulated in Table VIII. In order to get a valid J_{IC} value at this level of toughness, the thickness, B , and initial ligament, b , should be longer than 0.8 cm according to the following equations:

$$B > 25 \frac{J_Q}{\sigma_f} \quad (6)$$

and

$$b > 25 \frac{J_Q}{\sigma_f}$$

So the valid J_{IC} values could not be obtained in Charpy size specimen because the ligament, b , in this specimen geometry is far shorter than that required. In order to obtain a valid J_{IC} value, the modified compact tension specimen shown in Fig. 8-c was employed and testing with J_{IC} testing procedures. The load vs. load-point displacement curves obtained in the J_{IC} test at 77K are drawn in Fig. 40 (unloading curves are omitted during drawing). As shown in these curves, the weld metal specimen is still immune to catastrophic crack propagation but the base metal and HAZ specimens display unstable propagation after passing maximum load. Since, the first crack advance points, where the fracture toughness (J_{IC}) is determined, were monitored near the maximum load points in all the specimens tested at 77K J_{IC} value itself was not affected by the unstable crack propagation. It is also interesting to note that the fracture surface of the post-tested specimens tend to be flat and lack shear lips as unstable crack propagation becomes active after passing maximum load. Each unstable propagation shown in the load vs. load-point displacement curve (Fig. 40) correspond to a series of thumb nail marks which are visible on the fracture surface with the naked eye as shown in Fig. 41. Another thing to note in Fig. 41 is that the HAZ specimen has the abnormal shape of fatigue crack front resulting in non-valid toughness value. Since this specimen is from a double-V weld joint, the center part of the specimen lies far inside the base metal region and the edge part is close to the fusion

line. So the fatigue properties of the center of the HAZ specimen are different from that of the outer edges. Based on the length of fatigue precrack, it is expected that the fatigue crack growth rate in the HAZ is much faster than that in the base metal. Even though it is beyond the scope of this study, a fatigue test is also necessary for complete evaluation of the 9Ni weld joint.

The plane strain fracture toughness values, $K_{IC}(J)$, converted from J_{IC} using equation (5) are listed in Table VIII. Based on 77K data, the weld and HAZ fracture toughness values compare favorably with that of the base metal: 265 ksi $\sqrt{\text{in}}(292\text{MPa}\sqrt{\text{m}})$ in HAZ and 332 ksi $\sqrt{\text{in}}(365\text{MPa}\sqrt{\text{m}})$ in weld metal as compared with 294 ksi $\sqrt{\text{in}}(323\text{MPa}\sqrt{\text{m}})$ for 2BT-treated 9Ni steel. It is worth noting the fact that the base metal toughness deteriorates in the HAZ of the 9Ni weldment while it is improved in the HAZ of 12Ni welds. This reflects the difference in microstructural response on the weld thermal cycles between 9Ni and 12Ni HAZ's.

The trends in fracture toughness observed with modified compact tension specimens were similar to those with three-point bend specimens, but the $K_{IC}(J)$ fracture toughness values obtained by valid j_{IC} testing are much higher than the invalid values, $K_I(J)$, obtained with the small-size three point bend specimens. It seems to be due to the wrong assumption made in the three-point bend tests that the first crack advance occurs at the maximum load point.

As the temperature decreases further down below 77K, the 9Ni weldment, particularly the base metal and HAZ, tend to become brittle and eventually give jagged load vs. load-point displacement curves at 4.2K as noted previously in Fig. 32, and as shown in Fig. 42, the crack grows slowly and steadily with very small amplitude serrations up to maximum load and with rather larger load-drops afterwards. These kinds of serration mode were commonly observed [8,9] at 4.2K tests and have been believed to be

due to adiabatic heating during deformation [9] and not due to an unstable crack propagation [8] as slip or yielding also occurs discontinuously near 4.2K [57]. However, all the R-curves constructed in this study clearly demonstrated that the first crack advance occurs at the first serration accompanied with a cracking sound. It indicates that these continuous serrations are due to the minute pop-in mode propagations occurring successively rather than other means. Accordingly, all the 4K J_{IC} (or K_{IC}) values reported in Table VIII are the ones calculated based on J values at the first serrations marked by arrows on each curve. This means the maximum load, which has been used for estimating K_{IC} values with the equivalent energy method, did not affect J_{IC} values calculated by the J-integral method. If the fracture toughness was estimated with the equivalent energy method, the toughness value was substantially overestimated. For example, the K_{IC} values of the base metal and the weld metal were found to be 170 and $> \text{ksi}\sqrt{\text{in}}$ ($253 \text{MPa}\sqrt{\text{m}}$) by the equivalent energy method but were 100 and 130 $\text{ksi}\sqrt{\text{in}}$ respectively by the J_{IC} method.

One thing to note in Fig. 42 is the load difference between the first serration and the maximum load point. The maximum load on the base metal specimen was reached right after the first serration but that of the weld metal specimen was reached after substantial amounts of deformation. As a result, the maximum load on the weld metal specimen is almost twice as large as that at the first serration. Considering the thickness difference (base metal is 0.7 in (17.8 mm) thick and weld metal specimen is 0.35 in (8.9 mm) thick), it is expected that the load carrying capacity of the weld metal is almost two times higher than that of the base metal.

The early stage of serration and the very high maximum load in the weld metal specimen seems to be based on the microstructural effect of the weld deposits. Examination of whole fracture surfaces illustrated that the fracture mode of 9Ni base metal, which has a uniform microstructure, is quasi-cleavage throughout the fracture surface as shown in Fig. 43-a. But that of weld metal specimen is a mixture of typical dimple-

rupture and a small amount (about 20%) of quasi-cleavage. These two modes are usually divided with very clean boundaries as shown in Fig. 43-b. Therefore, it is reasonable to expect that the early stage of serration is attributable to brittle crack initiation occurring in some localized areas (Fig. 27-d) which were not fully refined by the subsequent weld passes. On the other hand, well refined regions carry the bulk of the applied load through a ductile failure mode. As a result, the abnormal features in load-COD curve of the weld metal specimen is attributable to the non-uniform grain size in the multi-pass weld deposit. This implies that a uniformly refined microstructure is an important factor in increasing the toughness value of ferritic weld metal unless an equivalent energy method is used.

CHAPTER IV

DISCUSSION

The results of mechanical testing establish that grain-refined ferritic steels can be welded with ferritic filler metal without sacrificing toughness in the heat-affected zone and weld metal at temperatures as low as 4K. This success may make it possible to realize several advantages of ferritic weldments in cryogenic structures, including high strength, a complete joint at the fusion boundary, matching low thermal expansion, and the low cost of ferritic consumables. The success of the welding procedure seems attributable to a combination of microstructural changes through the multi-pass welding process and the low interstitial weld deposit of the GTAW. Since the weldments prepared in this study differ from the base plates in composition and thermal history, the resultant microstructures are also different from those of base plates.

A. Effect of Composition.

The weld metal chemistry explored in this work differs from that of the base plate in three respects: the increased Ni content, the addition of Mn and Si (filler A) and the addition of boron (filler B).

1. Nickel Content.

The nickel content was increased to 14 wt.% to err on the side of safety in achieving a low ductile-brittle transition temperature DBTT in the weld metal. It is not clear that this increase is necessary. While a satisfactory DBTT was obtained, the thermal cycle simulation studies suggest that satisfactory properties might also have resulted if the base metal composition had been used.

Current metallurgical understanding does not permit an *a priori* choice of an optimum nickel content for low temperature toughness. While an increase in nickel content is often found to lead to a decrease in the DBTT [58-61] and a decrease in the length of columnar grains in the cast structure [62], the mechanisms of these effects

are uncertain. Floreen et al. [6] reported that there is an inherent effect of nickel that considerably raises the cleavage strength of the ferrite lattice possibly through changing slip characteristics such as increasing the ability to cross-slip. However, the increase of cleavage strength with increased nickel contents to over 10% has not been reported.

In the case of high nickel contents, it is more likely that the primary benefit achieved is indirect through the influence of nickel on the response of the microstructure to thermal treatment.

Previous research [63] suggests that there is an optimum nickel content of the weld filler metal which lies somewhat above that of the base plate. In the GTA welding of 9Ni steel an increase in nickel content from 5 to 11 wt.% gave a monotonic improvement in toughness at 77K, but toughness deteriorated when the nickel content was increased further to 17 wt.%. The problem at higher nickel content may be associated with an unstable austenite retention in the weldment, as is apparently the case in 18% Ni (250 grade) maraging steel [64].

2. Manganese and Silicon.

Manganese and silicon are common deoxidizers which were added to filler metal "A" in this research to determine their effect on the final weldment properties. As will be recalled, the 4K Charpy impact values of the weld metals were 53 ft-lb (72 Joule) for filler A and 128 ft-lb (174 Joule) for filler B. This result clearly indicates that their presence led to a deterioration in the weld metal toughness, which seems to be clearly associated with the formation of large (Mn-Si) oxides.

Silicon is often intentionally added to ferritic weldments for 9Ni steel [65] since 9Ni contains a significant alloying addition of manganese, and it is known that a low Mn/Si ratio is needed to obtain efficient removal of deoxidation products to the weld surface [66]. In fact, serious porosity problems have been encountered in ferritic GMA

welding of 9Ni steel with Si-free [54] weld metal and in the welding of low carbon manganese steels [66], apparently because of insufficient deoxidation of the weld deposit. With Si-containing weld chemistries, large (Mn,Si) oxides have been found on the fracture surfaces of ferritic weldments in 9Ni steel [67], and apparently cause embrittlement by mechanisms similar to that noted in the present work. Based on the above discussions, the addition of manganese and silicon in filler wire should be beneficial for getting oxygen but oxides remaining in the weld deposit deteriorate the low temperature toughness mainly due to the large size of their oxides.

3. Titanium.

The results obtained with filler metal "B" in the present work show that manganese and silicon are not necessary alloy additions to the weld metal. The 12Ni base plate alloy contains no manganese, and deoxidation and scavenging is, apparently, efficiently accomplished by the alloy addition of Ti, as was inferred by previous researchers. As shown in the Auger analysis of inclusion particles (Fig. 33), Ti not only acts as a deoxidizer in the weld deposit but also combines with carbon and sulfur to getter other potentially deleterious elements. The majority of these inclusions are less than $0.5 \mu\text{m}$ in size which is much smaller than that of (Mn,Si) oxides found in filler A deposits. In contrast to these beneficial effects, it was reported that the titanium in solution degrades the toughness of a ferritic weld deposit [68,69]. So the addition of titanium should be limited unless the oxygen level in the deposit is high. Given the relative cleanliness of the GTA welding process, the titanium content of the base alloy seems sufficient to ensure a clean and well-gettered weldment. One thing to point out here is the possibility of substitution of titanium with aluminum since both are potential scavengers for deleterious elements such as C, O, and N, and are generally used for grain refining in the multipass weld deposit [70]. According to previous research in NASA Lewis Research Center [23], however, aluminum bearing weld deposits on a GTA welded Fe-12Ni alloy display high toughness only after the post-weld heat treatment

and had very poor toughness in the as-welded condition. Although the source of poor toughness was not reported, the replacement of Ti with Al should be restricted unless the post-heat treatment is permitted.

4. Boron.

Boron was added to filler metal "B" in the expectation that it would act as a strong surfactant in boundaries of the weld metal to prevent intergranular separation, as it does in other alloys [71,72] and to also act as a grain refiner as in carbon steel welds [73,74]. It is also well known that Ti and B inoculations in aluminum melts significantly refine the grain size of the as-cast structure [75-77]. However, its actual role in the weldments studied in this research has not been identified since neither a measurable difference in grain size between filler A and B was observed nor was a trace of boron detected by Auger analysis of the microstructure of fracture surface. Although common grain refining agents are quite effective in reducing the grain size of cast metal, they seem to be relatively ineffective in refining the grain size of as-deposited weld metal. This is because the energy required for epitaxial growth (i.e., growth without nucleation) in weld metal is considerably less than the energy required for heterogeneous nucleation and growth of new grains.

Boron did, however, seem to be beneficial to the welding process. The addition of a small amount of boron to the Fe-12Ni-0.25Ti base plate improved weld metal fluidity in bead-on-plate welding, and it was found that filler "B", which contained 30 ppm boron, produced a more easily controlled weld puddle and better weld beads than did the boron-free filler "A".

B. Effect of Weld Thermal Cycles.

The degree to which microstructural and mechanical property changes arise in multipass weld metal depends not only on the "chemical aspects" of the deposit, but also on the history of the weld thermal cycles. The effect of individual thermal cycles

on low temperature toughness are quite different depending on the peak temperature (i.e., austenitizing vs. tempering cycle) and also on the base metal composition (carbon-free 12Ni vs. carbon-containing 9Ni steel) in the case of the tempering cycle.

1. Cycles over A_f Temperature.

a. Grain Refinement. The low ductile-brittle transition temperature of the ferritic weld metal is simply a consequence of the multipass welding process, which appears to refine the grain size of the weld deposit. A previous report [] on welding of 12Ni alloy with the electron beam welding process illustrated that HAZ toughness at 77K was greatly improved by the fully penetrated second pass while the weld metal toughness was not. In the present study, it was shown that the HAZ of multipass welded 12Ni joint has a higher toughness than the base metal. These results certainly indicate that weld thermal cycles are very effective in improving low temperature toughness through the microstructural refinement by repeated thermal cycles. As shown in Figs. 15 and 16, not all the cycles refine the microstructure but only the cycles whose peak temperatures lie between A_f and $\sim 1000^\circ\text{C}$ are effective. The tempering cycle below A_s temperature does not affect the original grain size and results in no change in the ductile-brittle transition temperature. If the cycle reaches a peak temperature higher than 1100°C , on the other hand, grain growth takes place significantly and results in an upward shift of the DBTT.

In conventional treatment of ferritic Fe-Ni cryogenic steels there are two mechanistically different ways of establishing a fine effective grain size: the direct crystallographic refinement of the martensite through austenitizing treatment, and the introduction of a fine distribution of precipitated austenite through intercritical tempering treatment [125]. In the present case it appears that grain refinement is a direct crystallographic refinement of the deposit and HAZ through the fast $\alpha \rightarrow \gamma \rightarrow \alpha$ cycle since no measurable retained austenite was detected in the 12Ni welded joint.

Several researchers have shown that a rapid austenitizing cycle can accomplish a significant grain refinement of steel and improve its mechanical properties with respect to conventionally treated material. This research involved iron-carbon alloys [78-80] and HY-130 steel (5Ni-Cr-Mo-B) [81]. The research by Porter, et al. [81] on HY-130 steel is particularly relevant, since these workers found that the degree of grain refinement increased with heating rate and also noted changes in dislocation substructure which were more pronounced in specimens given a rapid thermal cycle.

In order to see the rapid cycle effect on grain refinement in the present cryogenic steels, the 2BT-treated 9Ni specimen cycled up to 1200°C (Fig. 23-B) were heat treated in the furnace for 1 hour at 750°C (slightly higher than A_1 temperature) and compared with the specimen cycled to 800°C (double cycled specimen shown in Fig. 23-C). The optical micrographs taken from both specimens after a short time (5 sec) tempering at 575°C to reveal the packet boundaries are shown in Fig. 44. This micrograph clearly shows the finer structure in the rapidly austenitized specimen than in the furnace austenitized one. The 77K impact toughness of rapid-cycled specimens was 70 ft-lb (95 Joule) with a completely ductile fracture mode but that of the furnace-treated specimen was 24 ft-lb (33 Joule) with a quasi-cleavage fracture mode. This fact implies that the ductile-brittle transition temperature (DBTT) of the rapid-cycled specimen was suppressed below 77K but that of the austenitized specimen still remained above 77K. Based on these results, it is confirmed that a rapid cycle, which is the case in weld thermal cycles, is much more effective in refining the microstructure and thus results in a larger suppression of DBTT than the slow heated and long-time furnace heat treatment. As mentioned earlier, the grain-refining effect of the rapid austenitizing cycle of $\alpha \rightarrow \gamma \rightarrow \alpha$ is well documented [78-81] but its details of microstructural sources has not been discussed in the previous literature. Hence, some discussion follows: the austenite formed by shear reversion ($\alpha \rightarrow \gamma$) during fast heating contains a high density of dislocations right after the transformation but loses its dislocations due to excessive

recovery process if the specimen holds at the peak temperature for a long time. If there is no holding time, a high density of defects can offer more dense nucleation sites for martensite laths resulting in a finer packet size (Fig. 42) and possibly a destruction of lath alignment within a packet as shown in Fig. 25. This hypothesis may not be correct and more experimental evidence is sorely needed for a complete understanding of microstructural refinement during fast cycles. In particular, the substructural changes caused by rapid thermal cycling are very important since the $5\mu\text{m}$ apparent packet size of the weldment is considerably above that (about $1\mu\text{m}$) which appears to be necessary to lower the ductile-brittle transition of the base plates below 4.2K [82].

b. Removal of Retained Austenite. As shown in Fig. 19 and 21, the cycles over A_f temperature erase the retained austenite which was formed during the final tempering treatment of 9Ni steel. Therefore the role of austenitizing cycles in 9Ni steel is two-fold, i.e., grain refinement and removal of retained austenite. The absence of austenite after thermal cycling indicates that the retained austenite loses its stability at the austenitizing temperature and correspondingly transforms to martensite along with the surrounding austenite matrix.

In general, the retained austenite has been believed to be stabilized by the alloy segregation which occurs during long time tempering treatment at the low temperature in the $\alpha+\gamma$ region and also by stress generated by phase transformation resulting in volume changes. Through scanning transmission electron microscopy (STEM) analysis, Kim et al. [83] directly proved the chemical enrichment of the substitutional alloying elements such as Ni, Mn, Mo, etc. Many investigators [84-87] indirectly proved that carbon segregation occurs in the retained austenite phase, and is a dominant factor in stabilizing the austenite phase at cryogenic temperatures. It was also demonstrated [84] that the significant increases in toughness after tempering treatments are a direct consequence of the scavenging of carbon or carbide precipitates by the austenite. So there is no doubt that the austenite phase formed during conventional

tempering treatments is enriched in alloying elements, particularly by carbon, and it helps to lower the M_s temperature and increase stabilization even at low temperature.

If the specimen containing the austenite phase was heated over the A_f temperature, the ferrite matrix transforms to austenite and the microstructure at the peak temperature is no longer two phases but a single phase of austenite. Hence, the alloying elements segregated at the sites where the austenite was retained will diffuse out to the transformed austenite. Because of the low diffusivity of substitutional elements, the most favorable elements to diffuse and appreciable distance in a short time are interstitial elements such as carbon. Theoretically calculated mean distances of carbon diffusion during austenitizing cycles are estimated to be at least $3.5\mu\text{m}$ (approximated value for one second holding at 750°C) while the mean distance between retained austenite islands is only about $0.5\mu\text{m}$ or less. Considering the high density of dislocations in the shear-transformed austenite, the mean distance of carbon diffusion in fresh austenite can be greater than that of this theoretical value. Therefore, a mean distance of carbon diffusion during austenitizing cycle is sufficiently greater than the distance between retained austenite islands. It implies that the most important factor, i.e., local segregation of carbon, contributing to the stabilization of austenite is eliminated as a result of an austenitizing cycle over the A_f temperature. This causes the transformation of prior austenite islands to martensite on cooling along with the surrounding austenite matrix. So the final microstructure is the highly dislocated martensite without any second phases as shown in Fig. 24. Due to the absence of a carbon scavenging constituent, the resultant martensite should be supersaturated with carbon.

c. Effects on Toughness. As described in the previous section, the microstructural changes occurring during austenitizing cycles are grain refinement and removal of austenite. In addition, austenitizing cycles on tempered structures change their substructures to highly dislocated martensite. The toughness improvement by refining

the grain size is well explained by changing the fracture mode through the suppression of ductile-brittle transition temperature. However, there has been little attention on grain size effect on the upper shelf toughness, i.e., the impact toughness in the ductile region. Recently, Kim [] reported that the upper shelf toughness remained constant with varying grain size in the 5Ni-0.01C steel. This indicates that the fine grain size is good for suppressing the DBTT but not effective in improving the toughness of the ductile region. Therefore, the improved toughness in the austenitized 12Ni specimen (Fig. 18) and in the HAZ of the 12Ni welded joint (Fig. 30) cannot be fully explained by the grain size effect. With the absence of retained austenite phase in 12Ni alloys, the high density of dislocation generated by $\alpha \rightarrow \gamma \rightarrow \alpha$ cycle may be the microstructural source of this improvement, since the high density of dislocations would give an improvement in local plasticity which might minimize stress concentration at inclusion sites within the steel [88].

In contrast, the effect of an austenitizing cycle on the toughness of 9Ni steel depends on the initial microstructure. If the initial structure is annealed (coarse-grained) condition, the austenitizing cycle improves the low temperature toughness through suppress of the DBTT. This improvement, however, is limited to an intermediate level, about 70 ft-lb (95 Joule) at 77K. This limited improvement is quite in contrast to the large improvement to 150 ft-lb (203 Joule) in the 12Ni alloy as shown in Fig. 16. It illustrates that the level of upper shelf toughness is greatly affected by the carbon content in the martensite structure. If the initial structure is the fine-grained and tempered (2BT or QT) condition which contains retained austenite, the austenitizing cycle reduces the upper shelf toughness significantly even though preserving the low DBTT. This decrease is certainly attributable to the absence of austenite phase after cycling. Since the retained austenite phase in ferritic steels scavenges carbon out of the matrix resulting in an improvement of upper shelf toughness, the toughness of the cycled specimen drops to an intermediate level (~65 ft-lb) accompanied with the reso-

lution of carbon into martensite. Since the grain size has no effect on upper shelf toughness, the intermediate toughness will be preserved even after several cycles unless carbon is gettered again. In summary, an austenitizing cycle on 9Ni steel can either improve or reduce the toughness depending on the initial microstructure while that on 12Ni alloy always improves the toughness regardless of the initial microstructure. This difference is caused by the presence or absence of carbon in the composition of 9 and 12Ni steel respectively.

2. Cycles below A_c Temperature.

a. Cementite Precipitation. The tempering cycle on the carbon-free 12Ni alloy did not show any noticeable change either in microstructure or in toughness. Even in the carbon-containing 9Ni steel, the effect of the tempering cycle was not evident if the carbon is gettered in the retained austenite phase. The effect of tempering cycle on toughness was only observed in the fully martensitic 9Ni structure through the precipitation of cementites.

Generally the tempering process in Fe-Ni-C cryogenic steels include precipitation of cementite, introduction of austenite phase, and polygonization of the ferrite matrix. Previously many investigators [86,87] established that cementite precipitates form in the early stages of tempering and are sacrificed by the formation of austenite in prolonged tempering treatments. This indicates that cementite precipitates are a kind of transition phase on the way to austenite, which is the thermodynamically stable phase. As can be seen in Figs. 22 and 26, cementite particles are present at boundaries despite a very short tempering cycle, and their formation induces an abrupt decrease in hardness. Similar observations were made by Caron et al. [89] in the low carbon martensite. They reported that carbide precipitation, mainly cementite, occurs throughout the matrix and the hardness drops dramatically even after a rapid temper of 690°C for only 0.28 sec. So there is no doubt about the formation of cementite precipitates even with a very short tempering cycle. However, the questions are whether

these cementite precipitates are able to transform to austenite during the tempering cycle and, if they are, how stable is that austenite. Although the transformation mechanism from cementite to austenite is not well established, it is reasonably expected that the transformation trend will be shifted toward shorter tempering time as the tempering temperature increases. In 9Ni-0.1C steel, it was not until 120 hr. tempering at 500°C that any austenite transformed from cementite precipitates was observed, and this transformation was completed within 120 hr at 550°C [86]. In order to see more details of the tempering process at higher temperature, the annealed (1050°C/2 hr) 9Ni specimens were tempered in the furnace (temperature set at 590°C) for the various times. The results are shown in Fig. 45. As can be seen in this figure, no retained austenite was detected up to 20 minutes tempering. In other words, a quite long incubation time is necessary to form a stable austenite phase from cementite precipitates. According to this result, the formation of stable austenite is hardly expected during the tempering cycle because of the absence of holding time.

In summary, a weld tempering cycle is quite enough for the formation of cementite precipitates through the local diffusion of carbon in the highly dislocated structure but is not enough for the further transformation of cementite to austenite. The formation of cementite precipitates is a direct consequence of tempering the carbon-solutioning martensite. Accordingly, such a microstructural change cannot take place if the alloy does not contain diffusible carbon or if all the carbon in the steel is gettered by the retained austenite. That is why the microstructures of carbon-free 12Ni alloy and the 2BT-treated 9Ni steel are hardly affected by tempering cycles.

b. Effects on Toughness. Due to the absence of microstructural change in the 12Ni alloy and the 2BT-treated 9Ni base metal, the tempering cycle does not affect the original toughness, as shown in Fig. 16, 18, and 19. On the other hand, since the tempering cycle plays an important role in precipitating cementites, its effect on toughness becomes evident in the as-quenched 9Ni steel. The direct consequence of

cementite precipitates is a scavenging of carbon out of the matrix resulting in clean matrix.

In low carbon martensite, Abron [90] demonstrated that decreasing carbon content of the martensite is the outstanding factor in increasing the toughness. Thus, it is highly desirable to keep such interstitial impurities to a minimum. The simple way to accomplish this is the use of the purest possible raw materials as present in 12Ni alloys and filler metal. However, a more subtle possibility is to heat treat the "impure" material to give well-dispersed, but a small amount of second phase which has greater solubility for the impurities than does the primary phase. This is the well-known scavenging effect of retained austenite introduced during tempering treatment since the solubility of interstitial species such as carbon are far higher in austenite than in martensite (or ferrite). As far as carbon gettering is concerned, there is no doubt that the cementite precipitates formed during the tempering cycle play exactly the same role as that of retained austenite since they also drain off carbon from the matrix. The only difference may be the amount of carbon gettered in each phase. If the amounts of carbon gettered by either cementite precipitates or retained austenite are the same, the toughness enhancement of the ferrite matrix will be the same. Figure 45 can clearly rationalize this hypothesis since a dramatic improvement in upper shelf toughness is accomplished by the cementite precipitation during the early stage of tempering or tempering cycle. When austenite does form after 20 minutes at 590°C, however, only a slight improvement in toughness is obtained. Therefore, the toughness improvement by the last tempering cycle in the triple (1200 + 800 + 600°C) cycled specimen (Fig. 22) can be explained as the result of the enhancement of toughness in the matrix through the formation of cementite precipitates. Recently, Strife et al. [87] reported that three-step (QLT) heat-treated 5.5Ni steel containing cementite precipitates showed superior toughness to that containing 3.5 vol.% of austenite. It also implies that cementite precipitates are as good a constituent for improving the low temperature

toughness as the retained austenite is. Specially, both results provide more direct evidence of toughness improvement through carbon scavenging since cementite precipitates are straight-forward evidence of carbon removal from the matrix. It is worth noting that the scavenging of carbon through the cementite precipitation improves the upper shelf toughness significantly but does not improve the lower shelf toughness. Therefore, refinement of the grain size has to precede cementite precipitation for good HAZ toughness at cryogenic temperatures.

Although the high toughness can be obtained with the precipitation of cementite, some doubt remains as to how close the amount of carbon gettered by cementite precipitates during the weld thermal cycle that gettered in the form of retained austenite. A precise resolution of this question is not possible at this moment but one can expect that cementite precipitation gives a less amount of carbon scavenging because of the limited time for tempering in the weld thermal cycles. Suppose the same amount of carbon is gettered in both cases. another doubt still remains as to whether the gettering of carbon in the form of cementite precipitates can promote toughness up to the same level as when in the form of retained austenite. Since the cementite precipitates are generally believed to make void nucleation sites, toughness improvement is expected to be less even with the same amount of carbon scavenging. However, it should be noted here that there is a basic difference between sulfides and carbides in that carbides, unlike sulfides, do not crack or decohere at low strains [91]. Consequently with carbides in the structure, the steel can undergo significant deformation prior to void nucleation at the carbide precipitates. It indicates that the easy void nucleation at other particles such as oxides and sulfides, which decohere or crack almost immediately as strain is applied or even prior to straining [92] may limit the void nucleation and growth at cementite precipitates. Detailed SEM and EDAX studies on triple (1200 + 800 + 600) cycled specimen showed that almost all the particles inside the dimples were believed to be either oxides or sulfides. However, this observation

was limited to the rather large particles because of the relatively poor resolution of the microscope. In order to figure out whether voids can form at cementite precipitates, it will be necessary to observe the replica taken from the fracture surface in TEM.

From the above discussion, the adverse effects of cementite precipitates on toughness cannot be ruled out completely. Thus, the slight difference in impact toughness between cycled (1200 + 800 + 600°C) and 2BT-treated specimens may be caused by the two possible features of cementite precipitates over retained austenite, i.e., less the amount of carbon scavenging and void nucleation at cementite precipitates. This difference, 20 ft-lb (27 Joule), is quite small compared with the toughness improvement, to 150 ft-lb (203 Joule), by the cementite precipitation. This fact is very important in evaluating the weldability of austenite-containing ferritic nickel steels. If the retained austenite is the only factor in improving the low temperature toughness, the weldment of these steels has to be postweld heat treated in order to introduce the austenite in the HAZ. As the present result demonstrated, fortunately, the comparable toughness with the base metal can be recovered in the as-welded condition through the in-process formation of cementite precipitates during multiple pass welding. This fact can provide a microstructural support on the general statements [93] that 9Ni steel has good weldability without any post-heat treatment.

C. Ferritic Weldment for 4.2K Use.

1. Base Metal.

The high strength (1.4 GPa yield strength) and good 4.2K toughness of the 12Ni alloy is recognized as achieved not only by microstructural refinement through a unique 2B heat treatment but also by the exceptionally clean chemistry. Anticipating the commercialization of this alloy, it is important to establish tolerance limits for common impurity elements such as Mn, Si, C, and others. Since commercially available 9Ni steel contains reasonable amounts of these impurities and has been used

widely in cryogenic systems, this material has been chosen for this purpose and was modified using the 2BT heat treatment.

While a fracture toughness of $163 \text{ ksi } \sqrt{\text{in}}$ ($179 \text{ MPa } \sqrt{\text{m}}$) was reported [97] to be obtained for 2BT-treated 9Ni steel at 4.2K, this value was somewhat overestimated due to the rough calculation using equivalent energy method. In the present study, the same level of toughness value was obtained with equivalent energy method but a reliable 4.2K toughness value, $K_{IC}(J)$, obtained with J_{IC} testing was substantially lower ($100 \text{ ksi } \sqrt{\text{in}}$). It was readily noticed that this difference was due to the minute pop-in (separation) occurring before reaching maximum load. SEM observations shown in Fig. 43-A also indicates that this steel is quite brittle at 4.2K even after the 2BT treatment. According to these results, it can be concluded that the 2BT heat treatment increases the toughness of 9Ni steel from $72 \text{ ksi } \sqrt{\text{in}}$ ($79 \text{ MPa } \sqrt{\text{m}}$) in QT condition [9] to $100 \text{ ksi } \sqrt{\text{in}}$ ($110 \text{ MPa } \sqrt{\text{m}}$) but this improvement is not enough to change the fracture mode from brittle to ductile at 4.2K. It suggests more efforts on alloy development are really necessary to suppress the ductile-brittle transition temperature (DBTT) safely below liquid helium temperature. Since the grain size is the dominant factor in decreasing the DBTT, further refining the present microstructure, needless to say, is necessary for the final goal. The effective grain size, which has been defined as the facet size in the brittle fracture surface was measured in the 2BT condition to be around $10 \mu\text{m}$ (Fig. 43-A). So the fastest way to get close to finer grain size would be to understand the effectiveness of each step of the 2B heat treatment on microstructural refinement and to establish how the optimum microstructure can be created most efficiently. If the goal is not reached by thermal treatment alone, the introduction of a controlled rolling process or thermomechanical treatment can be considered for further improvement. The usefulness of controlled rolling in refining austenite grain size was well recognized in the HSLA steels [94], particularly in Nb-treated steel [95], and also has been attempted in the cryogenic 5.5Ni steel [96]. In 5.5Ni steel, it was reported that con-

trolled rolling followed by an austenitizing treatment was more effective in refining the prior austenite grain size than a double austenitizing treatment. This seems to be attributable to the creation of a higher density of potential austenite nucleation sites by the controlled rolling. Therefore, the slight modification of the ZBT heat treatment might be considered to include the thermomechanical treatments.

2. Ferritic Weld Metal.

There are two aspects in improving low temperature toughness of weld deposits, i.e., "chemical" and "microstructural" aspects. Since the effect of each alloying element was discussed in the first part of this chapter, mainly the effect of the "microstructural" aspect on toughness will be discussed in this section. Considering cryogenic toughness, obtaining the appropriate microstructure is a more important and desirable approach than changing chemistry because the DBTT is more severely affected by the grain size than by alloying content.

As mentioned previously in the section III-3 describing J_{IC} test results at 4.2K, a uniform microstructure appears to be one of the critical factors in improving the fracture toughness value at 4.2K. If the toughness of the weld metal is evaluated by the Charpy impact energy, the uniformity in microstructure may not be so important. Since the value recorded in a Charpy impact test is the total energy observed during crack initiation and propagation throughout the specimen, it is slightly affected by the local existence of a small amount of brittle fracture at the notch tip. In the case of a non-uniform microstructure, therefore, the impact energy can be raised just through increasing the fraction of refined regions which undergo ductile fracture. When assessing the weld metal toughness using the J_{IC} test, however, the toughness is determined at the first crack advance which occurs in the least tough region. This implies that fracture toughness of welded joint is determined by the toughness of the least tough microstructure in the weld deposit. This is why the uniformity of microstructure appears to be critical in improving the J_{IC} toughness value as much as the high

proportion of refined area. In most joints, however, it is difficult to avoid small portions of unrefined microstructure in localized regions unless post-weld heat treatments are applied. Nevertheless, at least the unrefined regions can be minimized by proper choice of welding techniques which avoid intensive local heating.

In order to prevent the weld beads from creating localized refinement, the geometry of each single bead has to be considered as a decisive influencing factor because the extent of refinement depends directly on the thickness of each bead. There are two types of weld beads, that is, stringer beads and weave beads. A stringer bead is made without appreciable oscillation resulting in a semi-circular shape of bead in cross-section as shown in Fig. 10. The weave bead is made with transverse oscillation which results in uniform thickness and the complete coverage on the underbeads as shown in the schematic diagram of Fig. 46. This difference in bead shape implies that the HAZ formed by a weave bead is more efficient in covering the underbead area without overlapping on other HAZs formed by previous beads than that formed by stringer beads. Therefore the weave technique has a distinct advantage over the stringer technique not only in increasing the proportion of the refined area but also in producing a uniform microstructure mainly through the less overlapping between HAZs. So the simple model of built-up layers of weave bead was made to assess the effect of welding conditions on the extent of refinement. A schematical drawing of this model is shown in Fig. 46, which was originally adopted by Ishimaru [97]. Considering the two successive layers of the i th bead and subsequent passes, the coarse grain structure formed inside the weld bead (columnar grains) and near the fusion line (coarsened grains) from the i th pass have to be exposed to the grain-refining regions of subsequent passes. Therefore, if the bottom line of grain-refined HAZ (b_{i+1}) of the $i+1$ th pass is lower than the bottom line of the grain-coarsened HAZ (A_i) of i th pass all the layers can be refined successively by the subsequent passes. This condition is expressed as the following:

$$\alpha = h_i + D_i + a_i = w_i g D_{i+1} + a_{i+1} + b_{i+1} = \beta \quad (7)$$

where h is the depth of the bead due to the adding of filler metal, D is the remelted depth of the previous bead, a is the depth of the grain-coarsened HAZ, and b is the depth of the grain-refined HAZ, α and β are summations of each term on both sides of equation IV-6 and are shown in Fig. 46. Suppose the heat input is the same and the successive change in joint geometry is negligible between adjacent passes, then the depth of each region (h , D , a , and b) is the same at the i th and $i+1$ th pass.

$$\begin{aligned} D_i &\approx D_{i+1} \\ a_i &\approx a_{i+1} \end{aligned} \quad (8)$$

and

$$b_i \approx b_{i+1}$$

combining equations 6 and 7, the following simple expression is derived:

$$h_i \leq b_i \quad (9)$$

This is the requirement to give at least a single grain refining thermal cycle on the coarse structure. If it is desired to refine the coarse structure at least twice, another thermal effect of the " $i + 2$ "th pass has to overlap the coarse grain region of the i th pass. With the same assumption as made above, the condition for this can be expressed as the following:

$$2h_i \leq b_i \quad (10)$$

This result indicates that the degree of refinement can be increased by decreasing the deposition rate (reduce h_i) and/or by increasing the depth of grain-refined HAZ (b_i). From an economical point of view, the decrease of deposition rate is not preferable since it increases the number of passes required for completion. The second approach to thicken the grain-refined HAZ (b_i), however, can be tackled by increasing the preheat temperature without sacrificing the deposition rate. The preheat treatment has a side effect of thickening the grain-coarsened HAZ (D_i). Fortunately this increase does not affect the results derived in equations (9) and (10) because the D_i term is not present in these equations. Thus, by increasing the preheat temperature, the degree

of grain refinement can be increased through an increase in the depth of the heat-affected zone. The effect of preheat temperature on the depth of the heat-affected zone is quite significant. For a single pass, full penetration butt weld in sheet material (two dimensional heat conduction) the distribution of peak temperatures in the base metal adjacent the weld is given by [98]:

$$\frac{1}{T_p - T_o} = \frac{4.13\rho C\alpha Y}{H_{net}} + \frac{1}{T_m - T_o} \quad (11)$$

where T_p = the peak temperature at a distance, Y , from the fusion boundary.

T_o = initial uniform temperature of the sheet plate

T_m = melting temperature H_{net} = net heat input = $\frac{\int I E I}{V}$

t = thickness of the plate

ρ, C = density and specific heat of the material

Using parameters such as:

$t^b = 730^\circ C, t = 5mm$, and $H_{net} = 0.72kJ/mm$, etc., the width of the heat-affected zone increases from 5.9 mm to 9.6mm with preheat temperature of $200^\circ C$. Although these values are derived for the so-called "thin-plate" condition, the 60 percent increase in the width of the heat-affected zone demonstrates the strong effect of preheat temperature in widening the heat-affected zone. An interesting variant of this approach is the use of interpass temperature as the preheat temperature, T_o , through the multi-arc process in which the interelectrode spacing is adjusted so that the following arc is delayed until solid state transformation has occurred and the arc sees a high interpass temperature set by the preceding electrodes. This has been recently exploited in GMA welding of LPG steels (3.5% Ni steel) to improve weld and heat-affected zone toughness [99]. Since this process still leaves the solidification structure at the final layer, which is not subjected to the additional thermal cycle, the toughness of weld metal decreases

as a whole as noted earlier in this section. For the purpose of improving the overall toughness of full thickness weld metal, the surface remelting process, which has been applied in welding of 9Ni steel with matching ferritic filler metal, should be followed on the final pass layer.

In summary, the weave bead technique combined with high interpass temperature and with surface remelting process is expected to be quite useful not only for the fully refined microstructure throughout the thickness but also for the increase in degree of grain refinement. Unfortunately, these techniques could not be attempted in the present study because of the poor control in manual welding process. Fully automatic GTAW equipment such as the TIL process [100] developed in Japan recently is necessary in order to verify the usefulness of the above techniques.

D. Alternative Welding Processes.

The GTAW welding process was selected for the present research because of its cleanliness and its controllability. In addition, the large, uniform heat-affected zone of the GTAW process is useful to insure the cyclic heat treatment of previously deposited material. This advantageous combination is not easily achieved in other welding processes such as gas metal arc (GMA) or electron beam (EB) welding. Conventional electron beam welding has already been demonstrated [17] to be inappropriate because of the coarse solidification structure established in the weld metal. The GMA process is also difficult to effect, but deserves further exploration because of the economic benefits to be achieved from its higher deposition rate. The gas metal arc welding (GMAW) process suffers from two shortcomings: the localization of its heat-affected zone due to its high deposition rate and its bell-like bead shape, and its relatively high contamination, particularly by oxygen and nitrogen, which arises from plasma jet instabilities in the consumable electrode process. Particularly, the characteristic shape (bell-like) of the GMA weld beads prevents the under beads from achieving uniform refinement. Zanis, et al. [101] considered the problem of achieving grain

refinement in a high-rate deposition GMAW process and have proposed reheat treatments using heating sources such as autogeneous GTAW or lasers to refine the GMA deposit. Dolby [102] has also proposed in-process techniques to refine the microstructure of weld deposits. But the contamination problem must also be overcome. Research and development of matching ferritic filler GMA welding methods were once performed [103] but no practical advancements have been achieved, since GMA arcs are stabilized only in the oxidizing-gas-mixed atmosphere. In a pure argon shielding atmosphere, a cleaning action of the cathode spot was generated on the surface and resulted in welding defects such as undercut. With the addition of oxygen and carbon dioxide to an inert gas, which can stabilize the arc, however, the oxygen content in the weld deposit was increased and resulted in poor toughness. Watanabe, et al. [104] investigated the notch toughness of shielded metal arc (SMA) weld metal and found that the toughness decreased dramatically when the oxygen content rose above 100 ppm. So the GMA welding process on 9Ni steel needed further development for stabilizing the arc under the pure argon shielding. Recently, Kawasaki Steel Company in Japan developed a pure argon shielding GMAW process by adding minute quantities of rare earth metals to the ferritic welding wire [105]. They reported [106] that this process was successfully applied to the welding of QT 9Ni steel by reducing the oxygen content below 50 ppm. However, this process still has a limited range of welding parameters which allow formation of a stable arc. Considering the importance of weld thermal cycles in refining the grain size, which is the primary factor in decreasing the DBTT, it is more desirable to control the heat input and deposition rate separately in order to obtain high toughness even at 4.2K. Further research will be necessary before the GMAW can be successfully used for welding ferritic steels with ferritic consumables for deep cryogenic applications.

CHAPTER V

SUMMARY and CONCLUSIONS

In order to develop the ferritic weldment for the liquid helium service, the grain-refined 9Ni and 12Ni plates were welded by multipass GTA welding process using 14% Ni filler materials. The results of mechanical tests showed that the welded joints has a matching strength and a comparable toughness with the base plates until down to 4.2K. The promising results obtained are attributed to the microstructural refinement through the multipass procedure as well as the chemical cleanliness of the weld deposit as achieved in the GTAW process. However, the details of microstructural changes during weld thermal cycles are quite different from those that occur in the furnace heat treatments so that the toughening mechanism of the welded region is also different, particularly in 9Ni steel. Further details of the conclusions drawn from this investigation are as follows:

1. From the microstructural study of bead-on-plate welds and full thickness weldments, the following observations were made:

- a. The microstructure of the 14Ni weld deposit consists of columnar grains and each columnar grain contains one or more bundles of cells growing in the same crystallographic orientation. The preferred growth orientation of cell structure was confirmed to be the $\langle 100 \rangle$ direction of austenite using a simple etching technique.

- b. An examination of partially overlapped bead-on-plate welds shows that the cell structure is hardly affected while the columnar grain structure is completely destroyed by the subsequent passes even along the fusion boundaries. This microstructural refinement is repeated layer by layer in the full-thickness weldments. However, a few isolated islands of partially refined structure remained.

- c. No measurable amount of retained austenite was detected in the weld deposit, as well as in the HAZ of the 12Ni joint. On the other hand, the volume fraction of

retained austenite existing in 9Ni steel, decreases monotonically through the HAZ as shown in the x-ray result.

2. Two filler metals with slightly different compositions were designed to study the effects of alloying elements on the weld metal properties. The following conclusions are derived on the basis of weld metal toughness and analytical results:

a. Ti is a better deoxidizer than Mn or Si since it not only acts as a scavenger of other deleterious elements such as carbon and sulfur but also it forms particles much smaller in size than Mn and Si.

b. The addition of boron improves the weld metal fluidity and produced a more easily controlled weld puddle resulting in better weld beads.

c. Combined inoculation with Ti and boron is not effective in refining the columnar grain size. This is because the nucleation event is not significant in the fusion welding process since a solid-liquid interface is always present and epitaxial growth occurs easily from unmelted base metal grains.

3. From the mechanical tests of ferritic weldments, the following results were obtained:

a. In tensile tests performed at 77K and room temperature, all the specimens fractured outside the weld metal and tensile properties of welded joints are very close to those of the base metal.

b. In Charpy impact tests, the ductile-brittle transition temperature of the weldment is below the liquid helium temperature (4.2K). The impact values of 9Ni steel is relatively flat across the HAZ so the HAZ toughness has no obvious correlation with the fraction of retained austenite remaining.

c. In the fracture toughness tests, the 2BT-treated 9Ni steel becomes brittle as the temperature goes down from 77 to 4.2K. The fracture toughness values K_{IC} (J) at 4.2K of 100, 82, and 132 ksi $\sqrt{\text{in}}$ (110, 90 and 145 MPa $\sqrt{\text{m}}$) were obtained in the 9Ni base

metal, its HAZ and weld metal respectively. The fracture surface of weld metal specimen shows a mixture in the fracture mode of dimple rupture and small amount of quasi-cleavage because of the non-uniform grain size in weld deposit. It represents that the weld metal toughness can be improved significantly by increasing the uniformity of grain size throughout the weld deposit.

4. Thermal cycling studies were performed to gain insight into the response of the base plates to the rapid heating and cooling cycles encountered in the HAZ during multipass welding.

a. *Austenitizing Cycle*. Rapid austenitizing, $\alpha \rightarrow \gamma \rightarrow \alpha$, thermal cycle is very effective in refining the grain size relative to conventional furnace treatment resulting in a significant suppression of DBTT even with a single cycle up to relatively high temperature region in austenite.

On the other hand, the austenitizing cycle causes the retained austenite, if present, to lose its stability and transform to martensite on cooling along with the surrounding matrix. Once the austenite transforms to martensite, it is not reformed by the subsequent tempering cycle. This causes a decrease in the amount of retained austenite across the HAZ of 9Ni steel.

The loss of retained austenite causes a significant drop in upper shelf toughness due to the supersaturation of carbon in the martensitic structure.

b. *The Tempering Cycle*. If the material does not contain carbon like 12Ni alloy or all the carbon in steel has been gettered into the precipitated austenite like the 9Ni base metal, the tempering cycle little affects the microstructure and toughness.

However, if the carbon is present as the supersaturated condition in the martensitic structure, the formation of cementite precipitates takes place during the tempering cycle. As a consequence of direct carbon gettering into the cementite precipitates, the upper shelf toughness improved to almost the same level as that obtained by the

introduction of austenite. So it is concluded that the cementite precipitate can act as a carbon scavenger just as the retained austenite does.

c. The above results illustrate the successive change in microstructure of the welded region during multipass welding procedure and also suggests different toughening mechanisms depending on the base plates. In 9Ni steel, while the precipitated austenite is removed by the high temperature austenitizing cycle near fusion boundary, the sequential rapid heat cycles to successively lower peak temperatures associated with succeeding weld passes reestablish high toughness by sequentially refining the microstructure and getting carbon into cementites. On the other hand, the high toughness in the HAZ of 12Ni alloy and in the carbon-free weld deposit is simply a consequence formed by the overlapped austenitizing cycles.

REFERENCES

- 1 H. I. McHenry and R. P. Reed; Nuclear Eng. Design, 58, 1980, 219.
- 2 Y. Takahasi, E. Tada, H. Tsuji and S. Shimamoto; ICEC9-ICMC, May, 1982, Kobe Japan.
- 3 R. L. Tobler, D. T. Reed and R. P. Reed; "Materials Studies for Magnetic Fusion energy Applications at Low Temperatures-IV", Tech. Rep. NBSIR 81-1645, pub. NBS, 1981, 37.
- 4 H. Yoshimura, T. Shimizu and K. Kitazima; Tetsu-to-Hagane, 67(11), 1981, 2019.
- 5 R. Mimura, K. Onishi, K. Yoshida and Y. Takahashi; *ibid*, 68(2), 1982, 490.
- 6 R. Ogawa and J. W. Morris, Jr.; ICEC9-ICMC, Kobe, Japan, May 1982.
- 7 S. Jin, J. W. Morris, Jr. and V. F. Zacky; Met. Trans. A, 6A(1), 1975, 141.
- 8 S. Jin, S. K. Hwang and J. W. Morris, Jr.; Met. Trans. A, 6A(8), 1975, 1569.
- 9 C. K. Syn, S. Jin and J. W. Morris, Jr.; *ibid*, 7A(12), 1976, 1827.
- 10 K. Ishikawa and K. Tsuya; Cryogenics, 17(5), 1977, 295.
- 11 M. Niikura and J. W. Morris, Jr.; Met. Trans. A, 11A(9), 1980, 1531
- 12 J. W. Morris, Jr., C. K. Syn, J. I. Kim and B. Fultz; Proc. Int. Con. Martensitic Transformation, Cambridge, 1979, 572.
- 13 T. Ooka and K. Sugino; J. Japan Ins. Metals, 30(5), 1966, 435.
- 14 J. I. Kim and J. W. Morris, Jr.; Met. Trans. A, 11A(8), 1980, 1401.
- 15 D. T. Reed and R. P. Reed; "Materials Studies for Magnetic Fusion Energy Applications at Low Temperatures-II", pub. NBS, 1979, 81.
- 16 R. L. Tobler and R. P. Reed; Symposium on Elastic-Plastic Fracture, ASTM, Atlanta, November, 1977.
- 17 D. E. Williams and J. W. Morris, Jr.; Weld. J., 61(5), 1982, 133-s.
- 18 K. Ishikawa and N. Marujama; Cryogenics, 18(10), 1978, 585.
- 19 M. Watanabe and I. Watanabe; IIW Doc. No. X-511-69, 1969.

- 20 C. E. Witherell and J. V. Peck; *Weld. J.*, 43(1), 1964, 3-s.
- 21 Nippon Kokan K. K. and Kobe Steel, LTD.; 1980 AWS 61st Annual Meeting, Session 22, 1980.
- 22 I. Watanabe; Central Research Lab., Nippon Kokan K. K., private communication.
- 23 J. H. Develetian, J. R. Stephens and W. R. Witzke; *Weld. J.*, 56(4), 1977, 97-s.
- 24 H. Tamura, T. Onzawa and S. Uematsu; *J. Japan Weld. Soc.*, 49, 1980, 855.
- 25 H. J. Kim; M. S. thesis, Univ. of Calif., Berkeley, 1981.
- 26 ASTM Standard Designation E-23.
- 27 R. L. Miller; *Trans. ASM*, 57, 1964, 892.
- 28 S. Jin, W. A. Horwood, J. W. Morris, Jr. and V. F. Zackay; *Adv. Cry. Eng.*, 19, 1974, 373.
- 29 ASTM Standard Designation E-399, 1975.
- 30 J. R. Rice, P. C. Paris and J. G. Merkle; ASTM STP 536, 1972, 231.
- 31 J. A. Begley and J. D. Landes; ASTM STP 514, 1972, 1.
- 32 F. A. Burdekin and D. E. W. Stone; *J. Strain. Anal.*, 1(2), 1966, 194.
- 33 F. J. Witt and T. R. Mager; *Nuclear Eng. Design*, 17, 1971, 91.
- 34 N. J. Petch; *Phil. Mag.*, 3, 1958, 1089.
- 35 G. A. Clark, W. R. Andrew, P. C. Paris and D. W. Schmit; ASTM STP 590, 1976, 27.
- 36 J. M. Merkle and H. T. Corten; *J. Pressure Vessel Tech. Trans. ASME*, 6, 1974, 1.
- 37 "LNG Materials and Fluids", pub. Cryogenic Div. of NBS, 1977.
- 38 H. Hayakawa and A. Imamura; *Bull. of JIM*, 18(4), 1979, 282.
- 39 L. E. Davis, N. C. MacDonald, P. E. Palmberg, G. E. Riach and R. E. Weber; "Handbook of Auger Electron Spectroscopy" 2nd ed., pub. Phys. Elec. Industries, Inc., Minn., 1972.

- 40 W. F. Savage, C. D. Lundin and A. H. Aronson; *Weld. J.*, 44, 1965, 175-s.
2nd ed., pub. Phys. Elec. Industries, Inc., Minn., 1972.
- 42 F. Matsuda, T. Hashimoto and T. Senda; *Trans. Nat. Res. Inst. Metal*, 11(1), 1969, 43.
- 43 W. F. Savage; *Welding in the World*, 18(5/6), 1980, 2.
- 44 W. F. Savage; "Weldments: Physical Metallurgy and Failure Phenomena", ed. R. J. Christoffel, 1978.
- 45 S. Matsuda, I. Inoue, H. Mimura and Y. Okamura; *Trans. ISIJ*, 12, 1972, 325.
- 46 T. Inoue, S. Matsuda, Y. Okamura and K. Aoki; *Trans. JIM*, 11, 1970, 36.
- 47 H. Ohtani, F. Terasaki and T. Kunitake; *Trans. ISIJ*, 12, 1972, 118.
- 48 U. H. Lindberg and B. L. Averbach; *Acta Met.*, 14, 1966, 1583.
- 49 D. Walton and B. Chalmers; *Trans. AIME*, 215(6), 1959, 447.
- 50 A. Rosenberg and W. A. Tiller; *Acta Met.*, 5(10), 1957, 447.
- 51 T. Maki and C. M. Wayman; *Acta Met.*, 25, 1977, 681.
- 52 M. J. Yokota, G. Sasaki and W. A. Horwood; *Mat. Sci. Eng.*, 19(1), 1975, 129.
- 53 K. W. Mahin and J. W. Morris, Jr.; *Adv. Cry. Eng.*, 26, 1980, 210.
- 54 S. K. Whang, S. Jin and J. W. Morris, Jr.; *Met. Trans. A*, 6A(11), 1975, 2015.
- 55 H. Tamura, T. Onzawa, S. Uematsu and K. Maekawa; *J. Japan Weld. Soc.* 48, 1979, 931.
- 56 T. Yamane, S. Takahashi, F. Inoko and G. Mimma; *Tech. Rep. of Osaka University*, 19, 1969, 409.
- 57 B. E. Kula and T. S. DeSisto; *ASTM STP 387*, 1965, 1.
- 58 J. M. Hodge, R. D. Manning and H. M. Reichold; *Trans. TMS-AIME*, 185(2), 1949, 233.
- 59 W. Jolley; *Trans. AIME*, 242(2), 1968, 306.
- 60 M. J. Yokoda, G. Sasaki and W. A. Horwood; *Mat. Sci. Eng.*, 19(1), 1975, 129.
- 61 S. Floreen, H. W. Hayden and T. W. Devine; *Met. Trans.*, 2(5), 1971, 1403.

- 62 D. J. Hurtuk and A. A. Tzavaras; *J. of Metals*, 34(2), 1982, 40.
- 63 "Practical Application of Welding Procedures of Ferritic Filler to 9% Ni Steel Plates for Cryogenic Storage Tanks", Kobe Steel, Ltd., No. RDPD-7902, 1972.
- 64 Z. Paley; *Weld. J.*, 48(6), 1969, 245-s.
- 65 K. W. Mahin, J. W. Morris, Jr. and I. Watanabe; *Adv. Cry. Eng.*, 26, 1980, 187.
- 66 D. J. Widgery; *Weld. J.*, 55(3), 1976, 57-s.
- 67 K. W. Mahin; Ph.D. thesis, University of California, Berkeley, 1980.
- 68 G. B. Hunter and T. W. Egar; Paper presented at Fall Meeting of TMS-AIME, 1979.
- 69 K. E. Dorshu; *Weld. J.*, 43(12), 1964, 564-s.
- 70 K. E. Dorschu; *Weld. Res. Council Bullitin*, No. 231, 1977.
- 71 H. Taga and A. Yoshikawa; *Trans. ISIJ*, 11, 1971, 1256.
- 72 S. K. Hwang and J. W. Morris, Jr.; *Met. Trans. A*, 11A(7), 1980, 1187.
- 73 J. H. Devletian and R. W. Heine; *Weld. J.*, 52(12), 1973, 529-s.
- 74 T. Funskoshi, T. Tanaka, S. Ueda, M. Ishikawa, N. Koshizuka and K. Kobayashi; *Trans. ISIJ*, 17, 1977, 419.
- 75 C. R. Simcoe, A. R. Elsea and G. K. Manning; *Trans. AIME*, 203, 1955, 193.
- 76 J. A. Grange and J. B. Mitchell; *Trans. ASM*, 53, 1961, 157.
- 77 R. A. Grange and T. M. Garvey; *Trans. ASM*, 37, 1946, 136.
- 78 R. A. Grange; *Met. Trans.*, 2(1), 1971, 65.
- 79 B. Karlsson; *Mat. Sci. Eng.*, 11, 1973, 185.
- 80 S. W. Mahajan, G. Venkataraman and A. K. Mallik; *Metallography*, 6(4), 1973, 337.
- 81 L. F. Porter and D. S. Dabkowski; "Ultrafine Grain Metals", pub. Syracuse Univ. Press, Syracuse, N.Y., 1969.
- 82 G. Sasaki and M. J. Yokoda; *Met. Trans. A*, 6A(3), 1975, 586.
- 83 J. I. Kim and J. W. Morris, Jr.; *Met. Trans. A*, 12A(11), 1981, 1957.

- 84 J. I. Kim and J. W. Morris, Jr.; Met. Trans. A, 11A(8), 1980, 1401.
- 85 T. Ooka and K. Sugino; J. JIM, 30(5), 1966, 435.
- 86 T. Ooka, H. Mimura, S. Yano, K. Sugino and T. Yoizumi; J. JIM, 30(5), 1966, 442.
- 87 J. R. Strife and D. E. Passoja; Met. Trans. A, 11A(8), 1980, 1341.
- 88 J. W. Morris, Jr.; LBL No. 11628, Lawrence Berkeley Laboratory, University of California, Berkeley, California, 1980.
- 89 R. N. Caron and G. Krauss; Met. Trans., 3(9), 1972, 2381.
- 90 Abron; T. ASM, 48(1), 1956, 51.
- 91 F. B. Pickering; "Toward Improved Ductility and Toughness", pub. ISIJ and JIM, 1971, 9.
- 92 D. Brooksbanks and K. W. Andrews; JISI, 185, 1964, 889.
- 93 A. W. Pense and R. D. Stout; WRC Bulletin, No. 205, 1975.
- 94 "Micro-Alloying 75", Washington, D. C., Oct. 1975, Union Carbide Corp., N.T.
- 95 M. Tokizane and N. Matsumura; Trans. ISIJ, 22(2), 1982, 27.
- 96 J. I. Kim; Ph.D thesis, Univ. of Calif., Berkeley, 1979.
- 97 Y. Ishimaru, H. Kobayashi, T. Okada and F. Tomiyasu; Weld. J., 57 (8), 1978, 273-s.
- 98 "Welding Handbook", Vol. 1, 7th ed., 1980.
- 99 H. Onoe, J. Tanaka and I. Watanabe; Met. Const., 11(1), 1979, 26.
- 100 Y. Ogata, I. Aida, M. Nagashima and K. Shibuya; Weld. J., 61(8), 1982, 355-s.
- 101 C. A. Zanis, P. W. Holsberg and E. C. Dunn, Jr.; ibid, 59(12), 1980, 355-s.
- 102 R. E. Dolby; ibid, 58(8), 1979, 225-s.
- 103 9Ni Committee, Japan Weld Engineering Society; "Testing and Research concerning Practical Application of Matching Ferritic Fillers to 9% Ni Steel", Nov. 1975.
- 104 M. Watanabe, J. Tanaka and I. Watanabe; Weld. and Met. Feb., 41(5), 1973,

167.

105 K. Agusa, N. Nishiyama and J. Tsuboi; *Met. Const.*, 13(9), 1981, 570.

106 K. Agusa, M. Kosho, N. Nishiyama, A. Kamata and Y. Nakano; *Kawasaki Steel Co. Tech. Rep.*, No. 6, Japan, Sept. 1982.

TABLES AND FIGURES

TABLE I				
Tensile Properties and Fracture Toughness of Various Steels at 4.2K				
Steel	Yield Stress Ksi (MPa)	Tensile Stress Ksi (MPa)	K_{IC} Ksi $\sqrt{\text{in}}$ (MPa $\sqrt{\text{m}}$)	Ref. #
Fe:12Ni-0.25Ti	195(1345)	219(1510)	232(255)*	8
9%Ni steel	191(1316)	223(1537)	166(183)*	9
1304LN	112(771)	245(1686)	191(210)**	15
316LN	149(1025)	201(1388)	185(203)**	15
Nitrnic 40	187(1241)	237(1634)	166(182)**	16

* Rough estimation of K_{IC} using 'Equivalent Energy Method'. ** Derived by initiation J_{IC} test, $K_{IC}(J)$.

Table II. Compositions of base metals, filler metals and weld deposits.

Element		Fe	Ni	Ti	Mn	Si	P	S	O	N	B	C
Base Metal	9 Ni	bal.	8.49	—	0.45	0.24	0.006	0.002	0.002	0.004	—	0.059
	12 Ni	bal.	12.07	0.20	—	—	0.001	0.002	<0.001	<0.001	—	0.002
Filler Metal	A	bal.	14.04	0.21	0.37	0.09	0.005	0.002	0.005	<0.001	—	0.006
	B	bal.	13.87	0.16	—	—	0.001	0.002	0.006	<0.001	0.003	0.003
Weld Deposit in 12 Ni	A	bal.	13.98	0.20	0.33	0.08	0.005	*	0.007	0.007	—	0.003
	B	bal.	13.81	0.15	—	—	*	*	0.007	0.006	0.0027	0.003

* Not Analyzed

— Negligible

XBL 827-6078

TABLE III. Welding Conditions

	Condition 1	Condition 2
Heat Input (kJ/mm)	0.7	1.7
Arc Voltage (V)	14-18	18-20
Welding Current (A)	150-180	250-300
Welding Speed (mm/sec)	4	4
Shielding Gas	Pure Argon, 25 ft ³ /hr. (0.7 m ³ /hr)	
Root Gap	Same as rod diameter	
Interpass Temperature	Less than 50 C.	
Welding Position	Flat	Flat

TABLE IV					
Results of Tensile Tests at 77K					
Specimen	Heat Input	Yield	Tensile	Elong.	R. A.
	kJ/mm	Stress	Stress		
		ksi(MPa)	ksi (MPa)	(%)	(%)
Fe-12Ni-0.25Ti		149(1028)	154(1062)	26.8	72
9% Ni Steel		146(1007)	163(1125)	34.0	71
Welded Joint*	0.7	145(1001)	154(1063)	25.0	71
(12Ni/HAZ/WM)					
	1.7	140(966)	148(1021)	21.2	68

* All specimens were fractured near Base/HAZ boundary.

TABLE V			
Charpy Impact Toughness with Different Joint Configurations			
Weld Metal	Testing Temp. (K)	Single Bevel	Single V
		Joule (ft-lb)	Joule (ft-lb)
Filler A	77.0	95(70)	167(123)
	4.2	37(27)	72(53)
Filler B	77.0	166(122)	183(135)
	4.2	132(97)	174(128)

TABLE VI			
Charpy V-notch Impact Values of 9Ni and 12Ni Welded Joint			
	Impact Energy, Joule (ft-lb)		
	Weld Metal	HAZ	Base Metal
9Ni joint at 77K	184 (136)	169 (125)	156 (115)
at 4.2K	153 (113)	149 (110)	146 (108)
12Ni joint at 77K	182 (135)	217 (160)	156 (115)
at 4.2K	173 (128)	179 (132)	136 (100)

TABLE VII						
Fracture Toughness, K_{IC} (E) of 12Ni Weldment						
Test Temp.	Heat Input kJ/mm	Three-Point Bend			Compact Tension	
		ksi/ \bar{m} (MPa/ \bar{m})			ksi/ \bar{m} (MPa/ \bar{m})	
		W.M.	HAZ	Base	W.M.	Base*
77	0.7	324(356)	-	300(330)	-	307(338)
	1.7	286(315)	330(363)	300(330)	280(308)	307(338)
4.2	1.7				160(176)	232(255)*

* Reported in reference [8].

TABLE VIII. Results of J-integral tests of 9Ni weldment.

	Three Point Bend		Modified Compact Tension	
	K_{Jm}^* ksi/ \sqrt{m} (MPa/ \sqrt{m})		K_{Ic} (J) ksi/ \sqrt{m} (MPa/ \sqrt{m})	
Testing Temperature	77 K		77 K	4.2 K
9Ni Base Metal	246(271)		294(323)	100(110)
Heat-affected zone	235(259)		265(292)	82(90)
Weld Metal	262(288)		332(365)	132(145)

* Invalid values obtained from J corresponding to maximum load (J_{max})

FIGURE CAPTIONS

- (1) The Fe-Ni equilibrium phase diagram with base metal heat treatments of (a) Fe-12Ni-0.25Ti alloy and (b) 9%Ni steel.
- (2) Weld joint groove designs: (a) Single-V groove, (b) Single-bevel groove, (c) Double-V groove.
- (3) Thermal cycle curve for the simulation of 1300(deC peak temperature.
- (4) Subsize cylindrical tensile test specimen (1 in = 25.4 mm).
- (5) Standard Charpy impact test specimen (1 in = 25.4 mm).
- (6) Styrofoam box configurations for the 4.2K Charpy impact test.
- (7) Cooling curves for the Charpy specimens under the liquid nitrogen or liquid helium flow.
- (8) Specifications of various fracture toughness specimens, (1 in = 25.4 mm): (a) three-point bend specimen, (b) compact tension specimen, and (c) modified compact tension specimen for J_{IC} test.
- (9) Optical micrographs of bead-on-plate weld etched with (a) 5% Nital and (b) the same region etched with acidified $FeCl_3$ solution ($\mu = \mu m$).
- (10) Optical micrographs of (a) partially overlapped bead-on-plate welds with heat input of 0.7 KJ/mm and (b) single bead with 1.87 KJ/mm.
- (11) Intergranular fracture appearance of bead-on-plate weld fractured at 77K: (a) Macroscopic view, (b) schematic drawing of sample preparation, (c) SEM fractographs taken before etching and (d) after etching with 5% Nital solution ($\mu = \mu m$).
- (12) Cellular structure revealed on the intergranular fracture surfaces ($\mu = \mu m$).
- (13) Cellular patterns revealed on the cleavage facets ($\mu = \mu m$).

- (14) Etch pits developed on the {100} cleavage facet and their analysis.
- (15) Microstructural changes of annealed 12Ni specimens with peak temperatures ($\mu = \mu m$).
- (16) Variation of Charpy impact energy with peak temperatures of weld thermal cycles.
- (17) Microstructural changes of 12Ni base metal with various peak temperatures ($\mu = \mu m$).
- (18) Charpy impact energy at 77K vs. peak temperature in 12Ni base metal.
- (19) Variations of Charpy impact energy at 77K, amount of retained austenite and hardness with various peak temperatures cycled on the 9Ni base metal (1 ft-lb = 1.355 Joule).
- (20) TEM micrographs of 2BT-treated 9Ni base metal: (a) bright field image, (b) dark field image of retained austenite and (c) selected area diffraction pattern.
- (21) TEM micrograph of 9Ni specimen cycled up to 750C ($\mu = \mu m$).
- (22) Multicycle HAZ simulations on the 2BT-treated 9Ni steel (1 ft-lb = 1.355 Joule).
- (23) Optical micrographs of HAZ-simulated 9Ni specimens ($\mu = \mu m$).
- (24) SEM fractographs of HAZ-simulated 9Ni specimens broken at 77K ($\mu = \mu m$).
- (25) TEM micrographs of double (1200 + 800(deC) cycled specimen: (a) bright field image, (b) SAD pattern taken from region B, (c) SAD pattern from region C, (d) and (e) are dark field images illuminated by (10 $\bar{1}$) and (200) spots respectively.
- (26) TEM micrographs of triple (1200 + 800 + 600(deC) cycled specimen: (a) bright field image, (b) dark field image of cementite precipitates and (c) SAD pattern and its schematic drawing.

- (27) Macro- and microstructures of full-thickness single-V 12Ni joint (1 cm = 10mm, $1\mu = 1\mu m$).
- (28) Macro- and microstructures of single-bevel 9Ni joint ($\mu = \mu m$).
- (29) Variation of austenite content across the HAZ of 9Ni steel.
- (30) Variation of impact toughness with notch location in 12Ni joint.
- (31) Impact toughness of filler B weld deposit with testing temperature, heat input and notch orientation (1 ft-lb = 1.355 Joule).
- (32) SEM fractographs of filler A weld deposit at (a) the ductile and (b) brittle region with EDAX analysis of particles in each region ($\mu = \mu m$).
- (33) Scanning Auger microprobe spectrum of matrix and Ti particles inside the fracture dimples ($DN/DE = dN/dE$).
- (34) Comparison of 4.2K impact toughness between 9 and 12Ni weldments.
- (35) SEM fractographs of 9Ni specimens broken at 4.2K: (a) weld metal, (b) HAZ and (c) base metal.
- (36) Load-COD curves of 12Ni three-point bend specimens tested at 77K.
- (37) Load-COD curves of weld metal specimens in the compact tension tests at 77 and 4.2K.
- (38) SEM fractographs of weld metal specimens recorded in Fig. 37 ($\mu = \mu m$).
- (39) Load-Load point displacement curves of 9Ni joint in the three-point bend tests at 77K (1 lb = 0.45 kg, 1 in = 25.4 mm).
- (40) Load-Load line displacement curves of 9Ni joint in the J_{IC} tests at 77 (1 lb = 0.45Kg, 1 in = 25.4 mm).
- (41) Post-test fracture toughness specimens tested at 77K (1 cm = 10 mm).
- (42) Load-Load line displacement curves of 9Ni base and weld metal specimens tested at 4.2K (1 lb = 0.45Kg, 1 in. = 25.4 mm).

- (43) SEM fractographs of fracture toughness specimens recorded in Fig. 42 ($\mu = \mu m$).
- (44) Optical micrographs of 9Ni steel: (a) rapid cycled up to 800(deC and (b) austenitized for one hour at 750(deC ($\mu = \mu m$).
- (45) Variation of Charpy impact energy and austenite content with tempering time at 590C (1 ft-lb = 1.355 Joule).
- (46) Schematic drawings of build-up layers.

Fe - Ni PHASE DIAGRAM

HEAT TREATING CYCLES

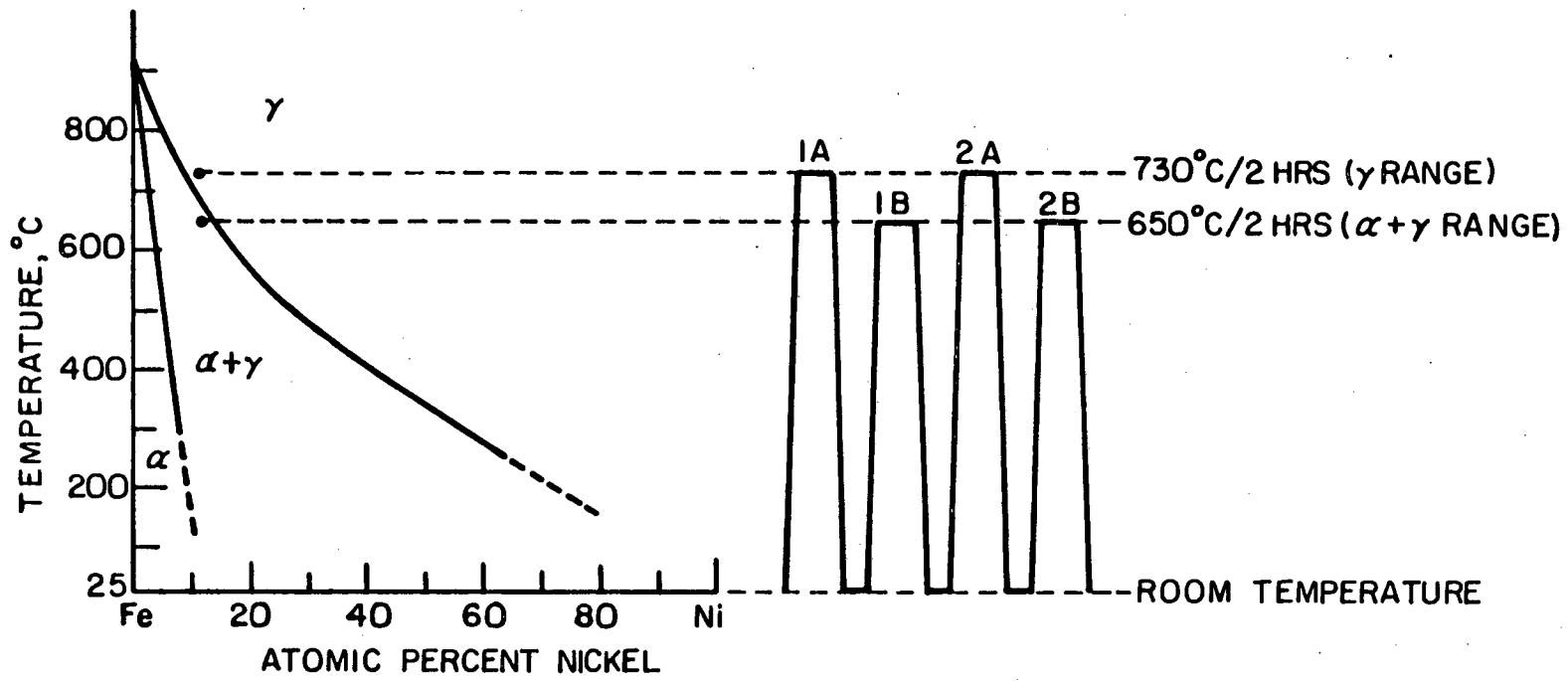
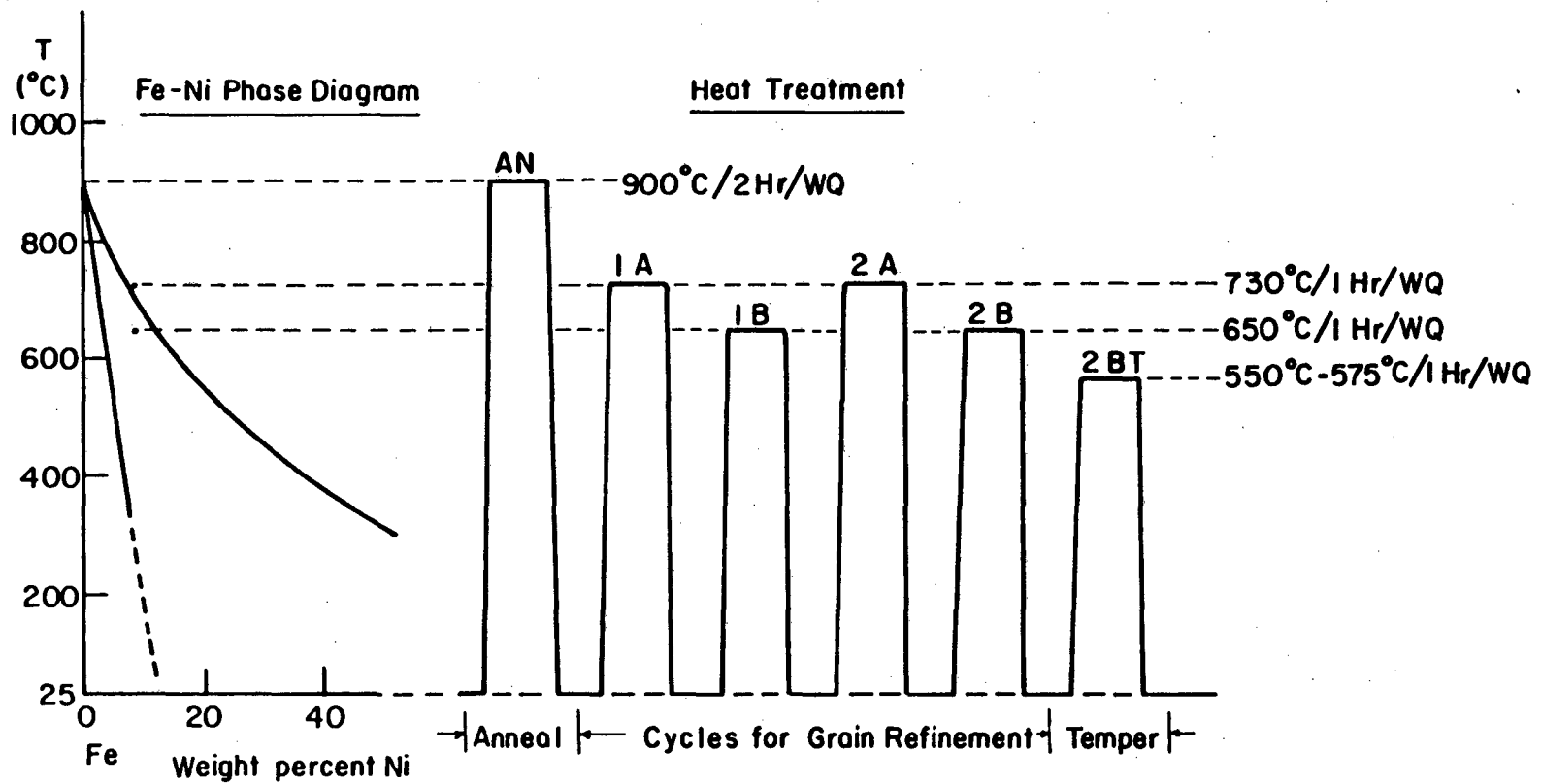


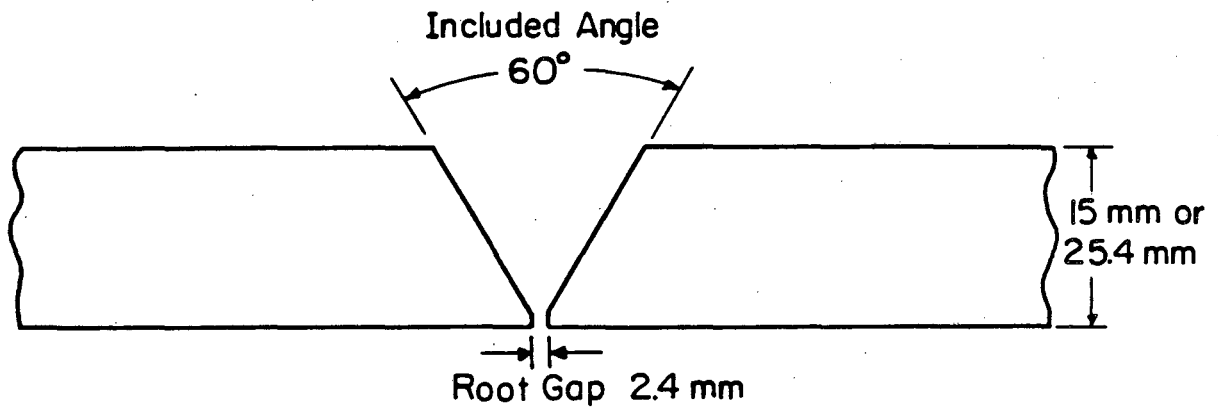
Fig. 1-a

XBL 739-1884

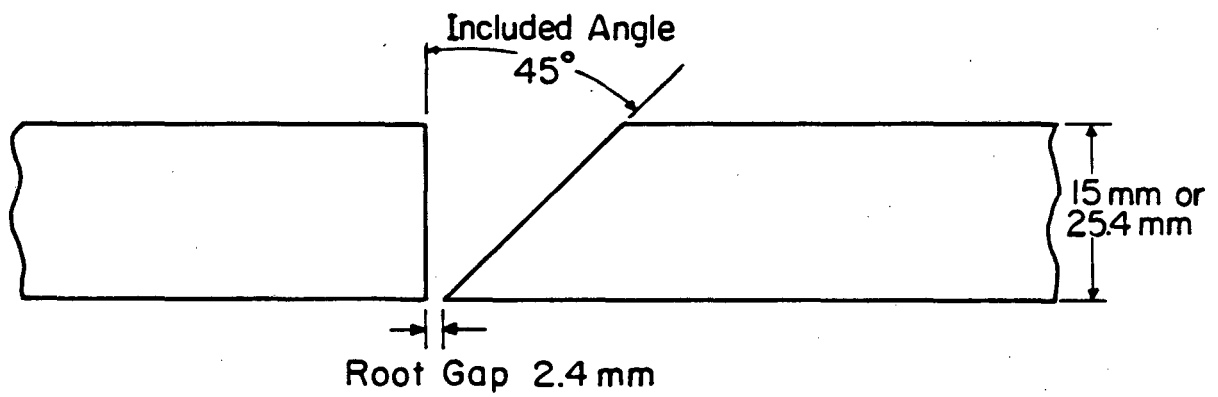


XBL 762-6382

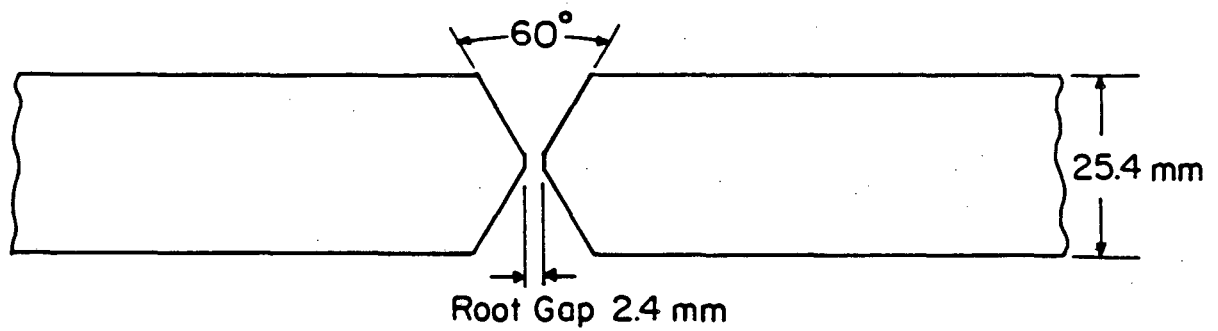
Fig. 1-b



a. Single-V Groove



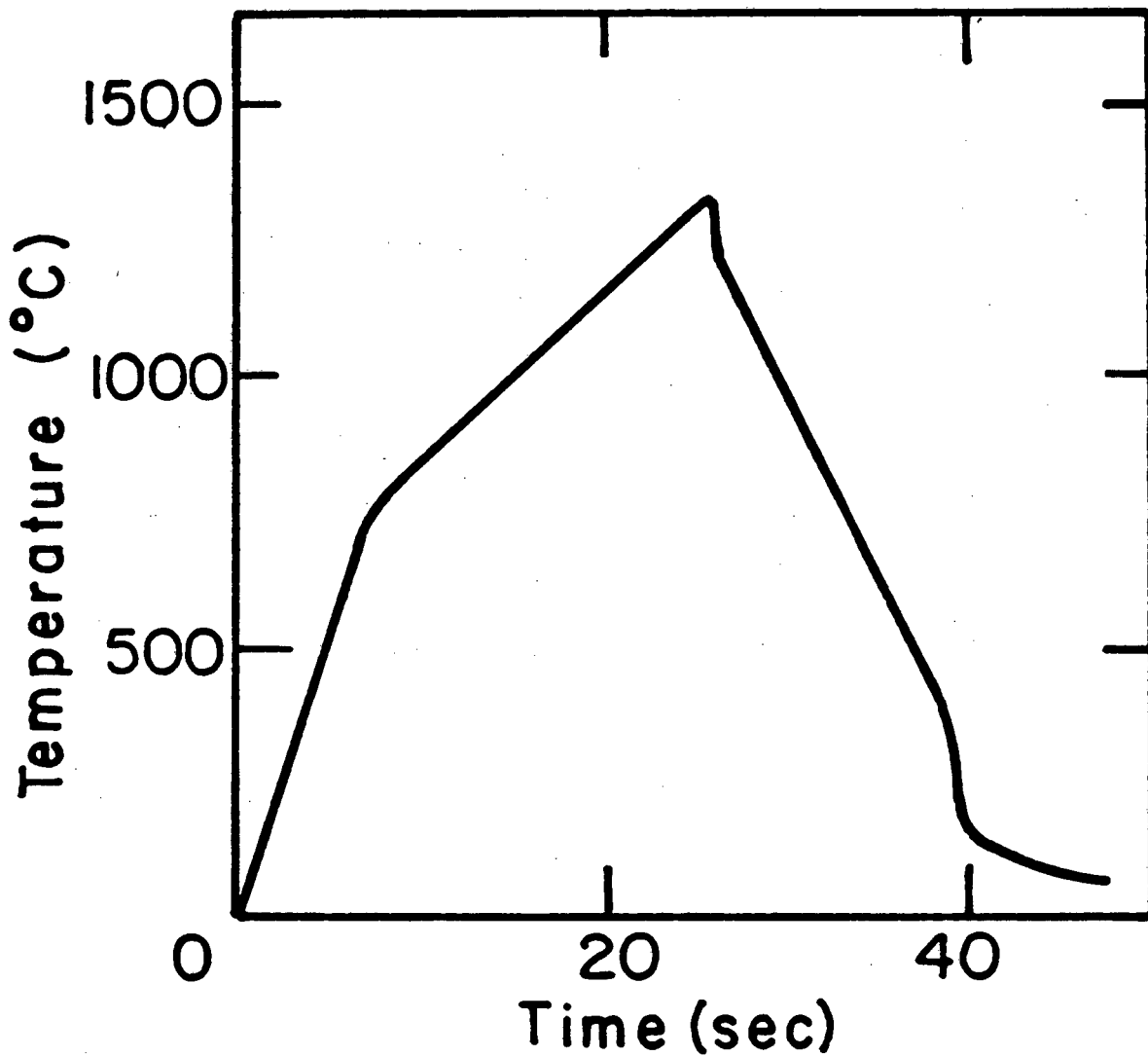
b. Single-Bevel Groove



c. Double-V Groove

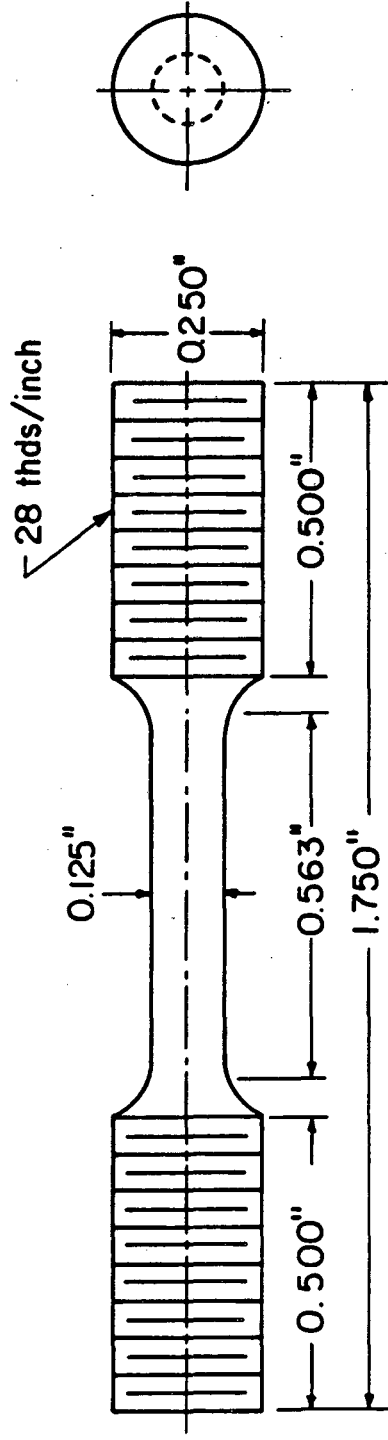
XBL829-6529

Fig. 2



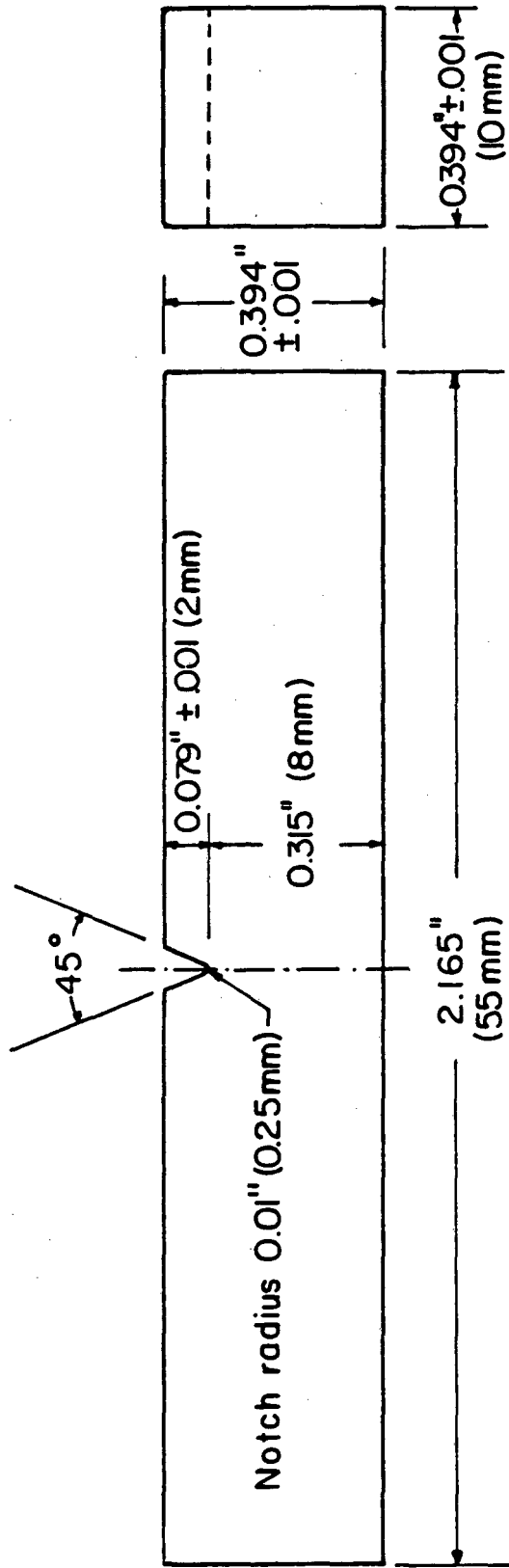
XBL 803-4799

Fig. 3



XBL 774- 5354

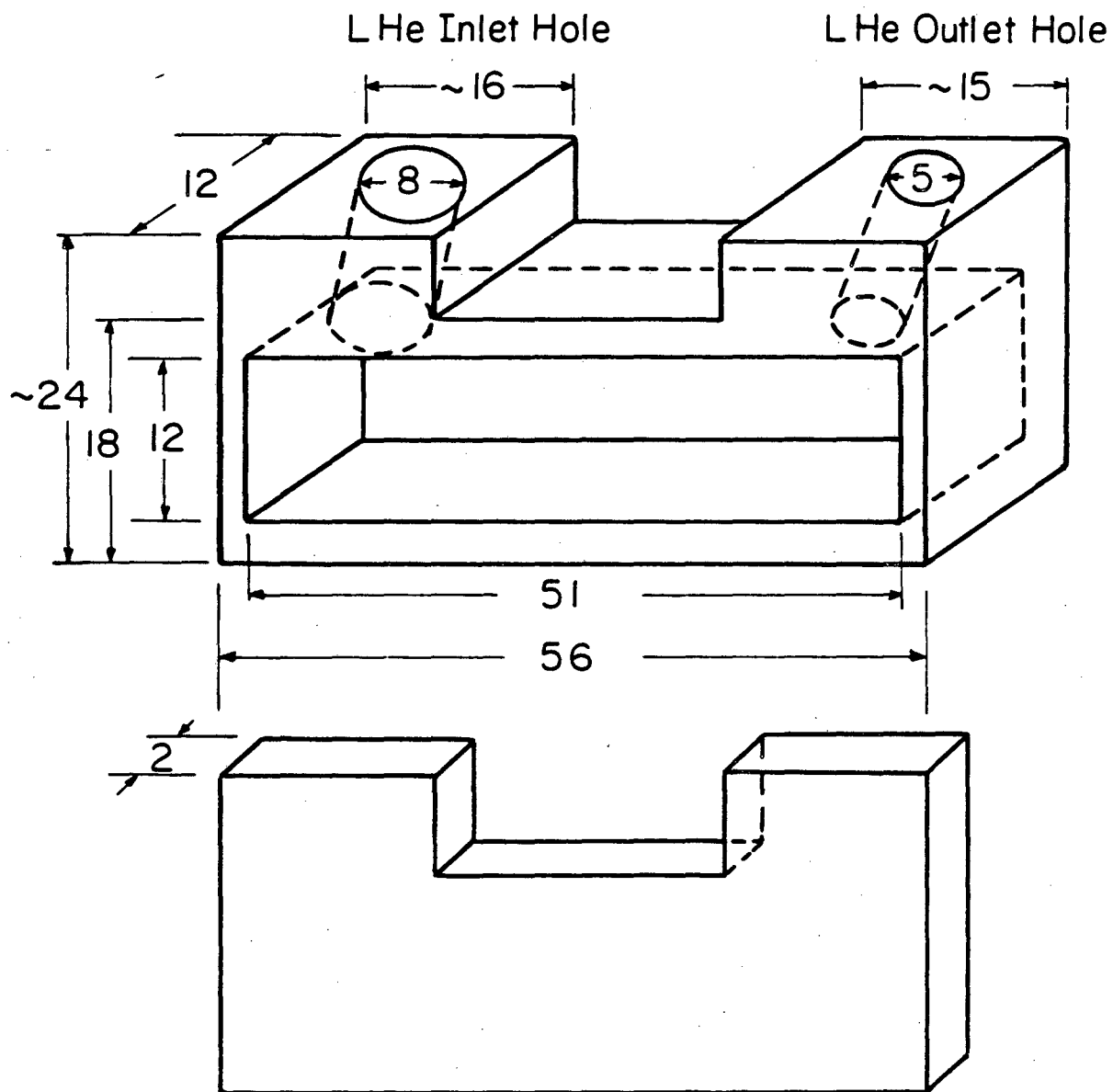
Fig. 4



Grind finish

XBL 7910-7195

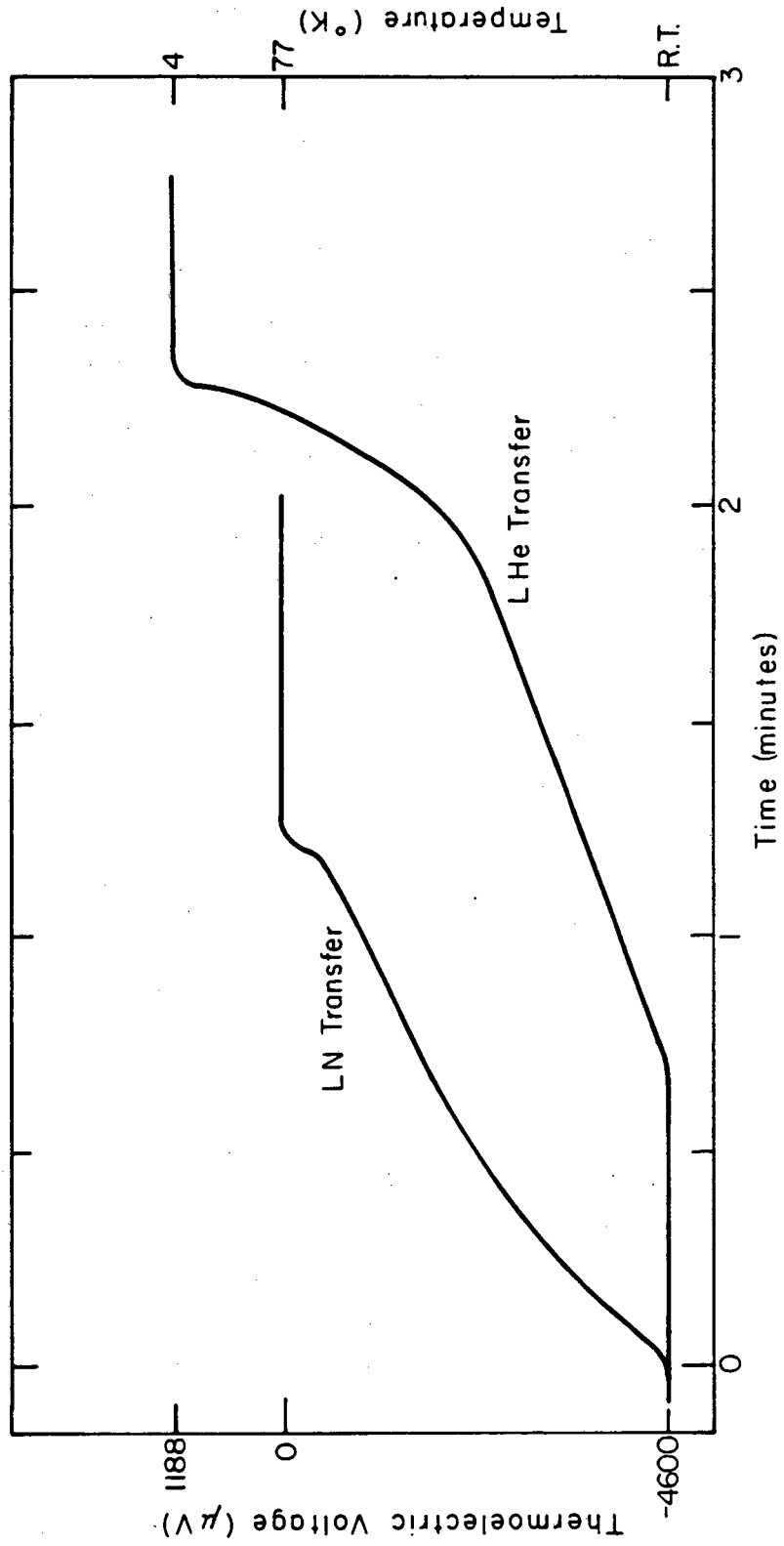
Fig. 5



Units in mm

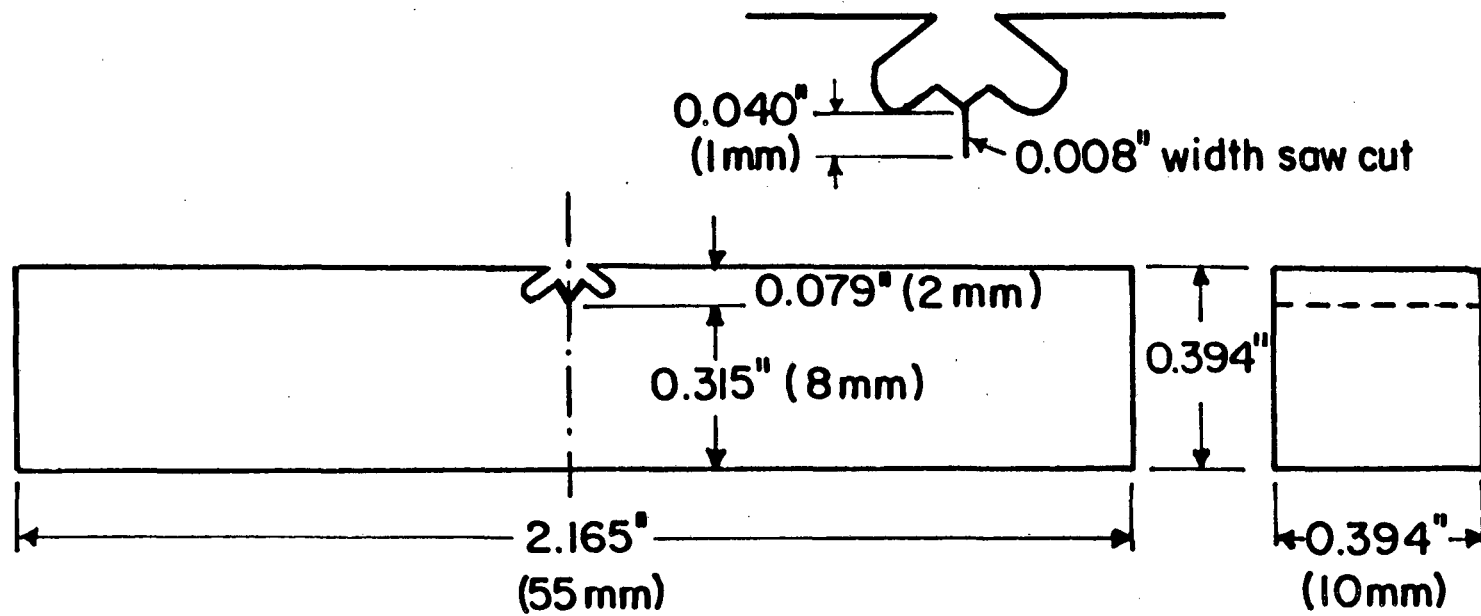
XBL 808-5606

Fig. 6



XBL 808-5607

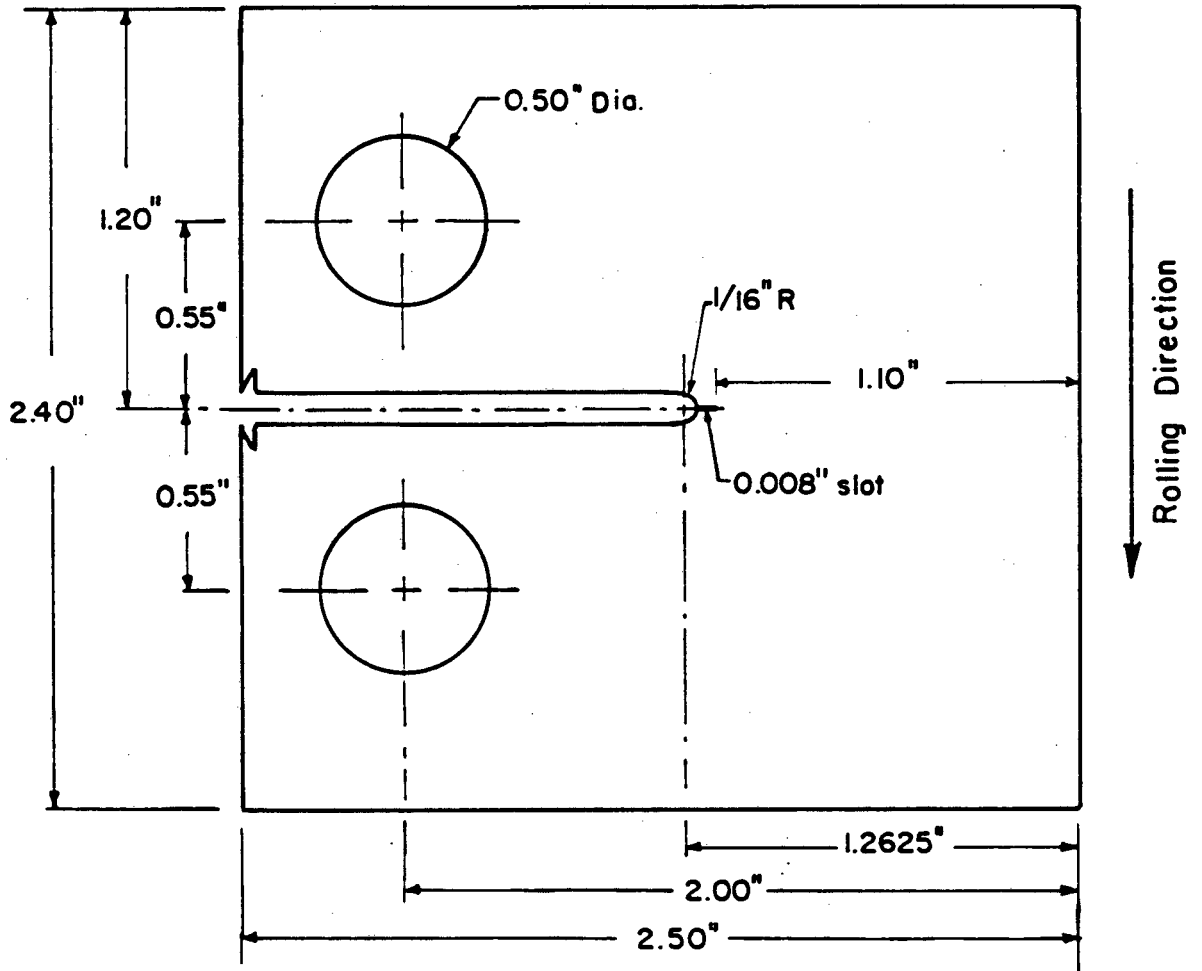
Fig. 7



(a)

Fig. 8-a

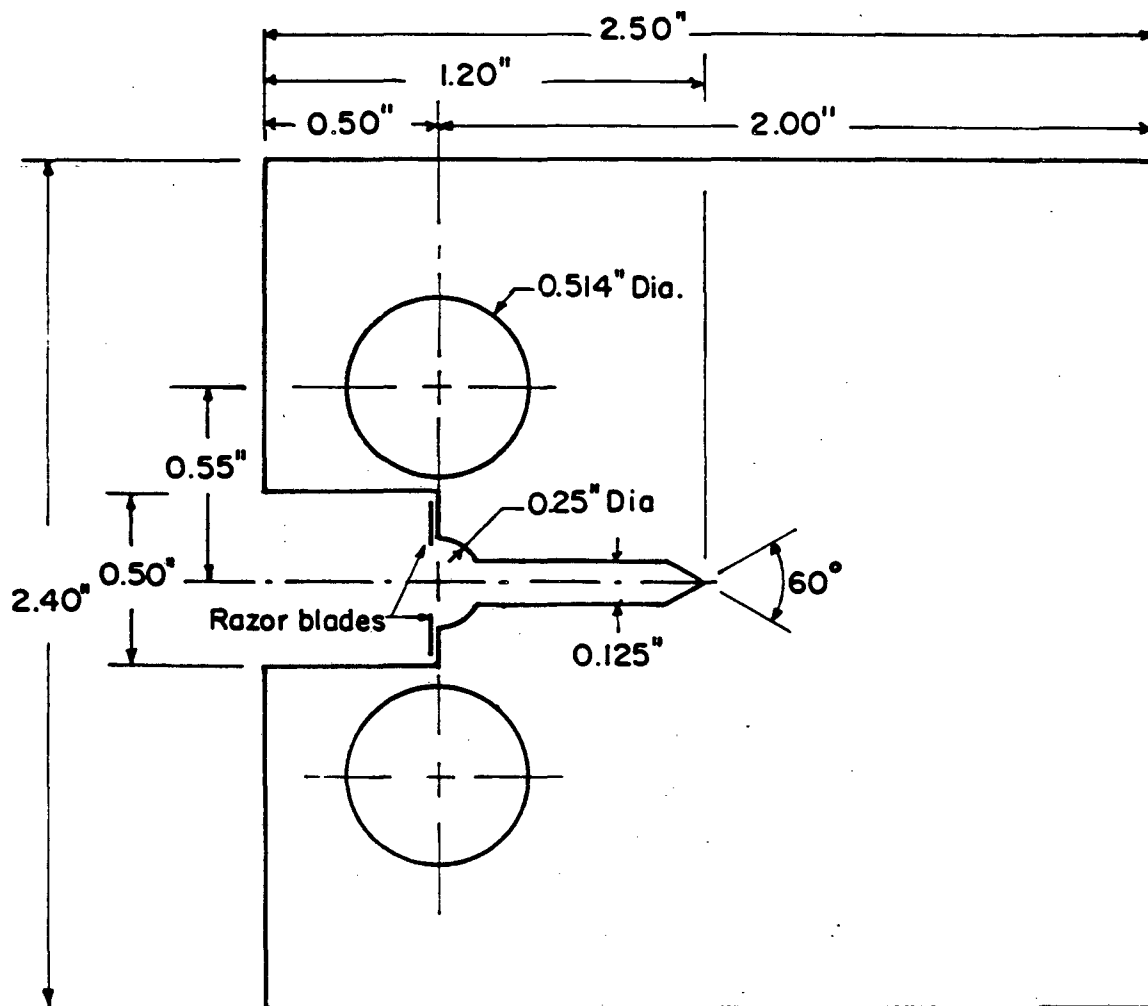
XBL 827-6028



(b)

Fig. 8-b

XBL 827-6029



(c)

XBL 827-6030

Fig. 8-c



5% Nital

Fig. 9

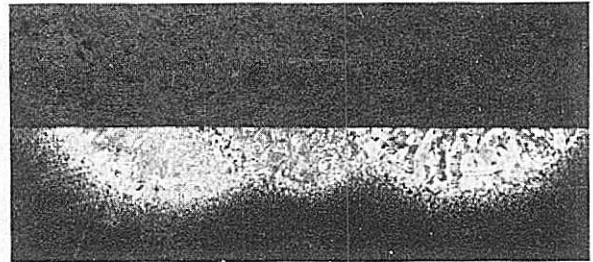


Acid. FeCl₃

XBB 802-1882

Heat Input

6.4 (KJ/cm)



18.7 (KJ/cm)

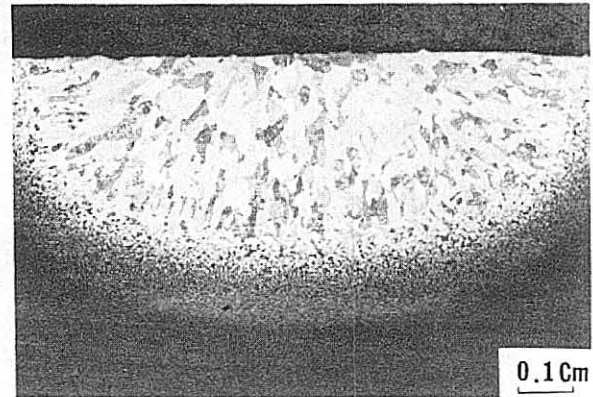


Fig. 10

XBB 805-6225

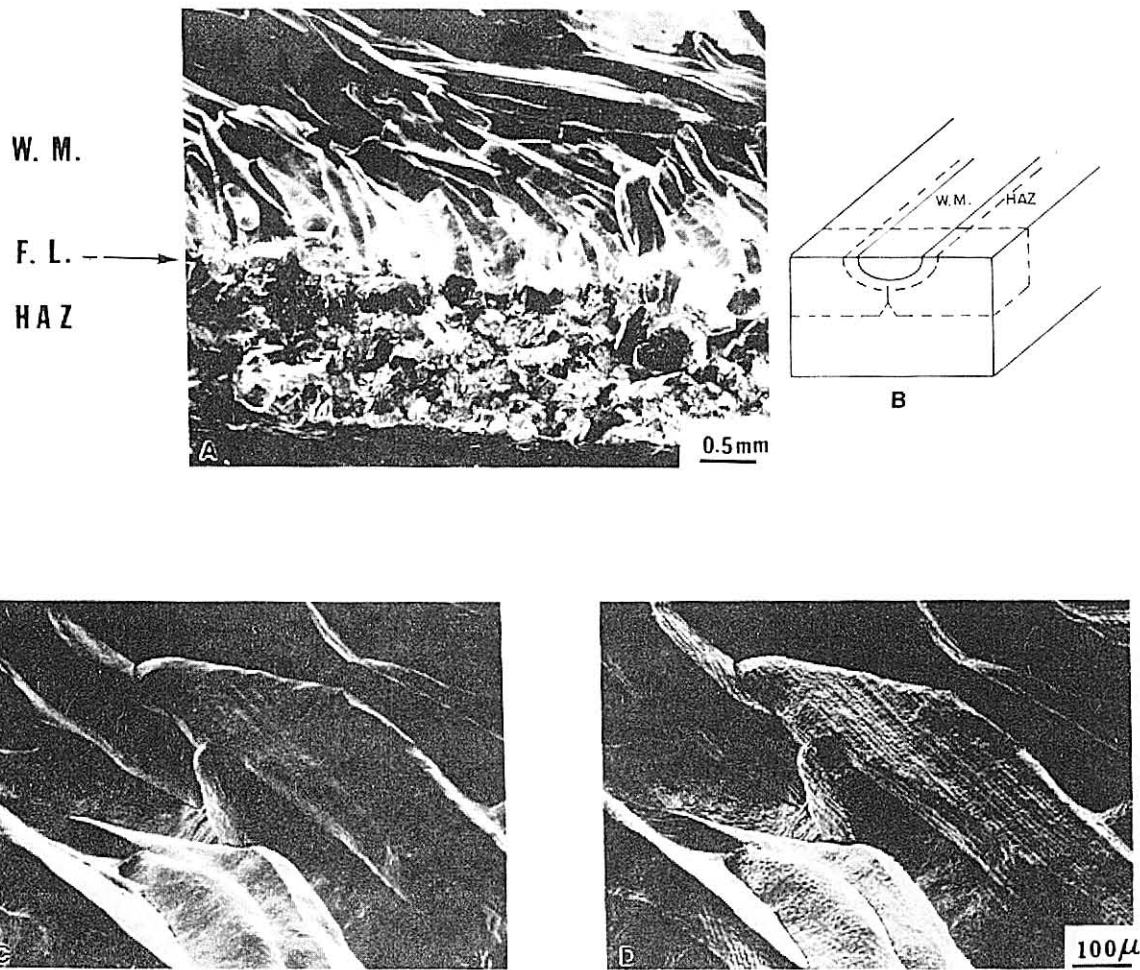


Fig. 11

XBB 812-1733

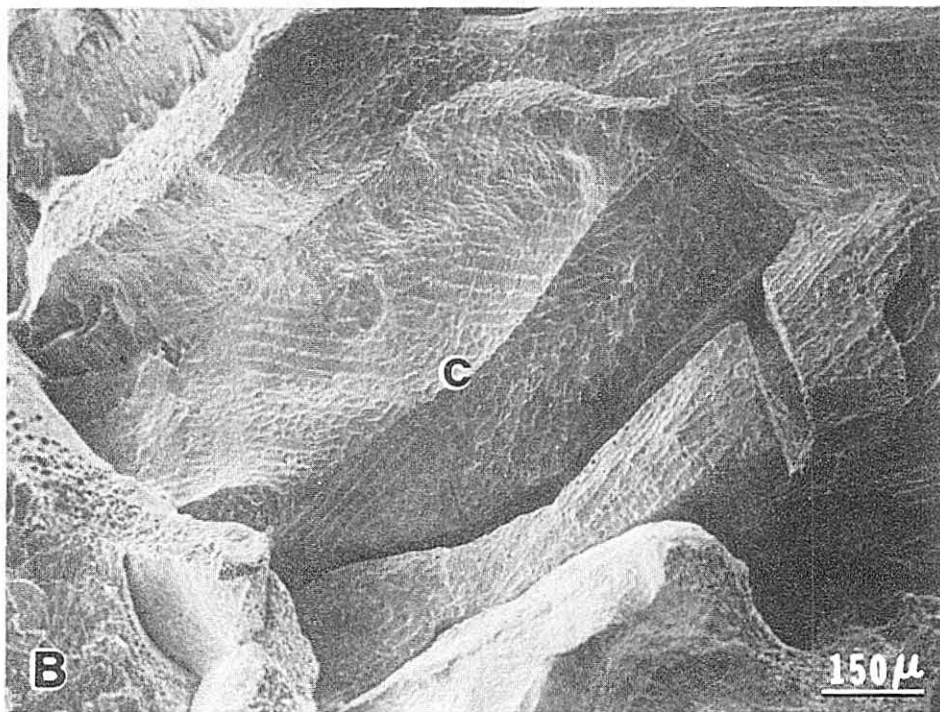


Fig. 12

XBB 823-1736

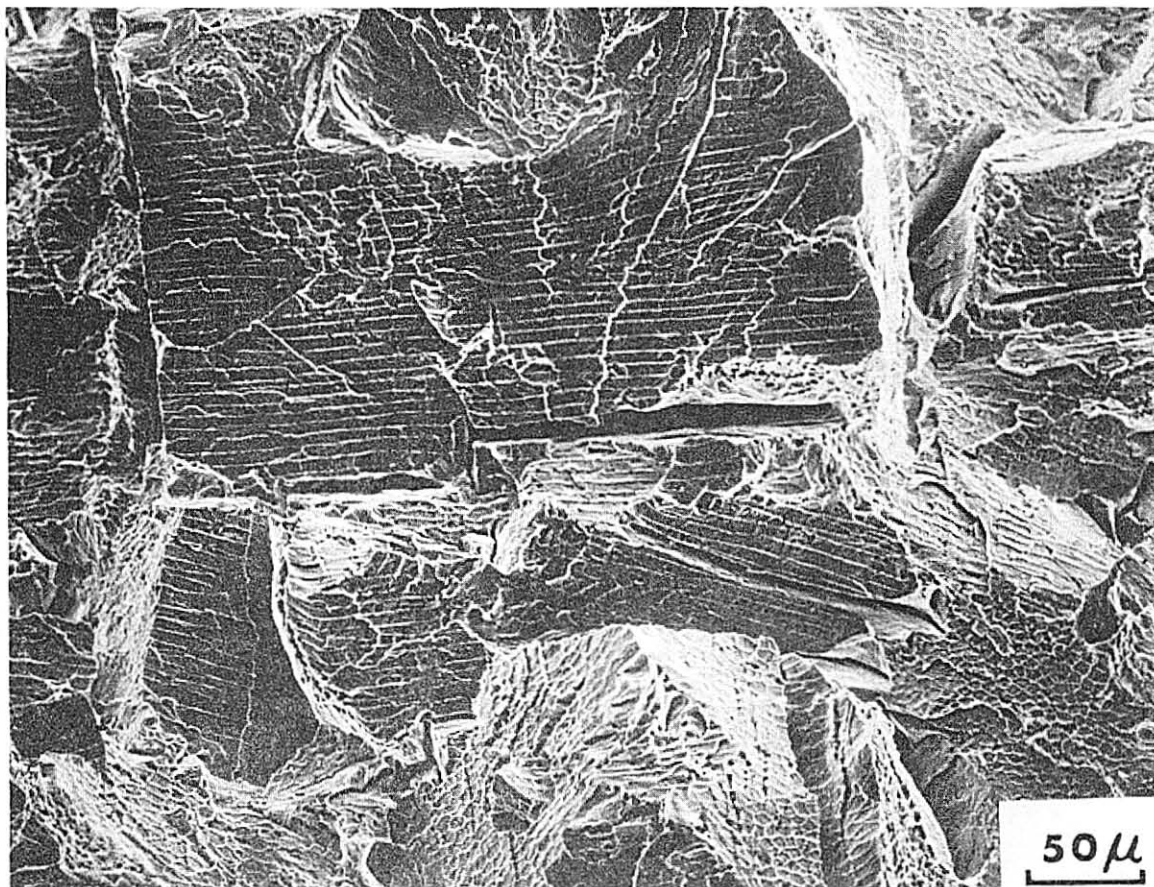


Fig. 13

XBB 805-5476

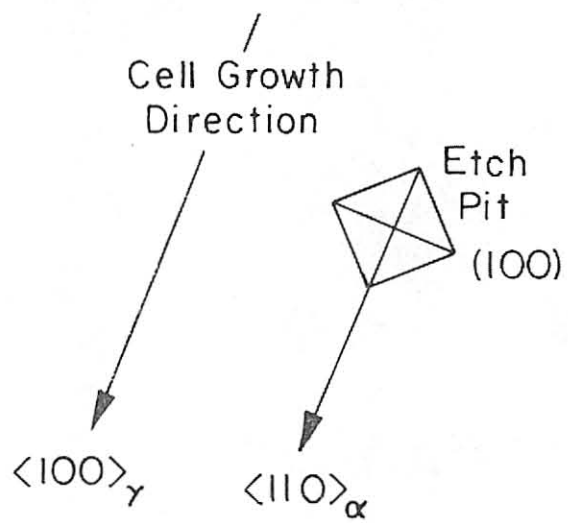
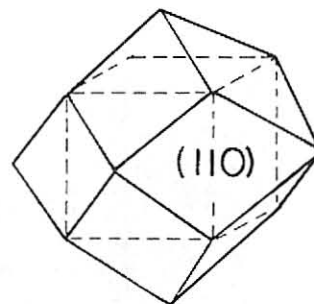
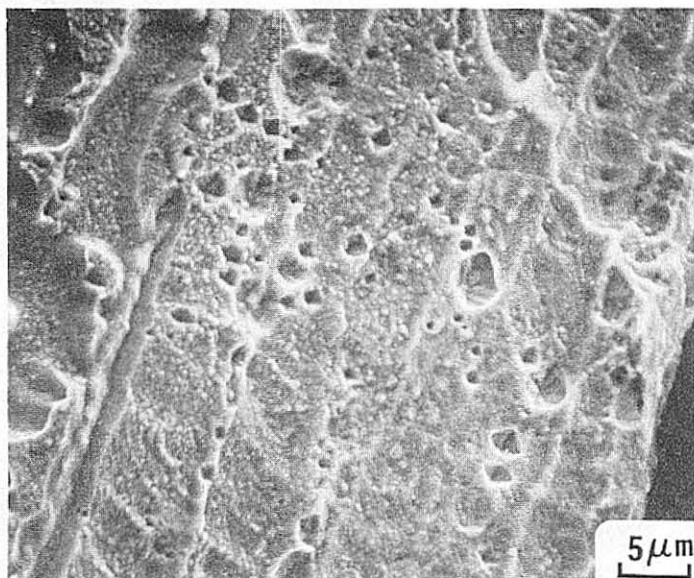
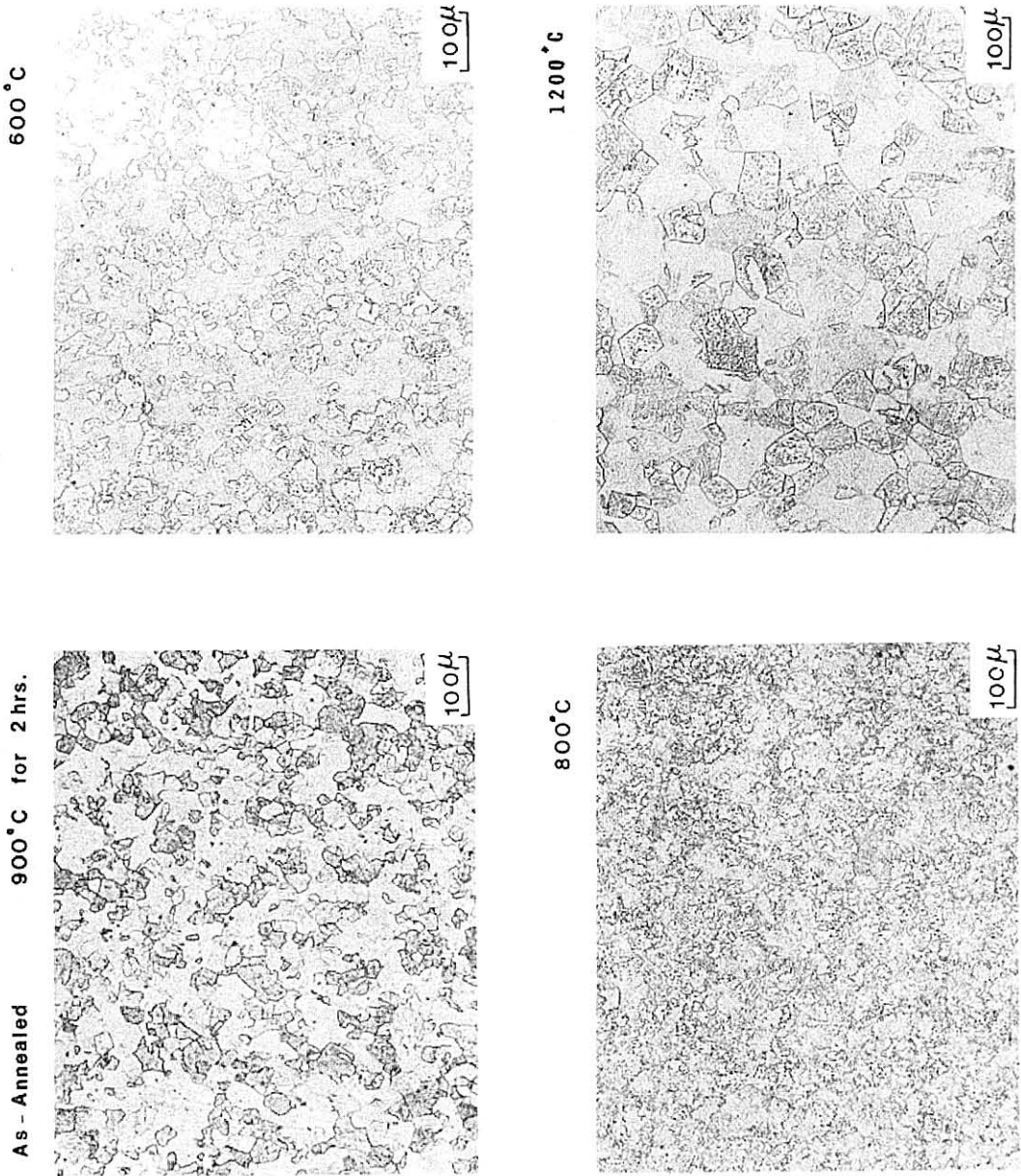


Fig. 14

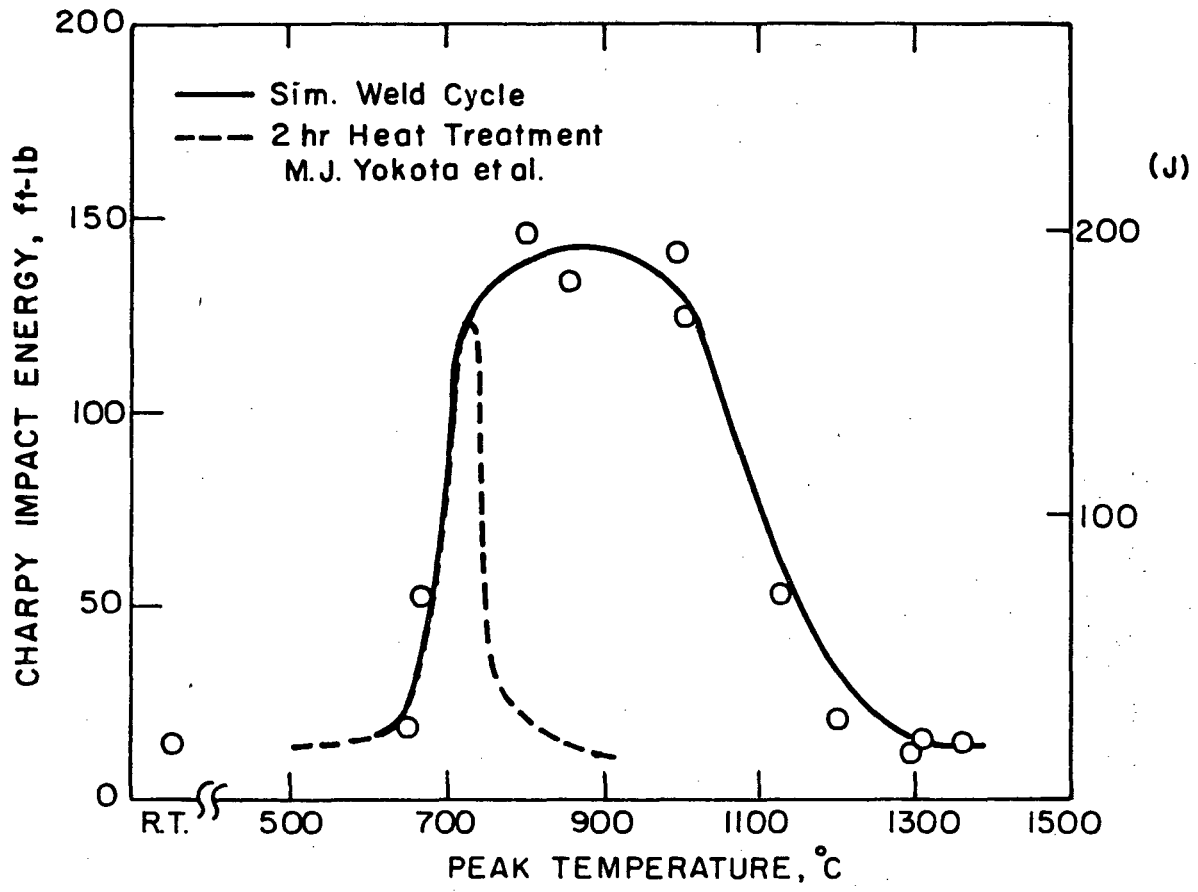
XBB 812-1732

PEAK TEMPERATURE vs. GRAIN SIZE



XBB 799-12638

Fig. 15



XBL 809-5979

Fig. 16

Heat Simulation of HAZ

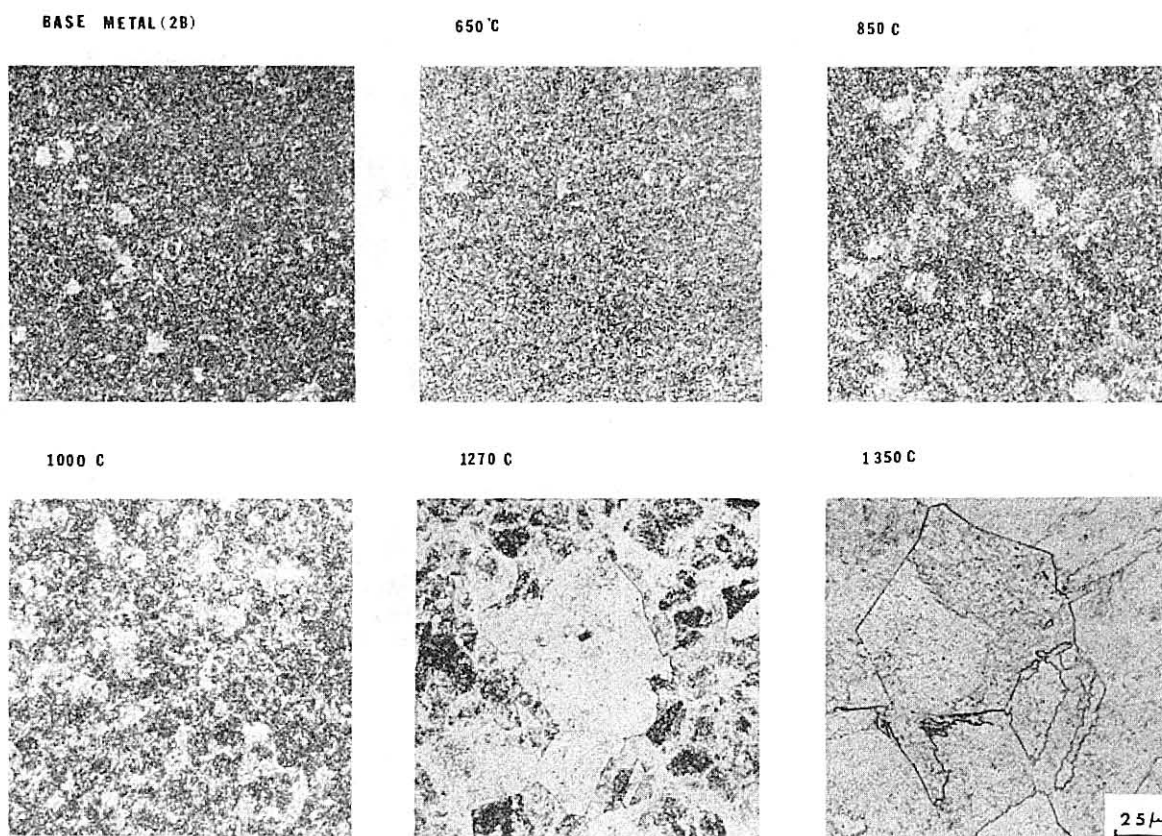
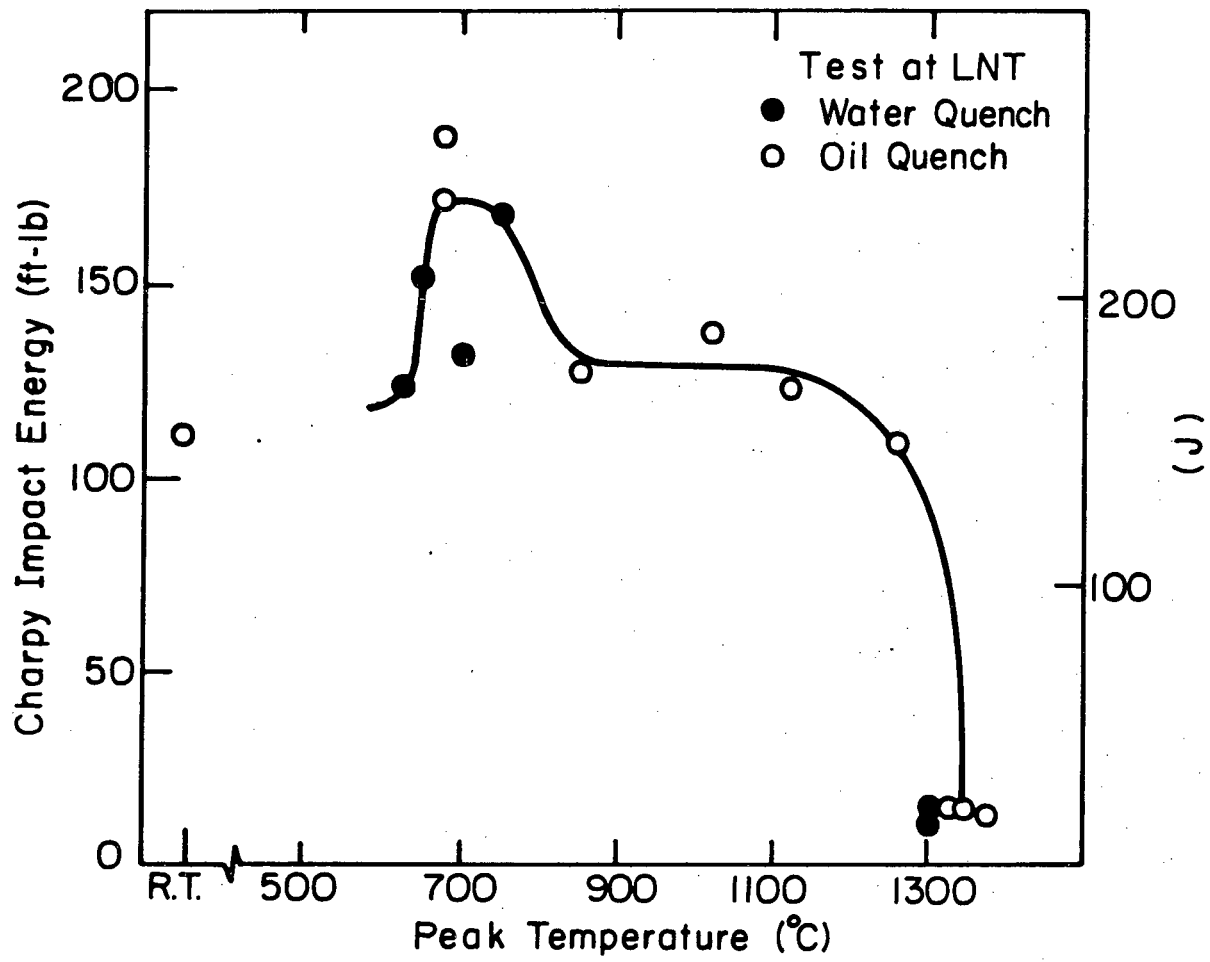


Fig. 17

XBB 805-5474



XBL 805-5189

Fig. 18

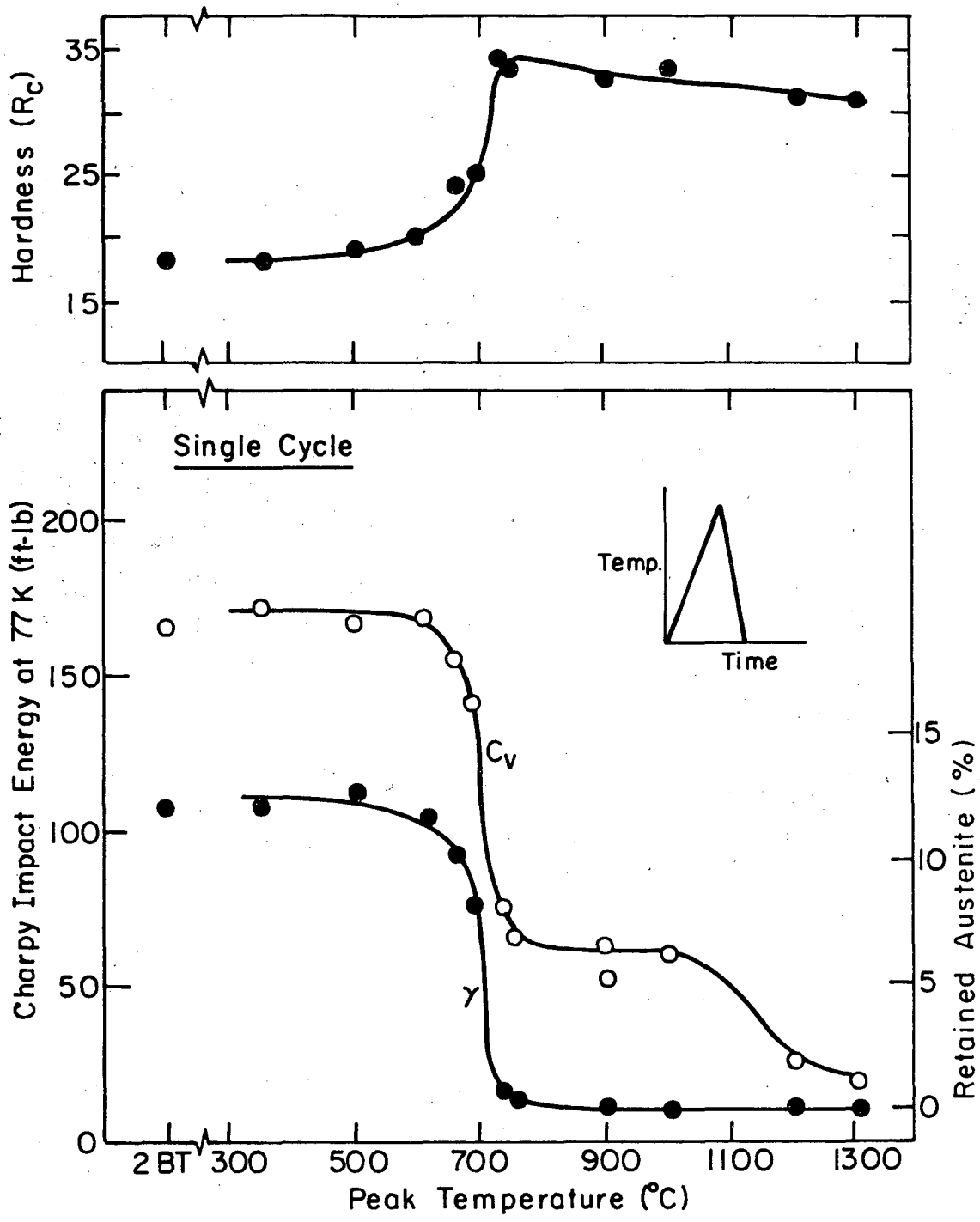
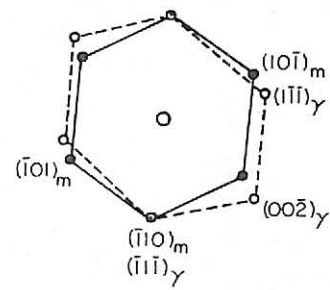
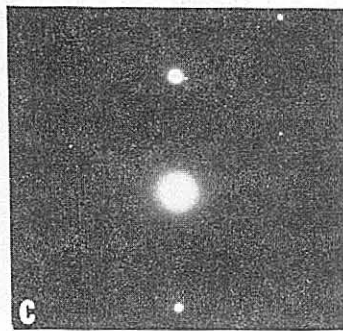
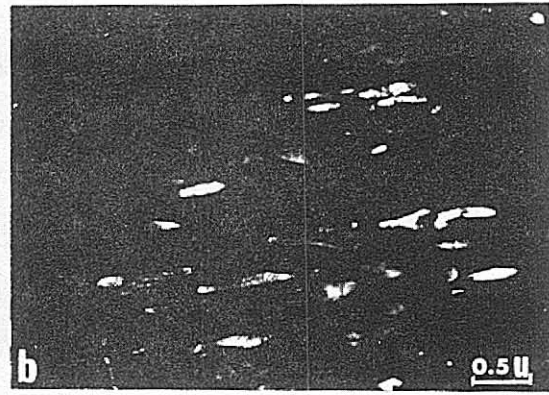


Fig. 19

XBL 822-5170A



- [111] Martensite
- [110] Austenite

Fig. 20

XBB 824-3345

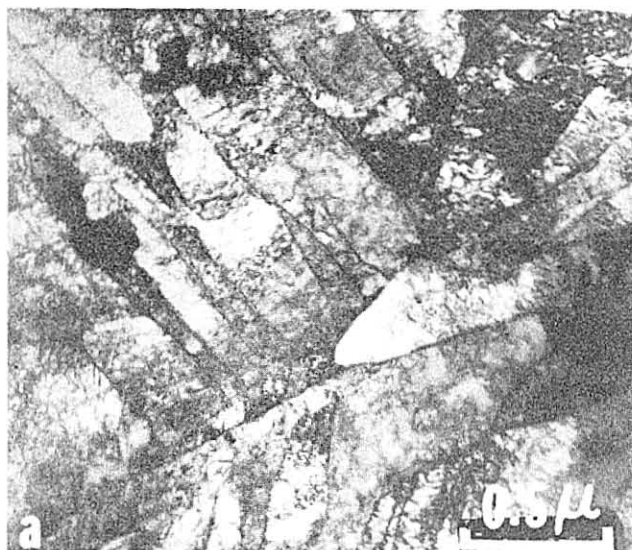
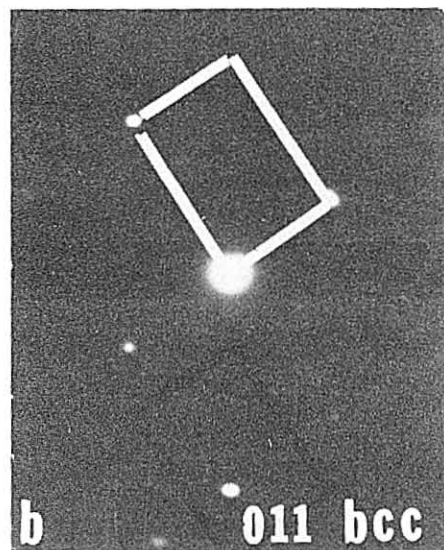


Fig. 21



XBB 824-3343

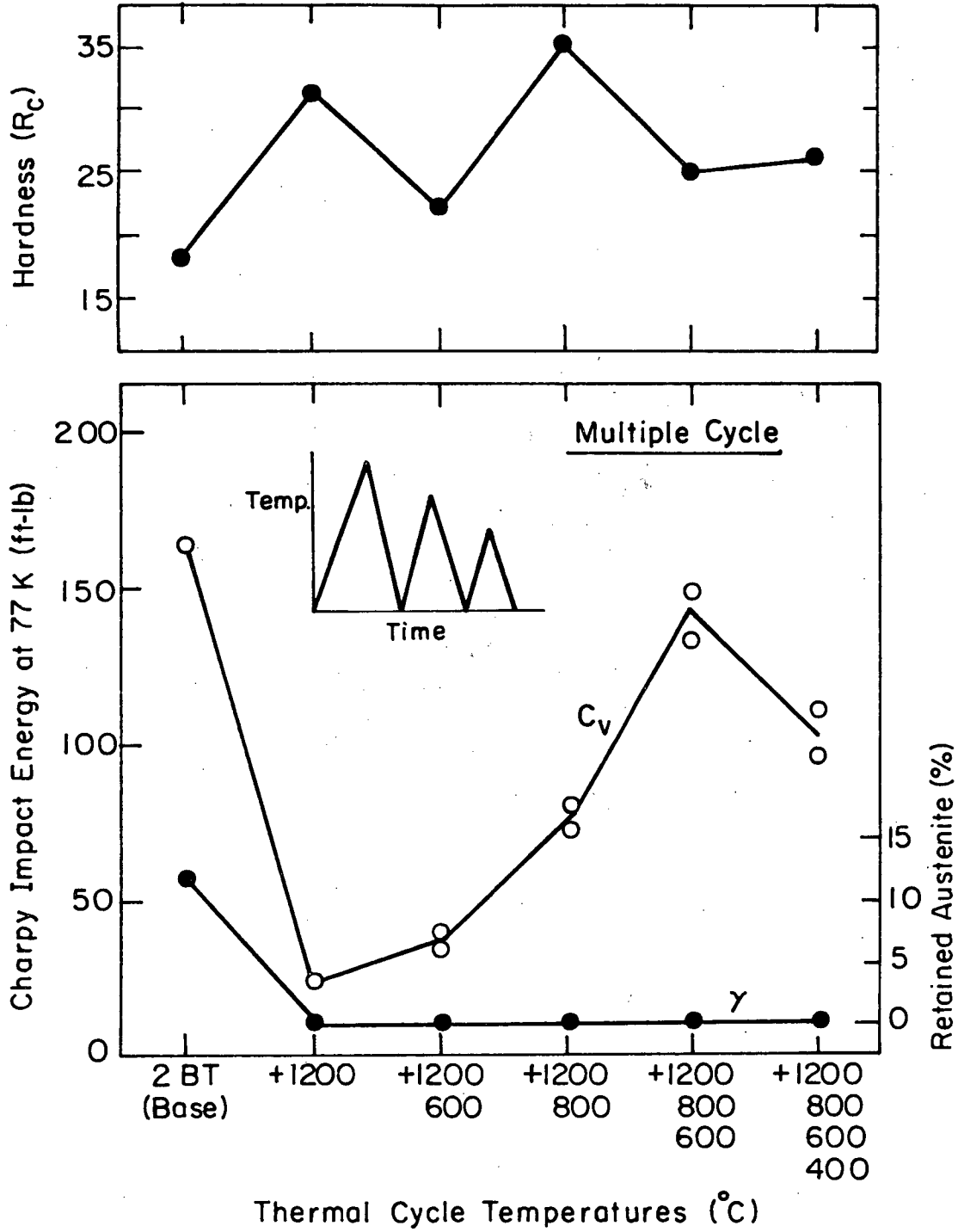


Fig. 22

XBL 822-5169B

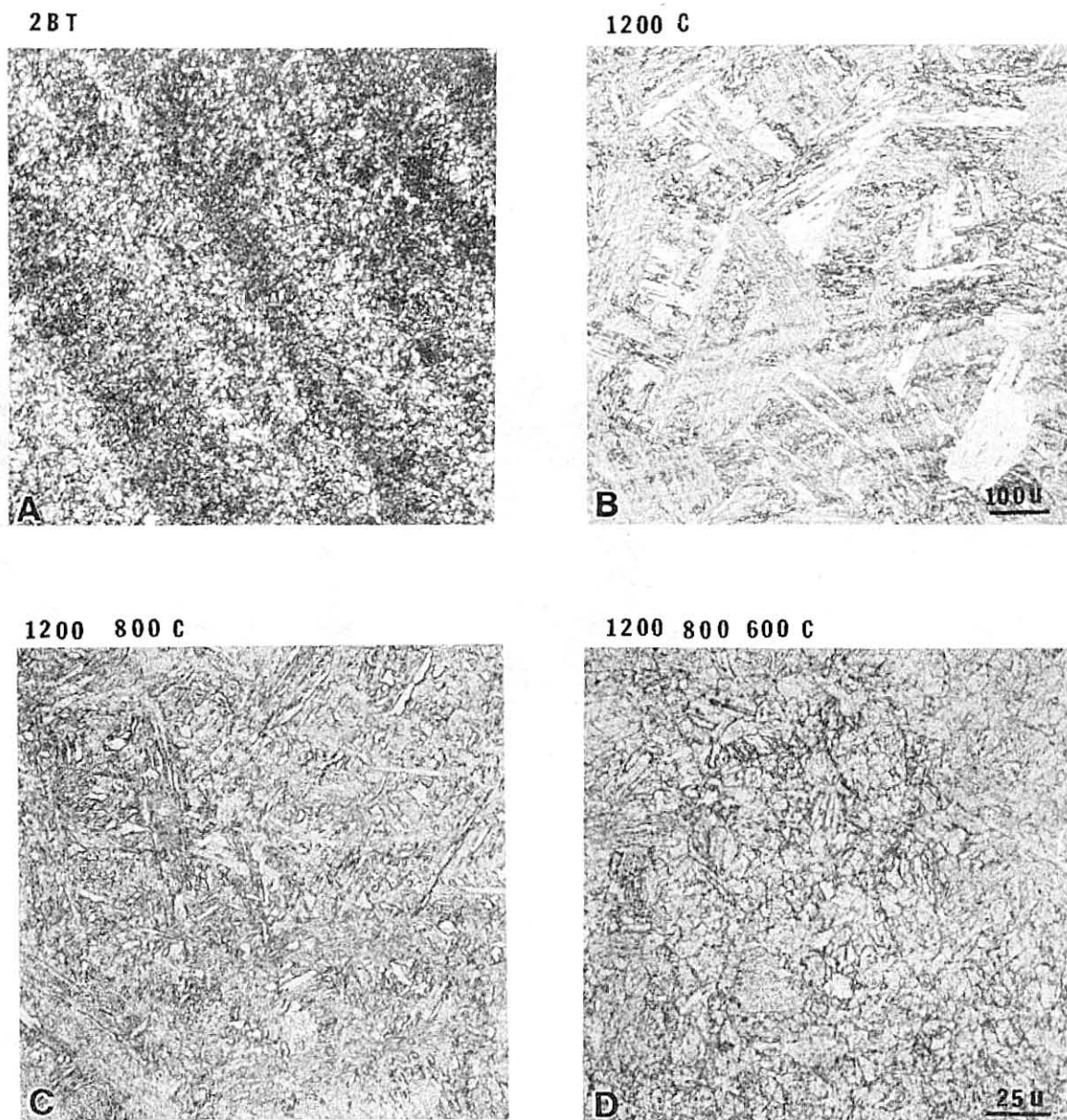
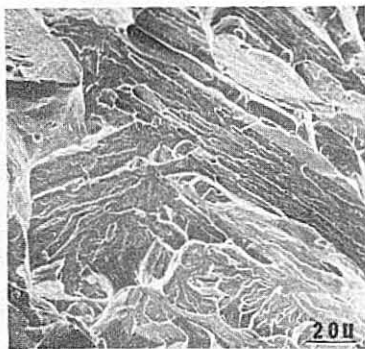
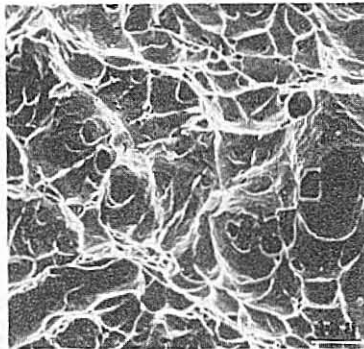


Fig. 23

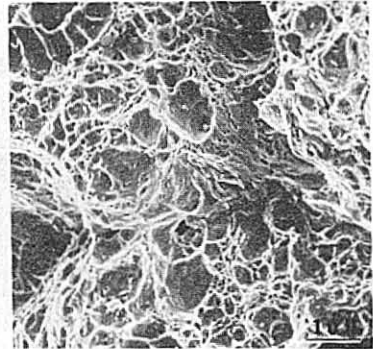
XBB 823-1737



1200 C



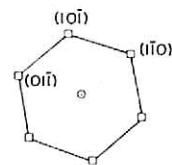
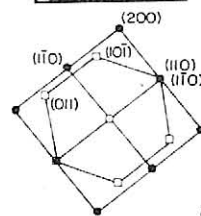
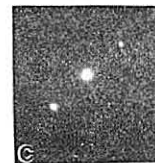
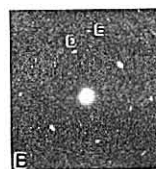
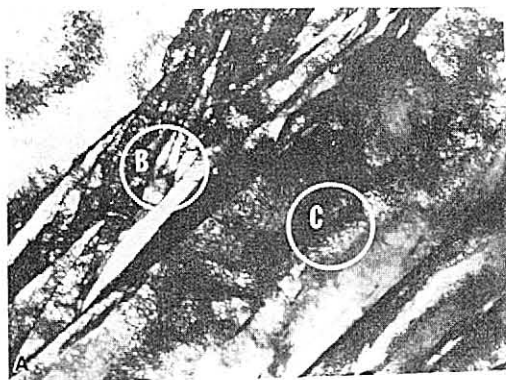
1200
800



1200
800
600

Fig. 24

XBB 822-1250



● [001] bcc
 □ [111] bcc

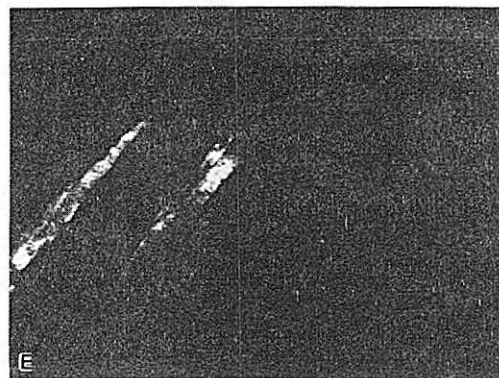
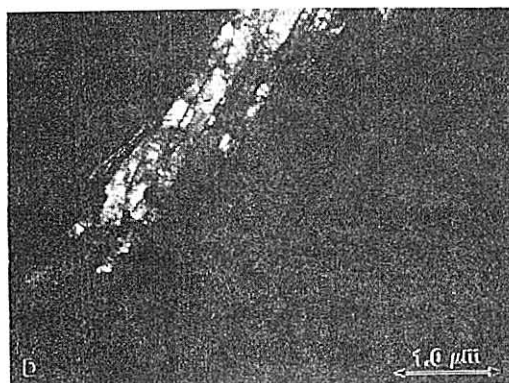


Fig. 25

XBB 822-1251

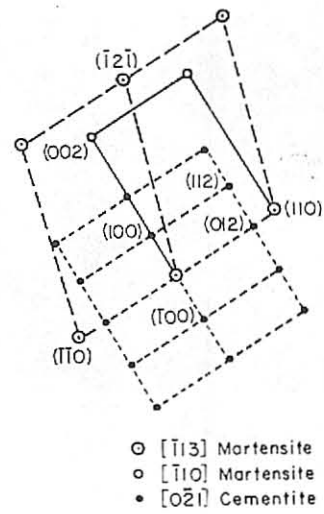
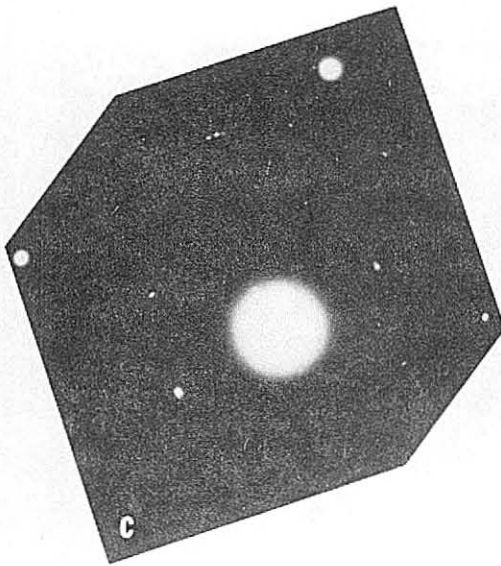
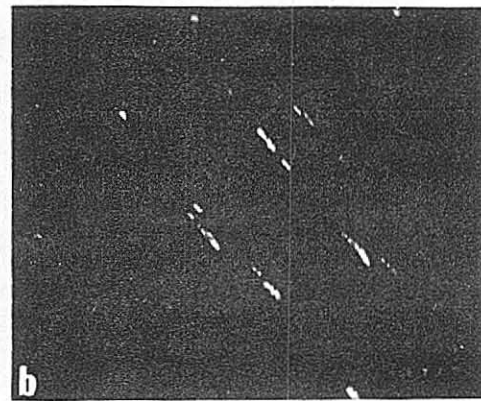
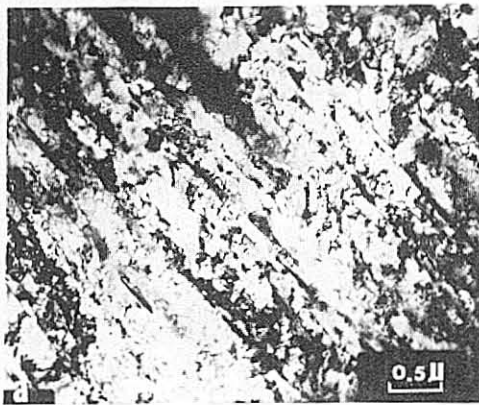


Fig. 26

XBB 824-3344

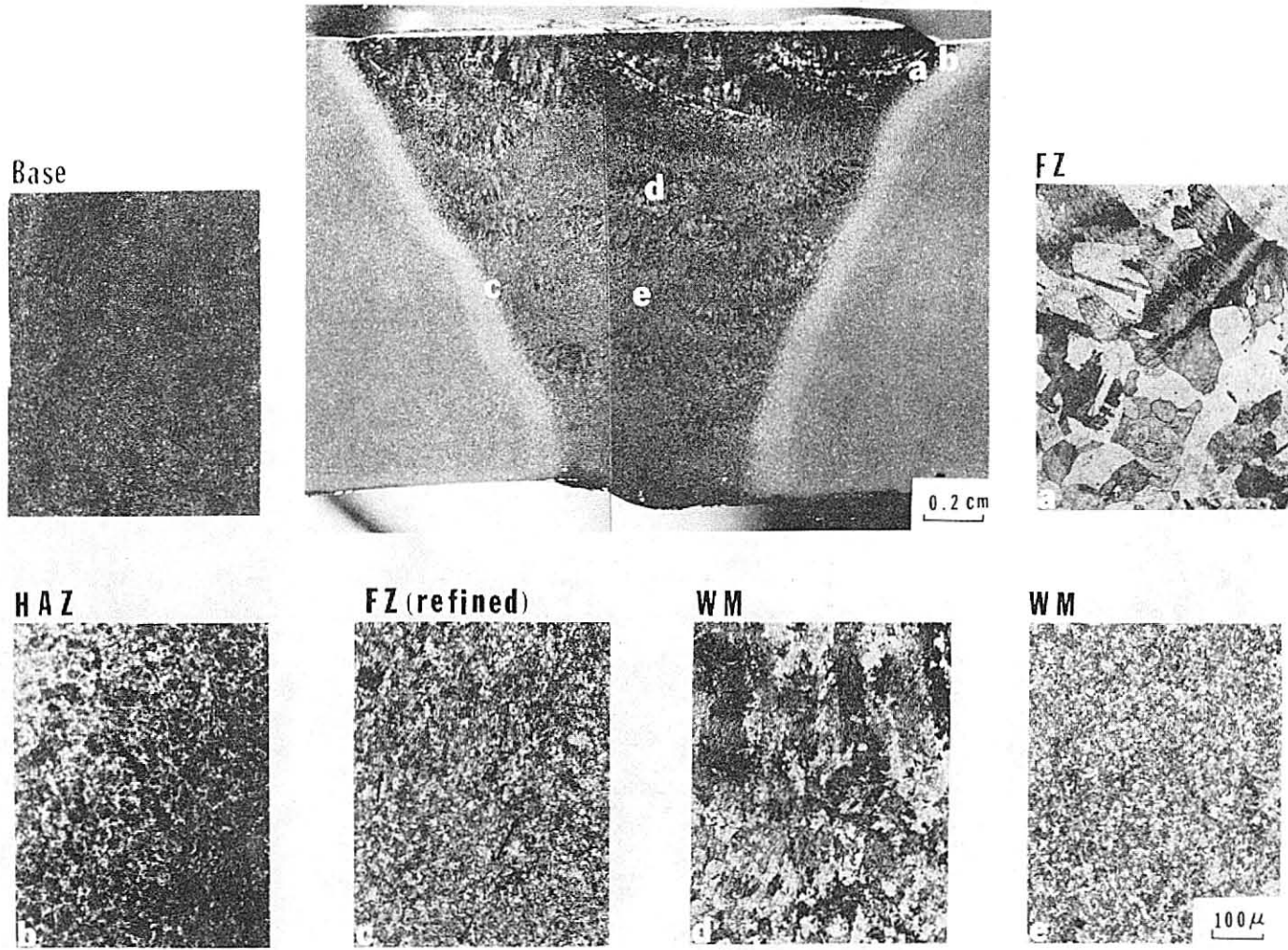


Fig. 27

XBB 805-5473A

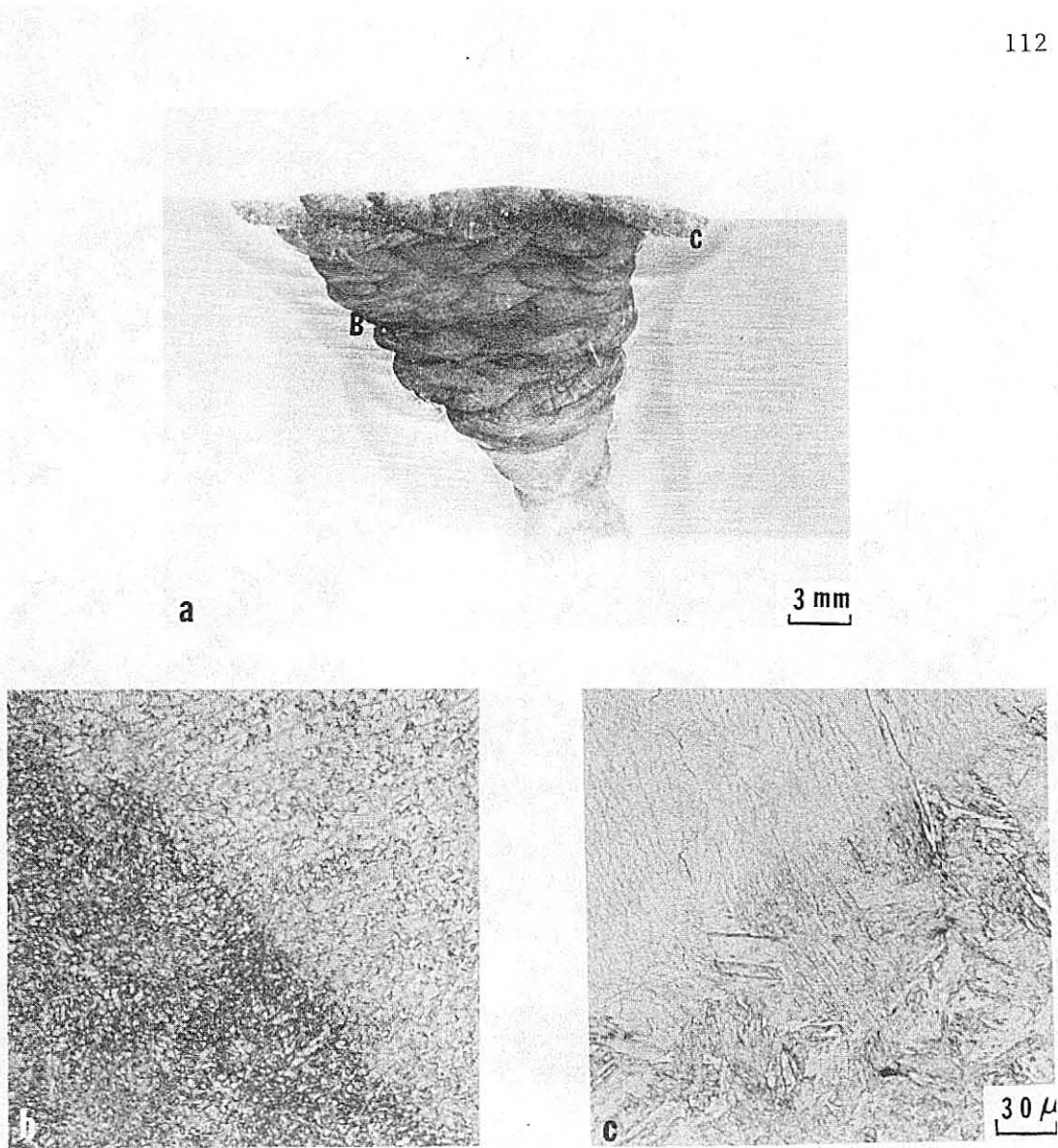
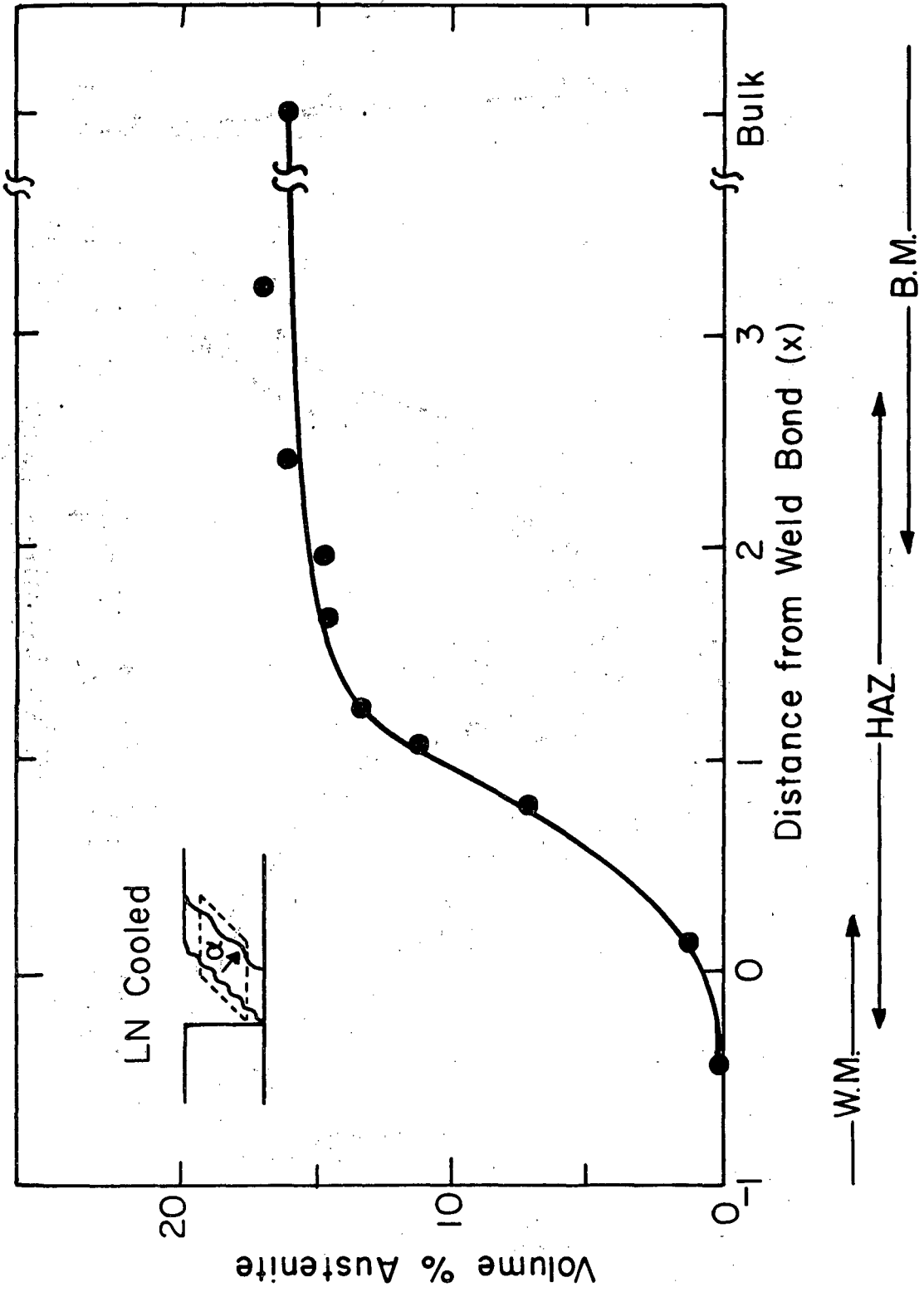


Fig. 28

XBB 818-8063



XBL816-5948

Fig. 29

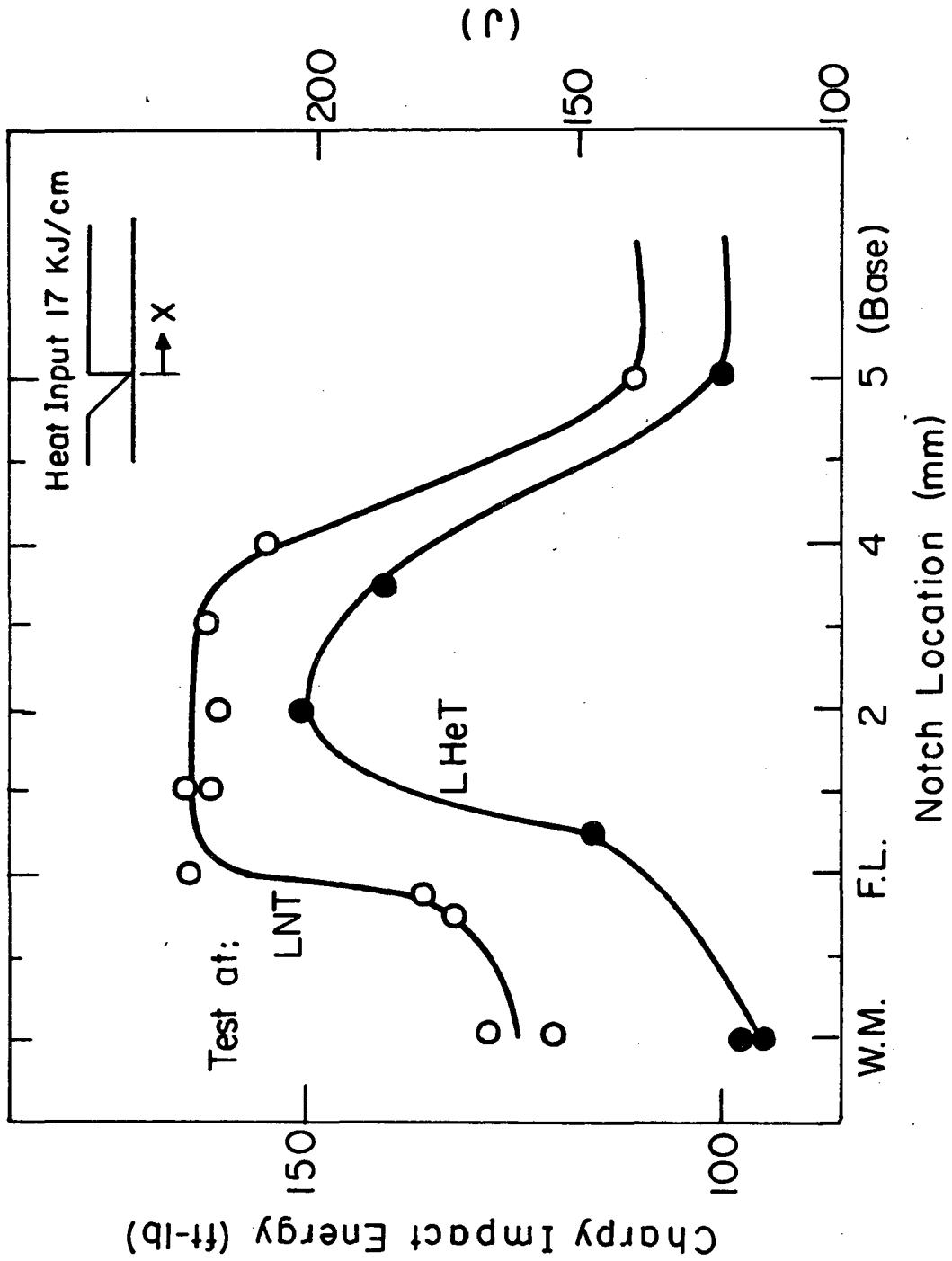
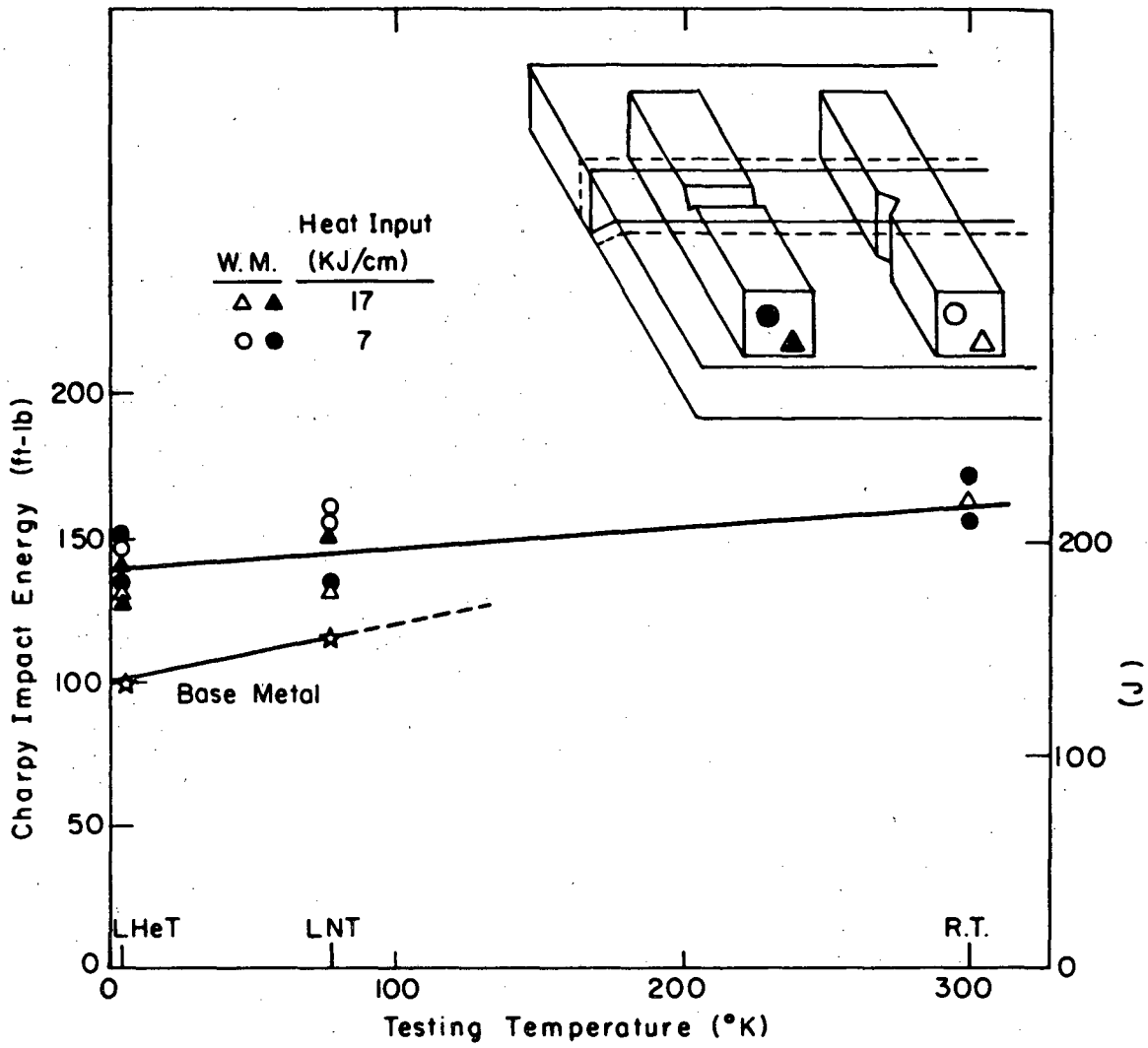


Fig. 30

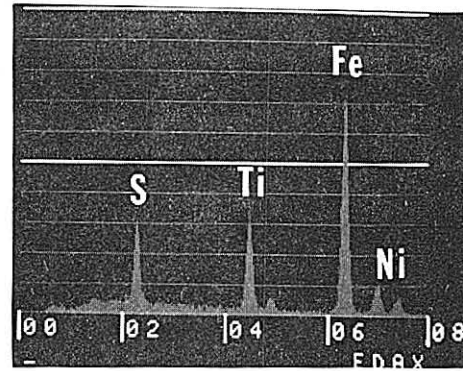
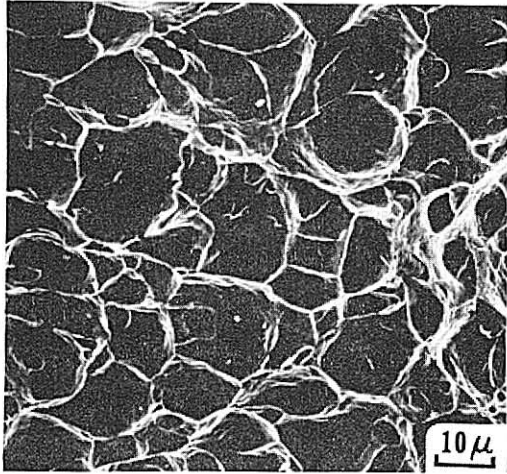
XBL 813-5392



XBL 814-5458

Fig. 31

(a)



(b)

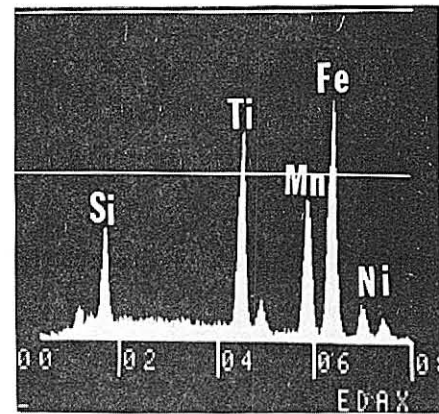
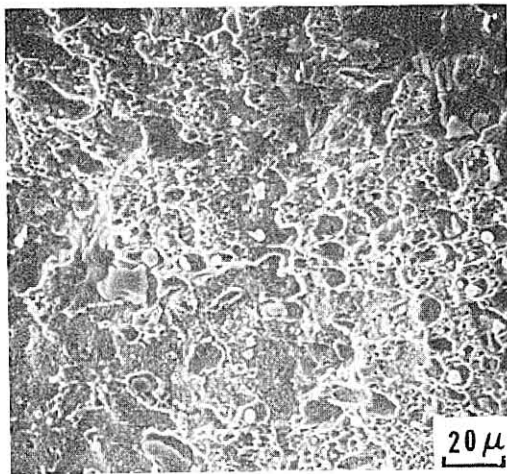


Fig. 32

XBB 817-6675

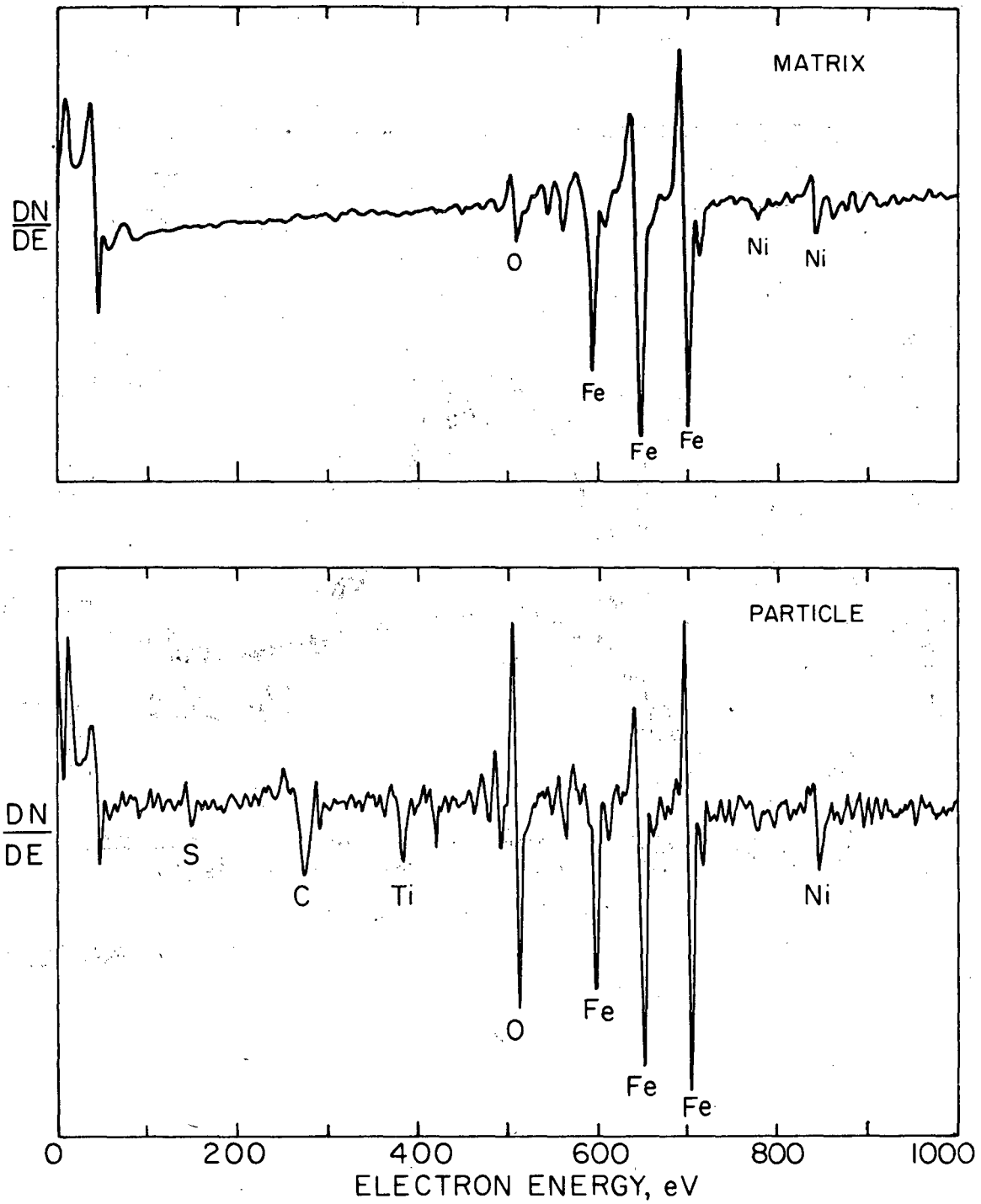
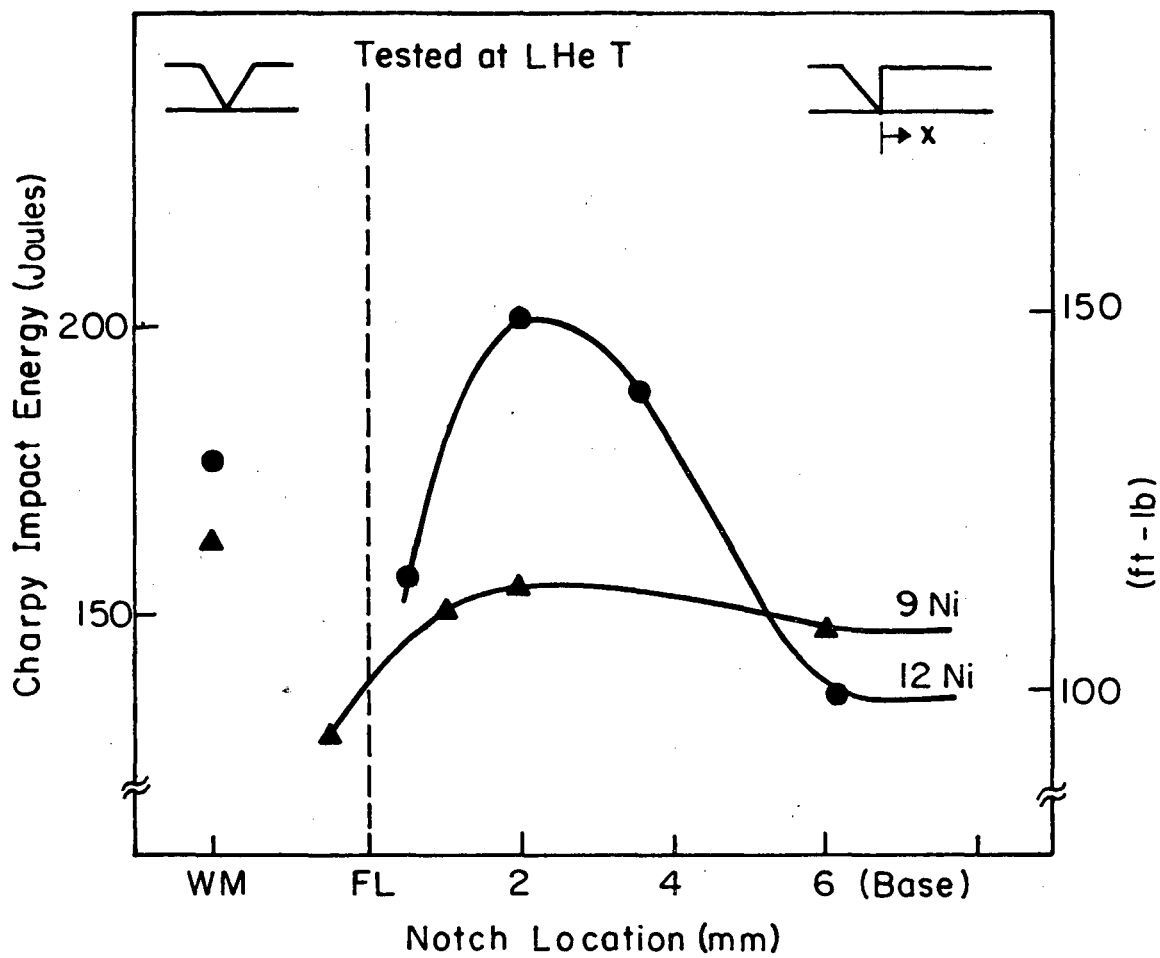


Fig. 33

XBL 805-5176A



XBL 817- 6141A

Fig. 34

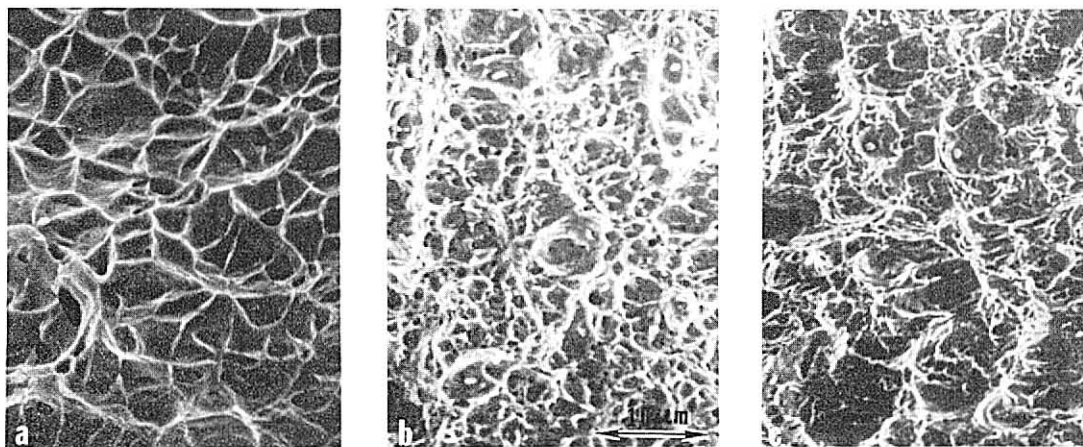
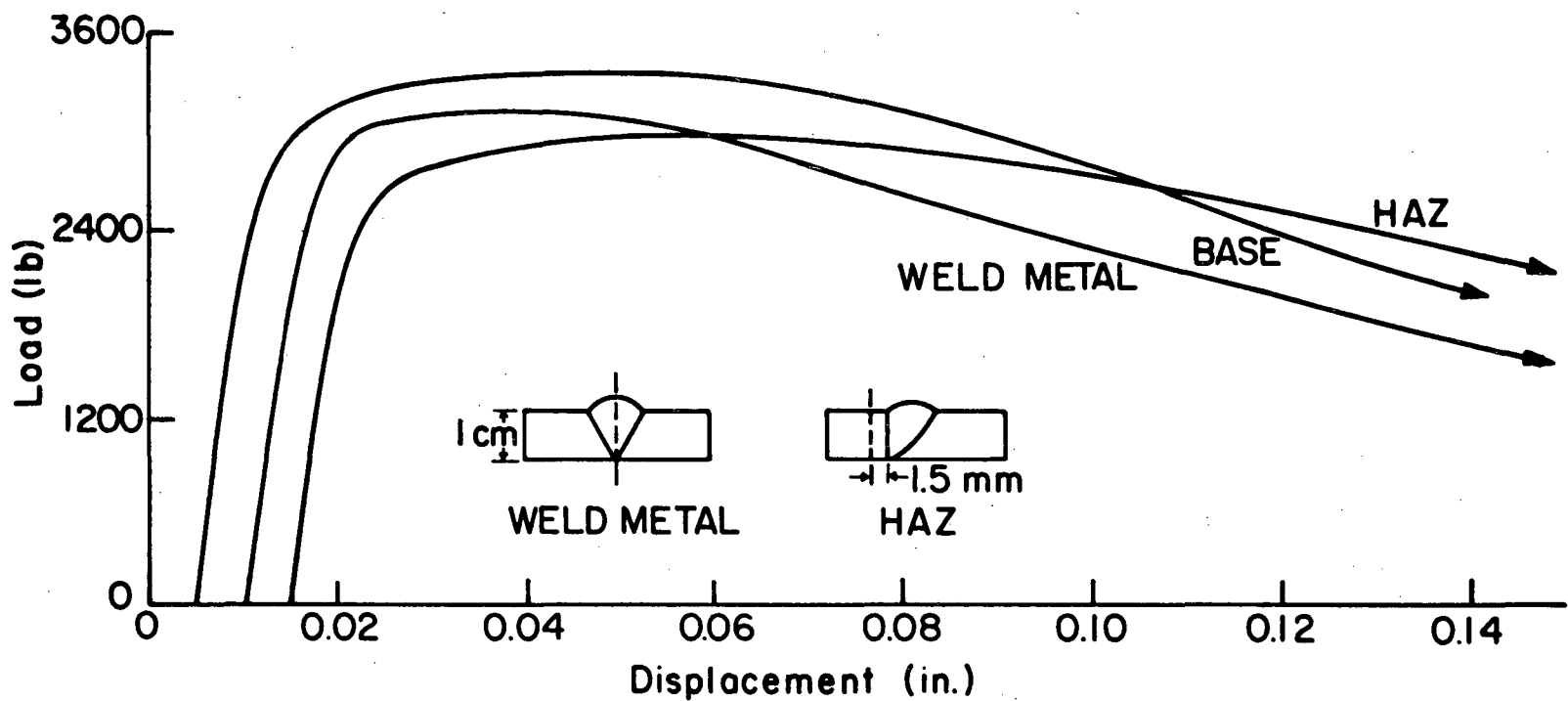


Fig. 35

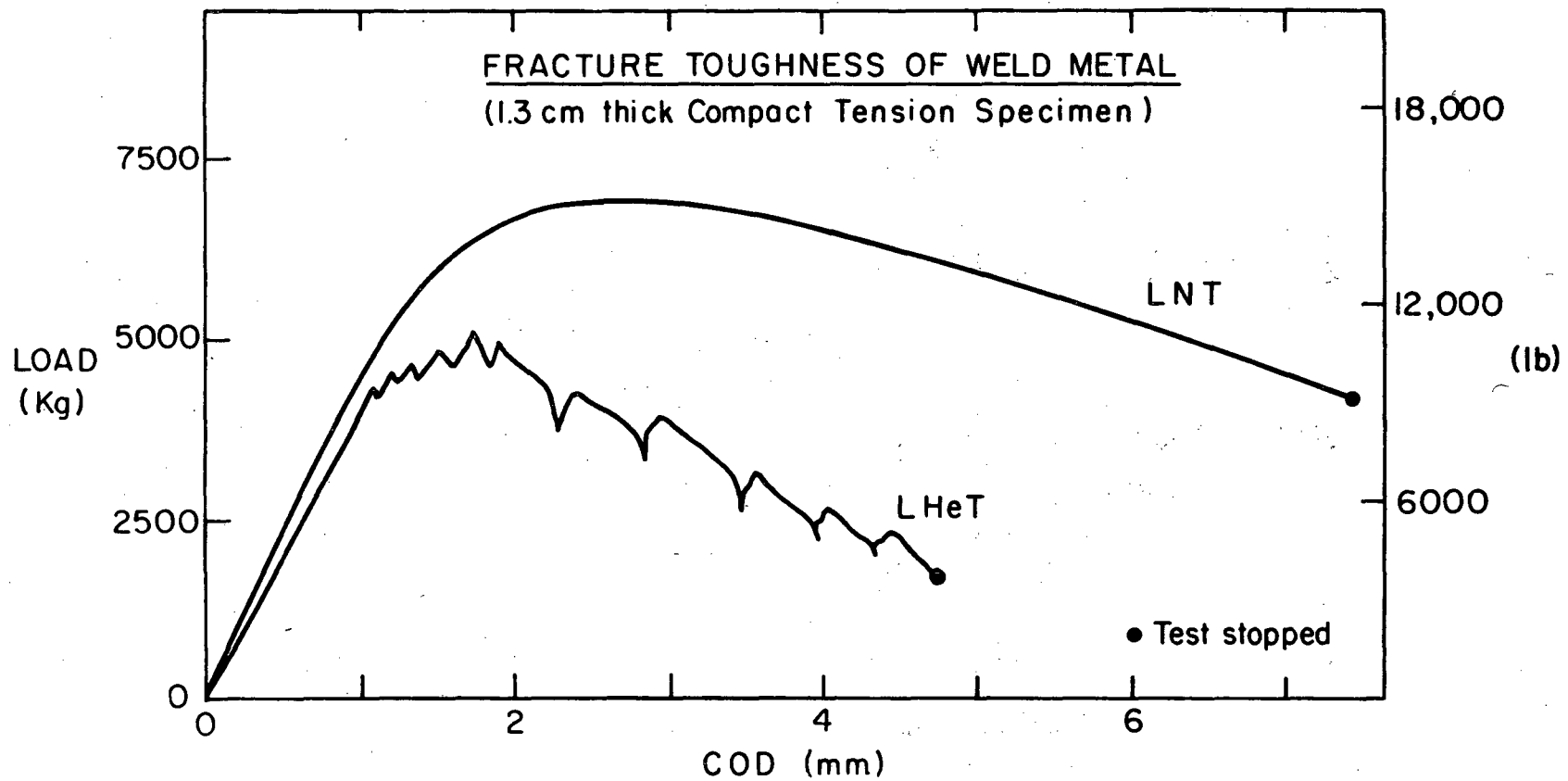
XBB 818-8064

FRACTURE TOUGHNESS TEST AT 77 °K
(1 cm thick 3-point bend test specimen)



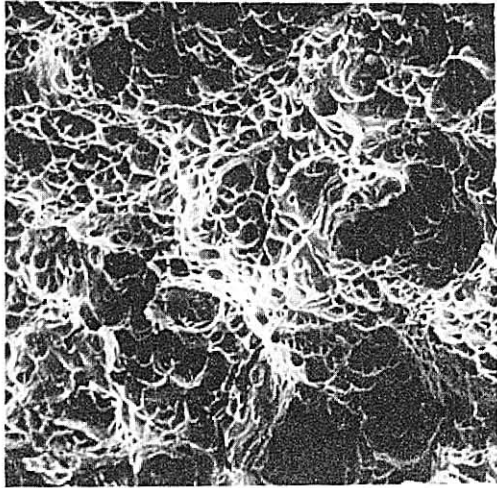
XBL 815-5690

Fig. 36



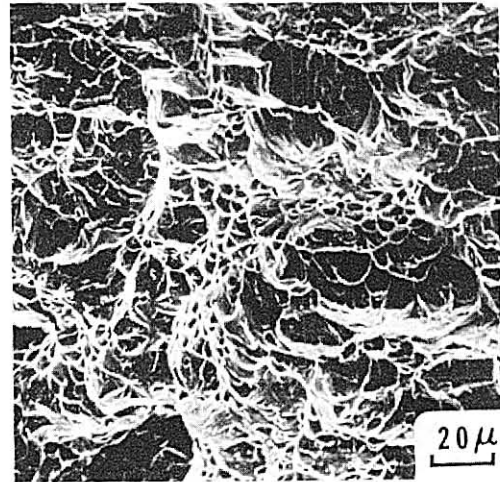
XBL 816-5854 A

Fig. 37



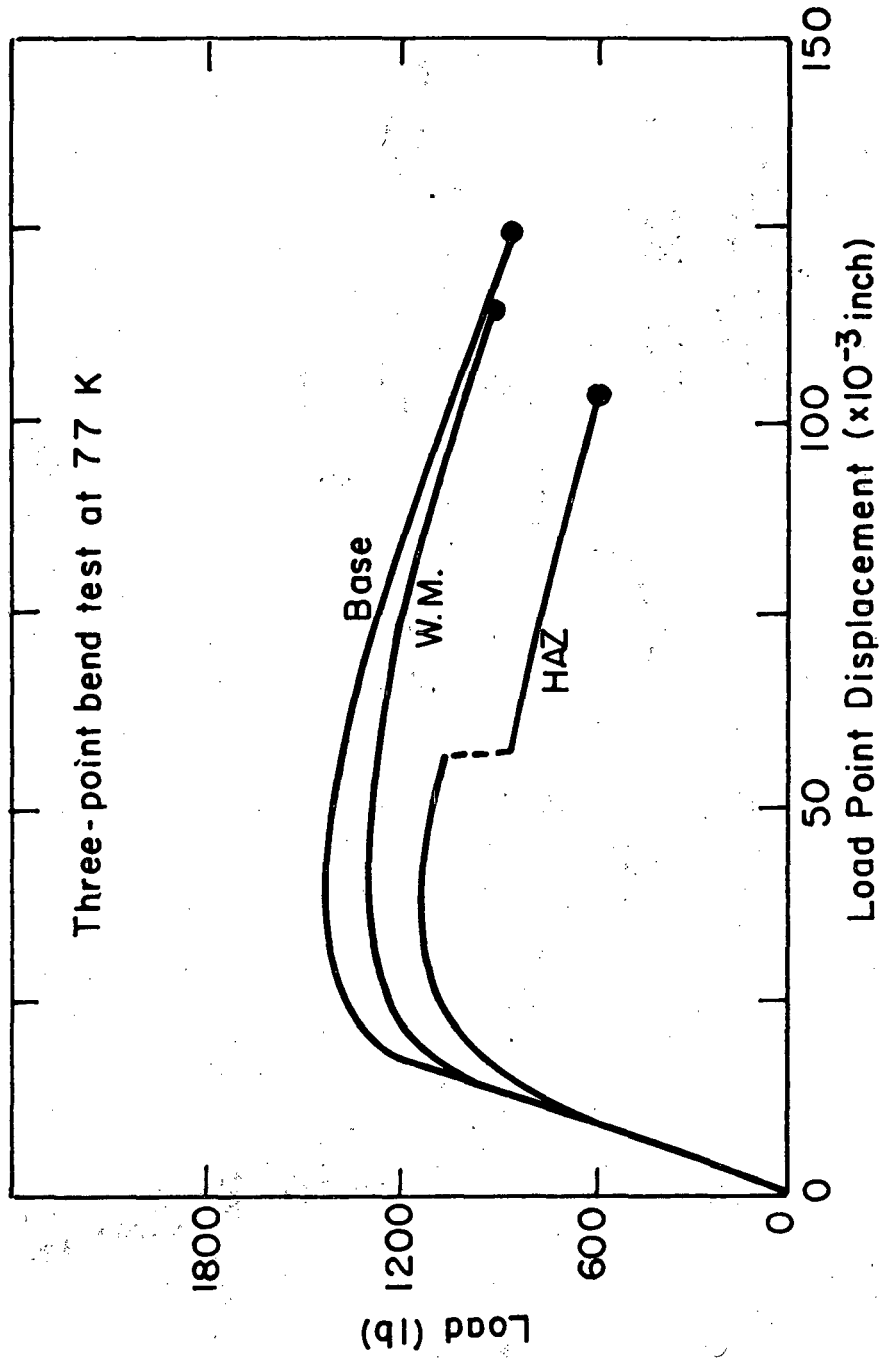
77 K

Fig. 38



6 K

XBB 817-6928



XBL 827-6079

Fig. 39

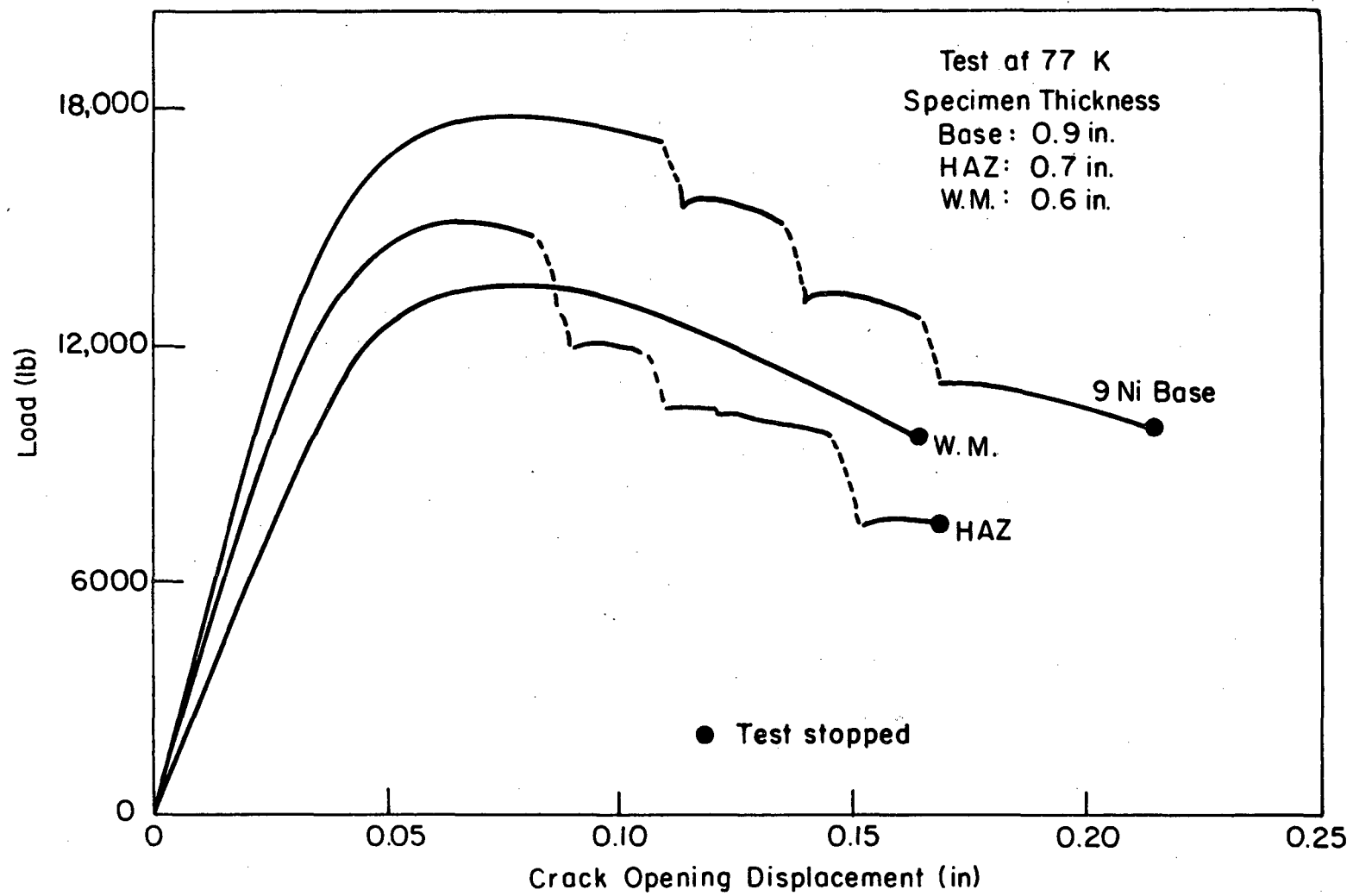


Fig. 40

XBL 827-6032

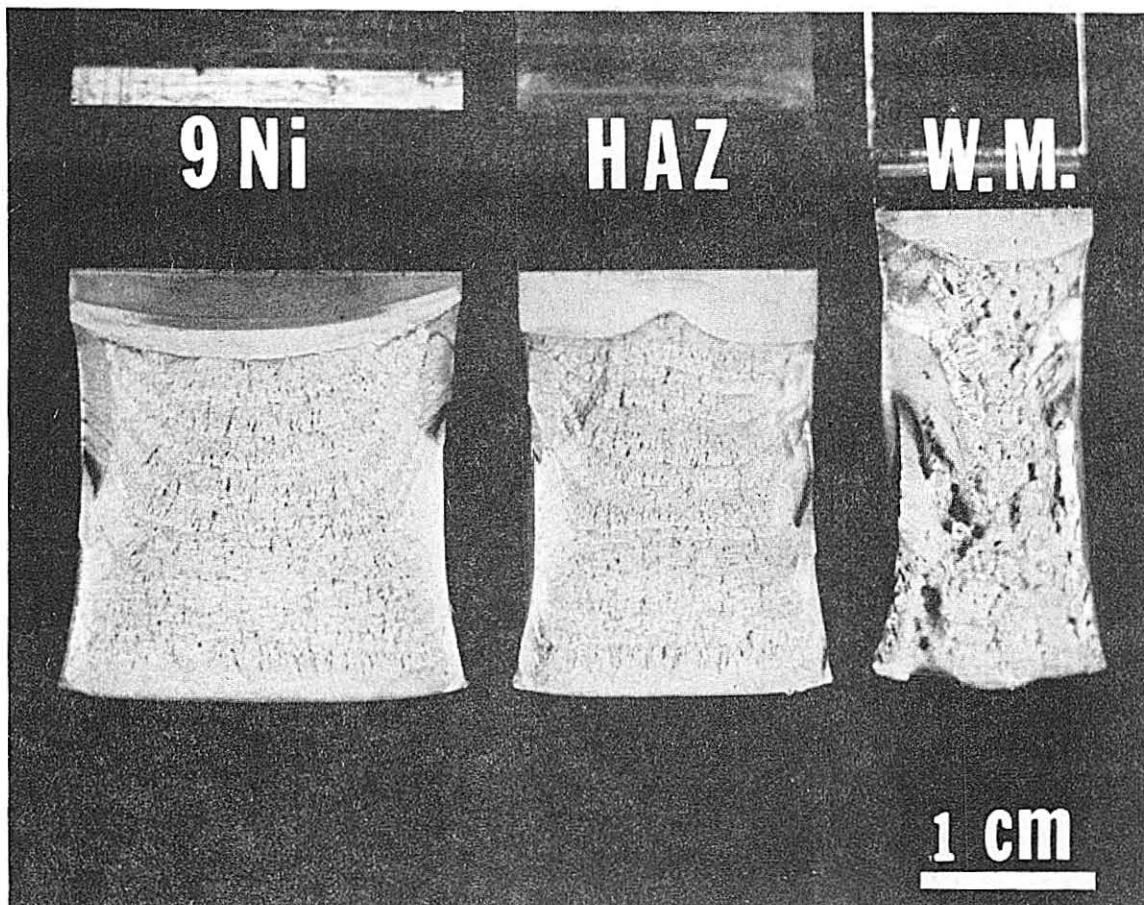
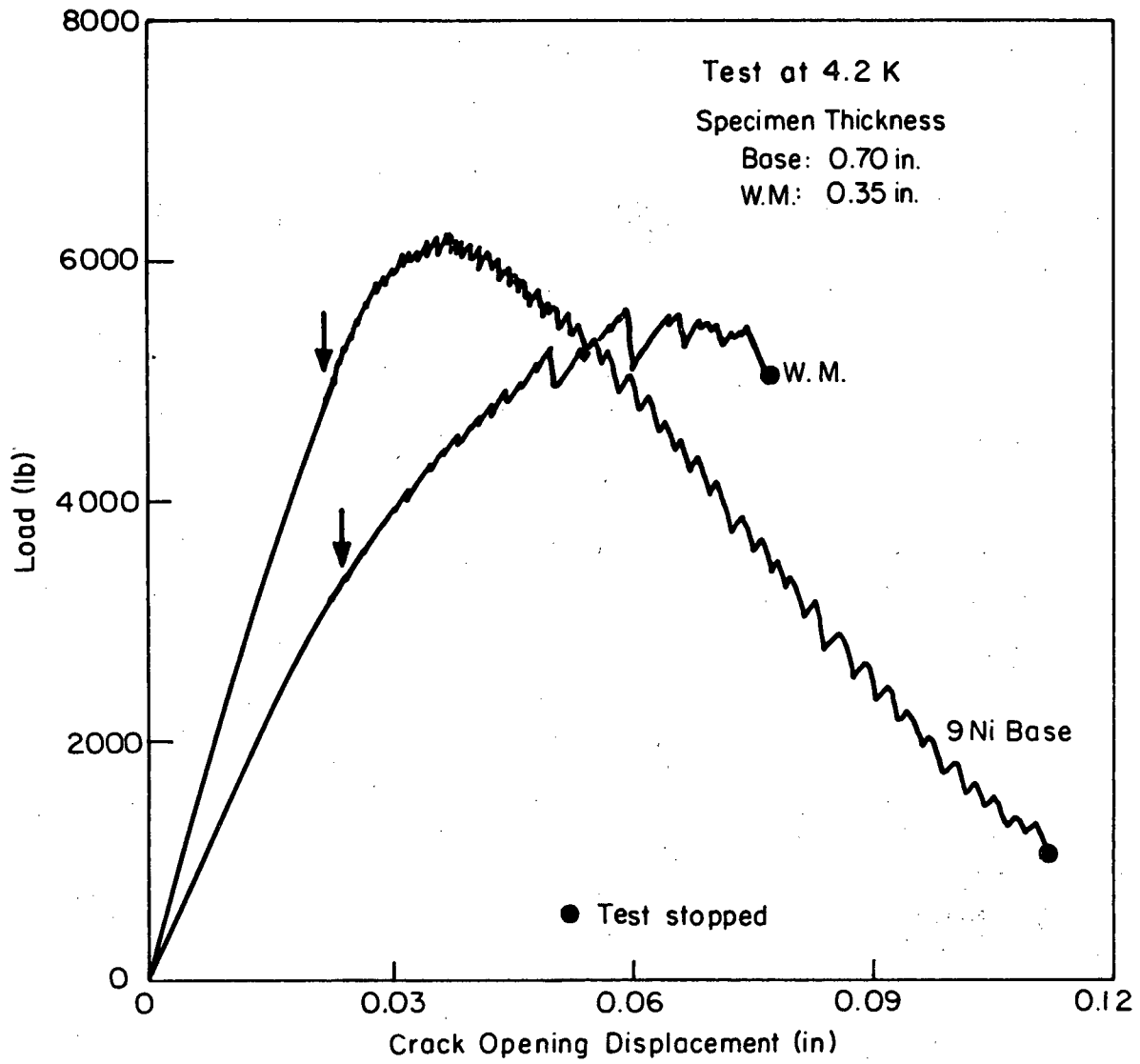


Fig. 41

XBB 827-6399



XBL 827-6031

Fig. 42

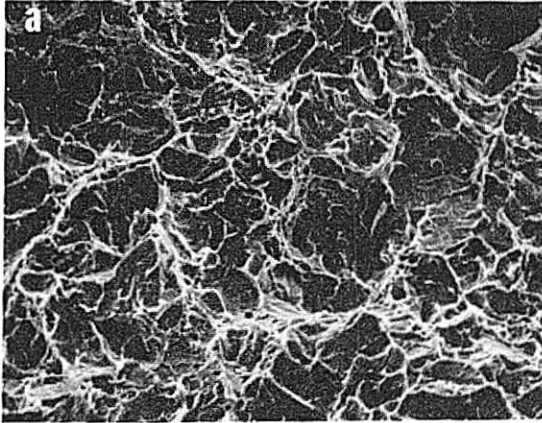
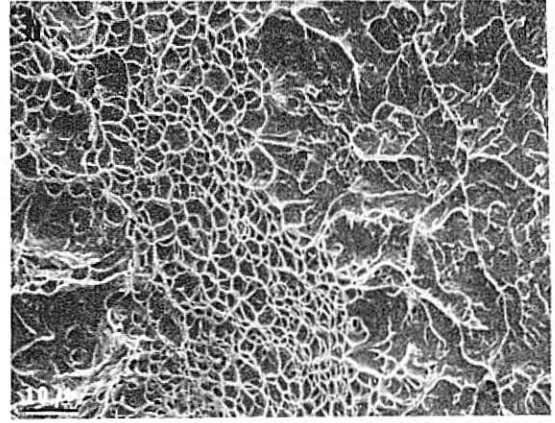


Fig. 43



XBB 827-6400



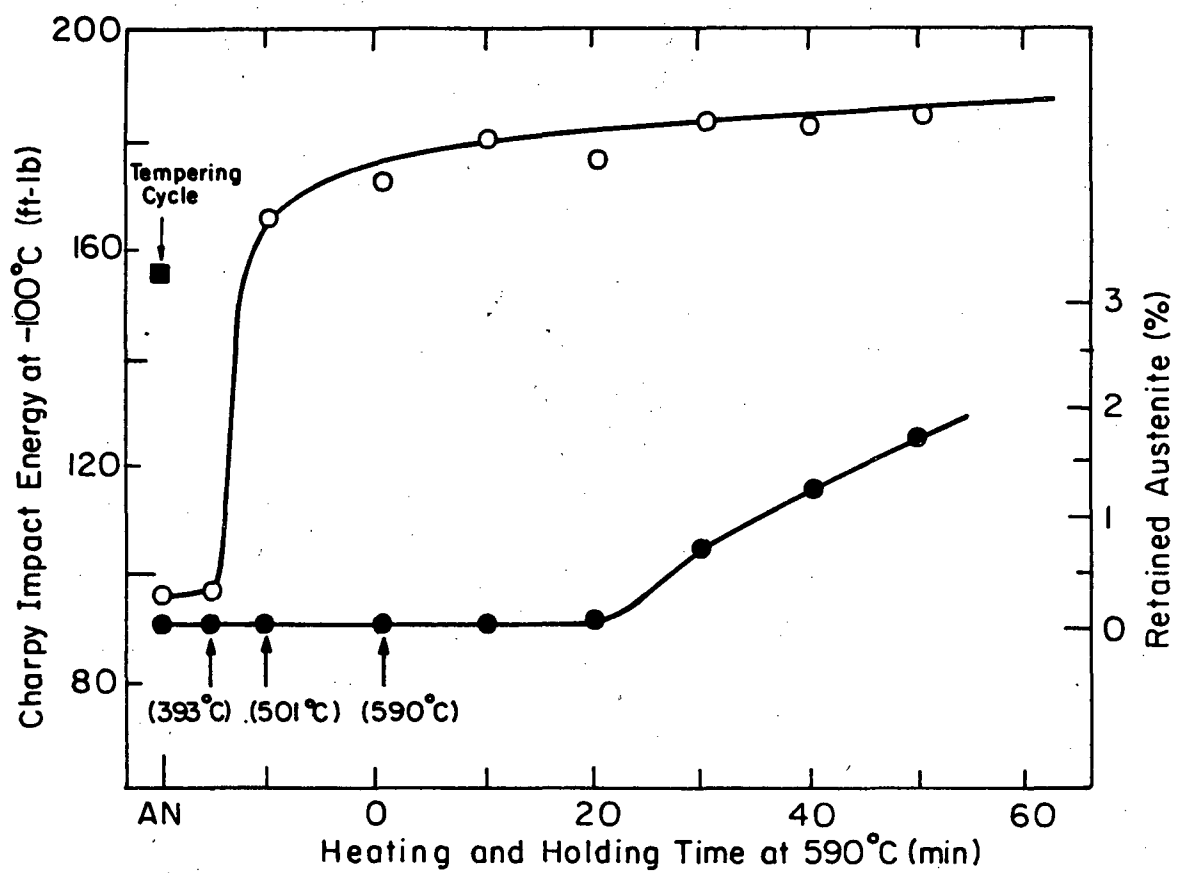
800 °C cycle



750 °C, 1 hr

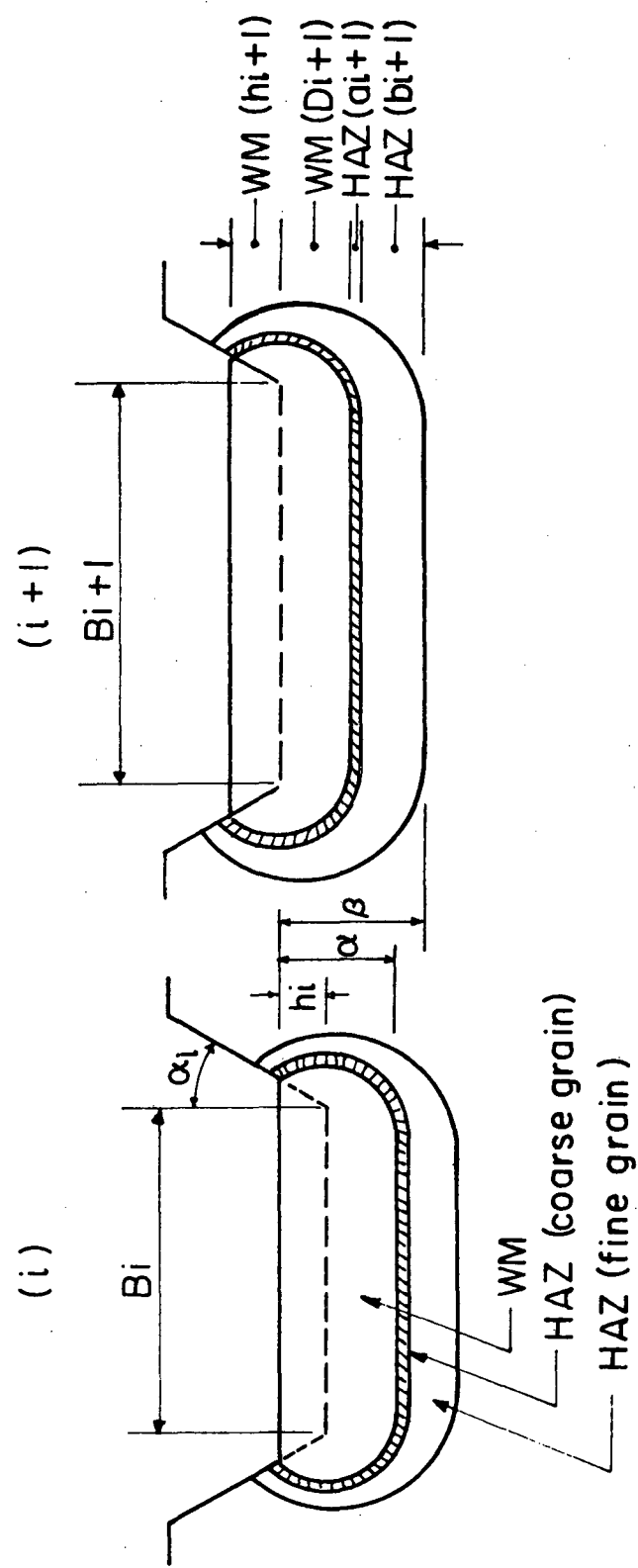
Fig. 44

XBB 823-2183



XBL 8210-6673

Fig. 45



XBL 827-6243

Fig. 46

This report was done with support from the Department of Energy. Any conclusions or opinions expressed in this report represent solely those of the author(s) and not necessarily those of The Regents of the University of California, the Lawrence Berkeley Laboratory or the Department of Energy.

Reference to a company or product name does not imply approval or recommendation of the product by the University of California or the U.S. Department of Energy to the exclusion of others that may be suitable.

TECHNICAL INFORMATION DEPARTMENT
LAWRENCE BERKELEY LABORATORY
UNIVERSITY OF CALIFORNIA
BERKELEY, CALIFORNIA 94720